ETH
Eidgenössische Technische Hochschule Zürich
Swiss Federal Institute of Technology Zurich

Quantum Device Lab
Prof. Dr. Andreas Wallraff
Spring Semester 2014

Master Thesis

Probing Photon Emission in Quantum Dots coupled to a Superconducting Resonator

Author: Kristian Cujia
Student number: 10-911-907
Master program: Micro and Nanosystems
Supervision: Anna Stockklauser
Dr. Julien Basset
Laboratory of Solid State Physics, ETH Zürich

Acknowledgements

I am grateful to Prof. Andreas Wallraff for giving me the opportunity to participate and conduct this project. I am pleased to have met a leader who is so motivated, knowledgeable and friendly and at the same time so challenging. I am thankful for his continuous support and encouragement, as well as for his constructive criticism.

I want to thank the DQD team members. Anna Stockklauser for welcoming me, for her support and guidance during the project and for her explanations. Particularly for trying to motivate me during all the time that the samples did not work. Julien Basset for his really hard work in the clean room, for his motivating discussions and insights into the potential of the experiment as well as for sharing his wide knowledge about the subject. Ville Maisi, Prof. Klaus Ensslin and Prof. Thomas Ihn for their support with the project, as well as for sharing some of their interpretations of the experiments. Without the support of the DQD team members this project would not have given any result.

Special thanks to Yves Salathe for explaining me many things about our digital mambo jambo signal processing setup, as well as his friendly and valuable help with testing a side project on FPGA programming. I also want to thank Farrukh Abdumalikov and Phillip Kurpiers for answering a variety of questions I usually had. The guys in the D5 office: Farrukh, Milan, Anna, Janis, and towards the end of the project Anton for making it a funny place to work. To all the soccer and beachvolley team members for the nice afternoon trainings.

Thanks to all the members of the group who directly or indirectly were involved in the project and for making the qudev the friendly, nice and successful lab it is. I apologize for many people I have not mentioned, particularly all the semester and master students I met. Last but not least, to my family and close friends, as well as to Yvonne Stark for her support and company during all the project.

Kristian Cujia

Abstract

Within the last decade circuit quantum electrodynamics (circuit QED) [1] has proven to be an excellent platform to study the coherent interaction between an artificial atom and a light field. Here an artificial atom, or more precisely an effective two level system, is realized using superconducting circuitry while the cavity is realized as a microwave resonator.

Recently, an effective two level system realized using a semiconductor double quantum dot (DQD) has been coupled to a microwave resonator. In this hybrid system, interactions between the dipole moment of (single) electrons in a DQD and the electromagnetic field in a microwave resonator have been observed ([2], [3]).

Using the same architecture, we initially discuss experiments performed with a resonator sample in order to investigate design parameters influencing its quality factor. With the aim of enabling high bandwidth correlation measurements, we then present the design and implementation of parallel digital filters in a digital signal processing platform.

We finally report on experiments to use the microwave resonator as a tool to explore fundamental processes occurring in a DQD driven out-of-equilibrium. In particular, we perform exploratory attempts to probe the microwave radiation emitted from a voltage-biased DQD by means of first and second order correlation function measurements.

Contents

CHAPTER 1

Introduction

The revolutionary idea of energy quanta introduced by Max Planck about a century ago begun a profound change in our understanding of the fundamental phenomena occurring in nature. It allowed to explain observations which had held inconsistencies with classical physics, such as the blackbody radiation or the photoelectric effect. The theory of quantum electrodynamics (QED) developed by Feynman, Schwinger and Tomonaga is the most successful theory about light, matter, and the interaction of light and matter. One of the most elementary forms in which light and matter interact is that when a single atom interacts with a single photon. Such a process has been a major focus of research for several decades, opening the field now known as cavity QED, where an atom (or ion) is coupled to an optical cavity. In recent years, a solid state realization of an artificial atom and a cavity opened the field now known as circuit QED, in which the artificial atom and the cavity are realized using superconducting circuits in the microwave domain.

Besides fundamental studies, these fields hold potential as eventual platforms for quantum computing applications. To this end, the (artificial) atom is used as a fundamental computing block, i.e. a quantum bit (qubit), and the microwave cavity is used to mediate qubit interactions.

The rapid development experienced in the field of circuit QED has drawn attention into hybrid systems: systems where the artificial atom in the circuit QED setup is realized in different ways. Such hybrid systems hold potential to combine their different advantages, and open the possibility of technology and know-how transfer between different research fields. An example of such systems, and focus of this project, is that of semiconductor (gate defined) quantum dots coupled to superconducting resonators. In this work we intended to use the circuit QED setup as a tool to explore fundamental phenomena occurring in a DQD. When the DQD is driven out of equilibrium, i.e. when it is voltage-biased, excess energy is released by emission of phonons and/or photons. The main idea is to use the microwave resonator as a selective probe to collect and analyse the emitted microwave radiation, which is not accessible in traditional semiconductor quantum dot architectures.

One of the most established tools to characterize electric fields is the measurement of correlation functions. Correlation functions evaluate the degree of temporal coherence of light, i.e. the ability of light to interfere with itself. In turn, temporal coherence properties can be used to infer details about physical properties of the light source. We focused on measuring the first and second order correlation functions of the radiation originating from the DQD. To this end, we incorporated a quantum limited parametric amplifier [4] to our measurement setup and used Field Programmable Gate Array (FPGA) electronics.

CHAPTER 2

Review

In this chapter we will review the basic concepts of cavity quantum electrodynamics (cavity QED) and discuss how it can be implemented using superconducting microwave electronics and semiconductor heterostructures.

2.1. Cavity QED

Let us consider a cavity formed by two highly reflective mirrors which define a quantized mode of the electric field (see Fig. 2.1). Due to the high reflectivity of the mirrors, photons stay inside the cavity for a long time. Inside the cavity there is an atom which can interact with the photons present in the cavity. After an average time $1/\kappa$ characterized by the cavity decay rate κ, photons leave the cavity through the mirrors and can be detected on either end. The cavity can be characterized by its resonance frequency $\omega_r/2\pi$ and its decay rate κ, or equivalently its quality factor $Q = \omega_r/\kappa$. The atom inside the cavity interacts with the electromagnetic field via dipole interaction, coupling its electronic excitations to the electric field. To model the system, the atom inside the cavity is often considered as a two level system with a ground $|g\rangle$ and an excited state $|e\rangle$ whose energy difference is given by $\hbar\omega_a$. In general, any system with an anharmonic energy spectrum, i.e. one where the energy levels are not equally spaced, can be considered as a two level system. The reason is that experimentally an individual transition can be isolated.

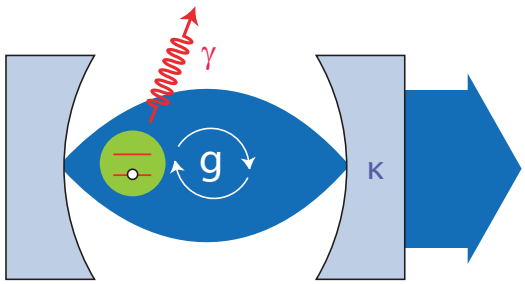

Figure 2.1.: Schematic of the cavity QED setup. Two mirrors define a quantized electric field mode which leaves the cavity at a rate κ. A two level system inside the cavity couples via dipole interaction with the field and exchanges excitations at a rate g. Interactions between the two level system and other degrees of freedom occur at a rate γ.

When the cavity and the atom are in resonance, they can exchange energy quanta at a rate g which is called the coupling constant. However, the atom can also couple to other uncontrolled degrees of freedom, which results in an energy loss at a rate γ. This system is described by a Hamiltonian known as the *Jaynes-Cummings* Hamiltonian [5].

$$H_{JC} = \hbar\omega_r \left(a^\dagger a + \frac{1}{2}\right) + \frac{\hbar\omega_a}{2}\sigma_z + \hbar g \left(\sigma^+ a + \sigma^- a^\dagger\right) \tag{2.1}$$

where the Hilbert space is spanned by a basis which keeps the total number of excitations constant: $\{|g,n\rangle, |e,n-1\rangle\}$. The first term in equation 2.1 describes the energy of a harmonic oscillator (in this case the electric field) in terms of a ($a^\dagger$) i.e. annihilation (creation) operators. The second term describes the energy of a two level system, where σ_z is the Pauli z-operator given by $\sigma_z = |g\rangle\langle g| - |e\rangle\langle e|$. The third term describes the interaction between the cavity and the atom at a rate g, where $\sigma^- = |g\rangle\langle e|$ and $\sigma^+ = |e\rangle\langle g|$ are the lowering and raising operators. The terms $\sigma^+ a$ ($\sigma^- a^\dagger$) describe the process of photon absorption (emission). This interaction neglects terms where the total number of excitations in the system is not constant, a simplification known as the rotating wave approximation.

When the interaction rate g is larger than the rates κ and γ, the system is said to be in the *strong coupling* regime. In this regime, the dynamics of the system strongly depend on the detuning $\Delta = \omega_r - \omega_a$ between the atom and the cavity. Two cases are of particular interest, namely small and large detuning.

Dispersive Limit When the detuning is large such that $|\Delta| \gg g$ no energy exchange between the atom and the cavity takes place, however a dispersive interaction remains. Since g/Δ is small, the Jaynes-Cummings Hamiltonian in equation 2.1 can be expanded using a Taylor series in g/Δ [6].

$$H_{disp} = \hbar\left(\omega_r + \frac{g^2}{\Delta}\sigma_z\right)\left(a^\dagger a + \frac{1}{2}\right) + \frac{\hbar\omega_a}{2}\sigma_z \tag{2.2}$$

The first term in equation 2.2 again describes the electric field in the cavity as a harmonic oscillator. However, its resonance frequency now depends on the state of the atom $\omega_r^{'} = \omega_r \pm g^2/\Delta$. This dispersive frequency shift of g^2/Δ can be used to infer the atom state by measuring the cavity frequency [7]. Equation 2.2 can be rewritten as:

$$H_{disp} = \hbar\omega_r\left(a^\dagger a + \frac{1}{2}\right) + \frac{\hbar}{2}\left(\omega_a + \frac{2g^2}{\Delta}a^\dagger a + \frac{g^2}{\Delta}\right) \tag{2.3}$$

Equation 2.3 shows that the transition frequency of the atom is modified by the photon number in the cavity $a^\dagger a$, an effect known as the *ac-Stark shift*. The term g^2/Δ in the effective transition frequency is known as the *Lamb shift*.

Vacuum Rabi Splitting All terms in the Jaynes Cummings Hamiltonian (equation 2.1) are conservative, i.e. keep the total number of excitations constant. This symmetry can be observed in the basis $\{|g,n\rangle, |e,n-1\rangle\}$ when we calculate the matrix elements

$$\begin{aligned} \langle e,n-1|\, H_{JC}\, |e,n-1\rangle &= (n-1)\,\hbar\omega_r + \hbar\omega_a \\ \langle g,n|\, H_{JC}\, |g,n\rangle &= n\hbar\omega_r \\ \langle e,n-1|\, H_{JC}\, |g,n\rangle &= \langle g,n|\, H_{JC}\, |e,n-1\rangle = \hbar g\sqrt{n} \end{aligned} \tag{2.4}$$

And write them in matrix form

$$\begin{pmatrix} (n-1)\hbar\omega_r + \hbar\omega_a & \hbar g\sqrt{n} \\ \hbar g\sqrt{n} & n\hbar\omega_r \end{pmatrix} \tag{2.5}$$

We now observe the symmetry of the Hamiltonian that arises from the interaction terms ($\langle e, n-1| H_{JC} |g, n\rangle$) and ($\langle g, n| H_{JC} |e, n-1\rangle$) which conserve the total number of excitations. We can diagonalize this matrix leading to

$$E_\pm = \frac{(2n-1)\hbar\omega_r + \hbar\omega_a}{2} \pm \sqrt{\hbar^2 \left(\frac{\omega_r - \omega_a}{2}\right)^2 + \hbar^2 g^2 n} \tag{2.6}$$

For the resonant case, i.e. when the detuning is close to zero ($\omega_r = \omega_a$), $E_\pm = n\hbar\omega_r \pm \hbar g\sqrt{n}$. Due to strong coupling, the energies split by a factor $2\sqrt{n}\hbar g$ in an effect known as *vacuum Rabi mode splitting*. In this situation, atom and cavity constantly exchange excitations which can be observed in time as *vacuum Rabi oscillations*. The eigenstates of the system become symmetric and anti-symmetric superposition of atom and photon states (equation 2.7)

$$|\pm, n\rangle = \frac{1}{\sqrt{2}} \left(|g, n\rangle \pm |e, n-1\rangle\right) \tag{2.7}$$

2.2. Quantum dots in circuit QED

An implementation of a cavity QED system by means of superconducting electronic circuits was proposed in [8] and demonstrated in [1], opening a field called circuit quantum electrodynamics (circuit QED). In this realization, the cavity is realized by a superconducting coplanar waveguide resonator and the 'atom' is implemented as two superconducting islands, a so-called *Josephson Junction* where the collective behaviour of electrons exhibits the properties of a two level system, a charge qubit in this case. Another possibility to realize a two level system are solid state quantum dots (QDs). QDs are formed by confining electrons in all three spatial dimensions on a small island coupled only weakly to the surrounding environment. This report deals with an hybrid system where gate defined lateral semiconductor QDs are coupled to a resonator. Lateral QDs [9] are formed on a semiconductor heterostructure where electrons are confined at the interface between two semiconductors such as gallium arsenide (GaAs) and aluminum gallium arsenide (AlGaAs), see Fig. 2.2a.

Since the bandgap of AlGaAs is larger than that of GaAs, a step in the conduction band occurs at the interface (see Fig. 2.2b). As it is energetically more favourable, weakly bound electrons in the n-doped region travel into the GaAs region but remain close to the interface plane due to the charge screening, i.e. electric field built up by the holes left behind [9]. The conduction band bends because the Fermi energy has to be constant across the whole structure. Electrons are free to move on the interface plane but are confined in the direction normal to it, forming a so-called two dimensional electron gas (2DEG). Due to confinement, electronic states are assumed to be quantized in the direction normal to the 2DEG plane. However the quantization energy is assumed to be large, such that electrons can remain in their ground state [9]. QDs are defined by depleting the 2DEG in certain regions applying negative potentials through metallic gates on top of the structure, as shown in Fig. 2.3.

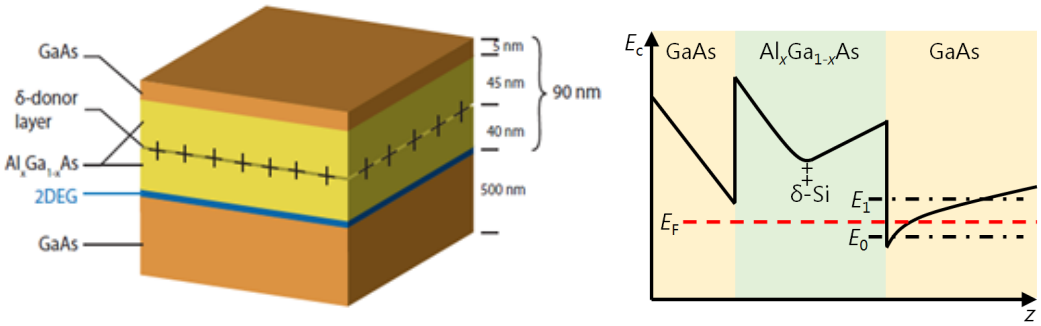

(a) (b)

Figure 2.2.: (a) Schematic of a GaAs/AlGaAs heterostructure with a 2DEG confined 90 nm below the surface (adapted from [10]). (b) Conduction band diagram for a GaAs/AlGaAs heterostructure such as in (a).

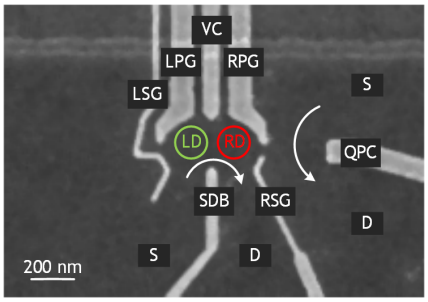

Figure 2.3.: SEM image of the metallic gates that define the confinement potentials for a DQD.

QDs are usually coupled to reservoirs such that electron transport occurs by tunnelling of electrons into the QD and out. If the 2DEG is depleted in such a way that two QDs are formed next to each other, a double quantum dot (DQD) can be formed.

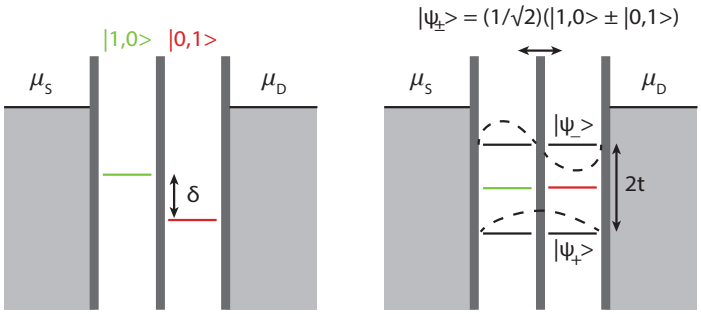

(a) (b)

Figure 2.4.: (a) Schematic of individual levels in a DQD with an energy detuning δ. (b) The interdot tunnel coupling t hybridizes the states $\psi_\pm$ describing an effective two level system.

To model a DQD as an effective two level system let us start by considering both dots initially uncoupled. A Hamiltonian that describes the configuration is given in the basis of charge states [9]

where $|1,0\rangle$ ($|0,1\rangle$) denote the state of an electron occupying the left (right) dot (see Fig. 2.4a).

$$H = \frac{\delta}{2}\sigma_z \tag{2.8}$$

where σ_z is again the Pauli z-operator, this time given by $\sigma_z = |0,1\rangle\langle 0,1| - |1,0\rangle\langle 1,0|$. The energy detuning between both states is given by $h\delta$, where $\delta = \omega_\delta/2\pi$. Figure 2.4a shows a schematic of the two ground state energy levels the DQD either in the state $|1,0\rangle$ or $|0,1\rangle$. When the two dots are tunnel coupled, an interaction term must be added to the Hamiltonian accounting for the tunnelling of an electron from one dot to another at a rate t/h, called inter-dot tunnel coupling.

$$H = \frac{\delta}{2}\sigma_z + t\sigma_x \tag{2.9}$$

Where σ_x is the Pauli x-operator given by $\sigma_x = |0,1\rangle\langle 1,0| - |1,0\rangle\langle 0,1|$. The inter-dot tunnel coupling mixes charge states and hence leads to a an hybridization of the electron states in the left and right dot. When δ becomes small, the eigenstates of the system become symmetric and anti-symmetric superposition of the initially uncoupled states, as given in equation 2.10. At zero detuning the energies of these states would be degenerate and hence split by a factor of $2t$. The new eigen-energies of the system are given by equation 2.11.

$$\psi_\pm = \frac{1}{\sqrt{2}}\left(|0,1\rangle \pm |1,0\rangle\right) \tag{2.10}$$

$$E_\pm = \pm\frac{1}{2}\sqrt{\delta^2 + (2t)^2} \tag{2.11}$$

As depicted in Fig. 2.4b, the hybridized states $\psi_\pm$ describe an effective two level system with transition frequency $\hbar\omega_q = \sqrt{\delta^2 + (2t)^2}$, which can in turn be coupled to a cavity. The resulting interaction is formally equivalent to a dipole coupling between the resonator and the DQD and is formally analogous to cavity QED. Please refer to [11] for a formal treatment of a DQD coupled to a resonator. Although coupling of DQD to cavities has been realized, up to date we are not aware of any documented observation of strong coupling in such architecture. Strongly coupling semiconductor QDs to a superconducting resonator would eventually allow to integrate spin degrees of freedom (which are known for having considerably larger coherence times) into a circuit QED architecture.

CHAPTER 3

Measurement Setup

3.1. Sample

The experiments covered in this report were performed using the device depicted in Fig. 3.1. It is based on a selectively doped semiconductor heterostructure which is grown by molecular beam epitaxy (MBE) [12]. As mentioned in section 2.2, a 2DEG is formed roughly 90 nm below the surface at the interface of n-doped AlGaAs on top of GaAs.

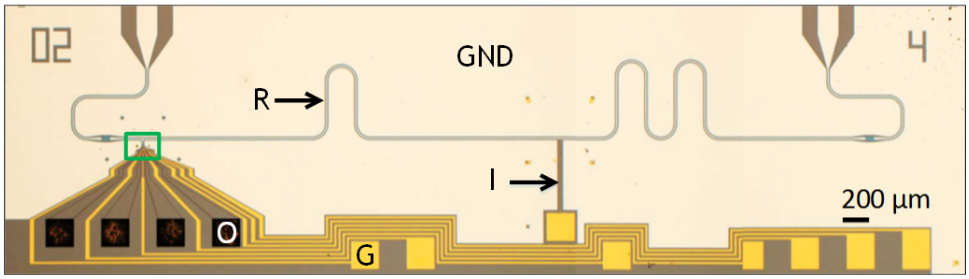

Figure 3.1.: Optical photograph of the sample design. Labels are: resonator (R), ground plane (GND), ohmic contacts (O), metallic top-gates (G), inductor (I). Metallic top-gates are shown in gold. The 2DEG is located in dark grey regions.

On top of the semiconductor heterostructure wafer a microwave cavity is added. It is fabricated as a coplanar waveguide (CPW) resonator in a photo-lithographic process using aluminium, which is superconducting below $T_{c,Al}$= 1.2 K. Please note that AlGaAs is etched away below the region where aluminium is deposited, such that there is no 2DEG below the resonator. In the sample used for the measurements presented in this report, the external quality factor was Q_{ext} = 2060 which corresponds to a decay rate of $\kappa/2\pi$=3.35 MHz. The resonance frequency ν_r=6.852 GHz is mainly determined by the length of the resonator which is about 8 mm.

On top of the remaining GaAs area, metallic gates are defined by a combination of photo-lithography and electron beam lithography (EBL), such that on the left hand side of the resonator at an anti-node of the electric field, a DQD can be formed (area enclosed in a green rectangle in Fig. 3.1). Figure 3.2 shows the sample gate design and indicates the following naming convention: left side gate (LSG), left plunger gate (LPG), central gate (VC), right plunger gate (RPG), right

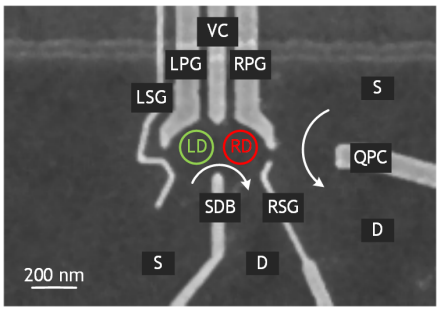

Figure 3.2.: SEM image of the sample showing its gate design.

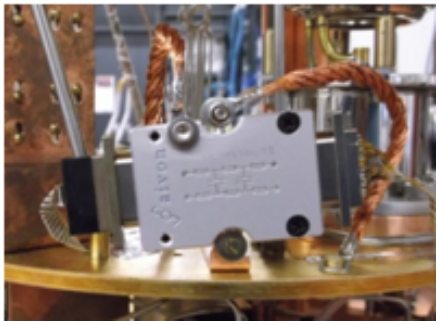

Figure 3.3.: Low pass frequency *Aivon* filter.

side gate (RSG), source drain barrier (SDB), quantum point contact (QPC), source (S), drain (D). Arrows in Fig. 3.2 indicate paths where current flows. Coupling between the DQD and the resonator is achieved by directly connecting LPG to the center conductor of the CPW. In order to DC bias this gate, an inductor at the center of the resonator is added, as shown in Fig. 3.1.

3.2. Cryogenics

In order to observe quantum effects the thermal occupation of all relevant degrees of freedom needs to be below one quantum of energy. As discussed in chapter 6, various energy scales come into play regarding quantum dots. For the microwave resonator, the energy scale is given by that of a single microwave photon $h\nu_r$ putting a limit to the thermal energy $k_B T \ll h\nu_r$. This condition can be satisfied in a *dilution refrigerator* [13] which can reach temperatures down to $\approx$ 20 mK. The dilution refrigerator used in our experiments employs a *pulse tube cooler* with a helium working medium to pre-cool the first two stages to 70 K and 4 K. Cooling to 20 mK on the lowest stage is achieved by extracting heat through the evaporation of ^{3}He in a ^{3}He ^{4}He mixture.

To reduce the heat load to the lowest temperature stage, we use stainless steel cables which have a lower conductivity ($\approx$ 0.1 W mK^{-1}) in comparison to regular copper cables ($\approx$ 20 W mK^{-1}). Additionally, attenuators are added at different temperature stages in order to thermalize the outer and inner conductor of the cables to the respective temperatures (see Fig. 3.4). Attenuators also reduce thermal radiation coming from room temperature equipment, helping the physical temperature (lattice vibrations) and the electromagnetic field temperature (photon excitations) to remain low. Another measure to reduce the thermal radiation entering the sample are circulators added between the sample output and the amplifiers. Circulators act as a one way valve for microwave radiation, allowing it to propagate only in one direction. In this way the noise emitted by the amplifiers towards the sample is filtered and deposited in 50 Ω terminations (see Fig. 3.4).

On the DC lines side, a customized low pass *Aivon* filter has been added. This filter was modified (Fig. 3.3) by Peter Märki from the Nanopysics Group in order to capacitively connect it to the ground of the cryostat, allowing for good thermalization. The addition of this modified filter brought a significant improvement in the measured electronic temperature of the sample, reducing it from 130 mK to 58 mK.

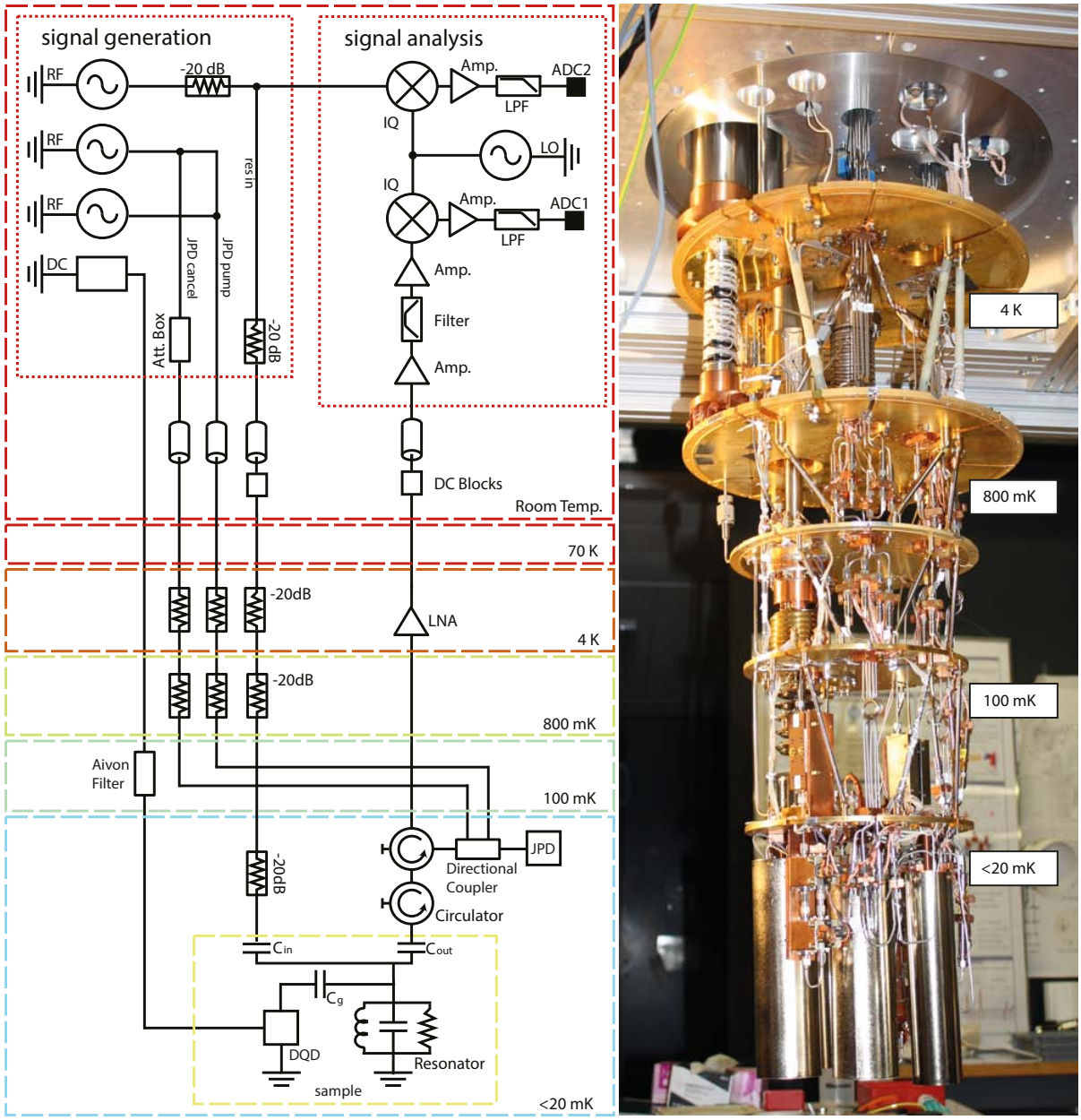

Figure 3.4.: Left: Schematics of the experimental setup. Signal generation and signal acquisition takes place at room temperature. Three RF generators are shown, one is used as to generate the resonator signal input, while the other two are used to operate and calibrate a parametric amplifier. The room temperature DC part of the setup consists of several DC sources and meters required to operate the gates of the sample and measure currents. The JPD block consists of a setup indicated in Fig. 3.5. The aivon filter is depicted in Fig. 3.3. Five temperature stages are found inside the cryostat. Right: Photo of the open cryostat indicating different temperature stages. Figure layout adapted from [14].

3.3. Signal generation, amplification and acquisition

Our experiments involve a variety of electrical signals which are generated by room temperature equipment and can be divided into the following groups: synchronization and trigger signals, continuous microwave signals, and DC signals.

To perform precise measurements all devices need to be commonly synchronized. This is achieved by phase locking each device to a common 10 MHz reference provided by a Rubidium clock (SRS FS745). This clock is stabilized against drifts in the clock frequency and provides a reference signal with ultra-low phase noise. Typically many repetitions of a measurement are performed to acquire enough information. These repetitions are controlled by a free running external trigger usually set to a value of 25 μs.

Continuous microwave signals are generated by Rhode and Schwarz microwave sources, see Fig. 3.4. One source (RF) is used to apply coherent tones to the resonator. Another source (LO) is used as a local oscillator for demodulation of the resonator output signal to an intermediate frequency (IF). Two further sources are used to pump and calibrate a *parametric amplifier*.

Amplification Measurements of signals coming out of the resonator are enabled by the use of a parametric amplifier (paramp) and cryogenic low noise amplifiers (LNA) installed respectively at the lowest and at the 4 K stage of the cryostat. The noise level is quantified by the noise temperature which is the equivalent temperature of a black body radiator in front of a noiseless amplifier producing the same amount of noise as our system. Frii's law for the noise temperature shows that the system noise is dominated by the first amplifier in the detection chain

$$T_{sys} = T_{amp} + \frac{T_{rest}}{T_{amp}} \tag{3.1}$$

During the course of the project, we introduced a paramp into our setup as the first amplifier in the detection chain. The device, shown in Fig. 3.5, is called a Josephson Parametric Dimer (JPD) [4]. It works in reflection and consists of two non-linear coupled resonators. The non-linearity arises from superconducting quantum interference devices (SQUIDS) realized by means of Josephson Junctions whose inductance can be tuned by means of an applied magnetic field. For parametric amplification to occur, the JPD needs to be pumped by a high power RF signal. The gain and bandwidth of the JPD are tunable, and the effective noise photon number N_0 after amplification lies between 0.5 and 10 photons ([4], [15], [16], [17]). In contrast, LNAs implemented using high electron mobility transistors (HEMT) feature effective noise photon numbers between 30 and 200 ([18], [19], [20], [21]). As described in section 7.2, due to the quantum character of the JPD operation it is possible to measure an estimate for the effective noise photon numbers in our setup. This number was found to be around 5 for the JPD, and around 100 for our HEMT amplifier. The deviation of N_0 from the vacuum for the JPD is due to cable and insertion losses in front of it.

At room temperature, the signal is further amplified by $\approx$ 60 dB (ZFL-500LN+, Mini-Circuits) to a level where it becomes detectable by digital electronics. The amplified high frequency signal is filtered by an analogue low pass filter (VLFX-225, Mini-Circuits) and converted down to an IF of typically 25 MHz. For down conversion we use an IQ mixer (IQ4509MXP, Marki) driven by a local oscillator which is phase locked to the input microwave signal. The resulting IF signal is again low pass filtered (SLP-50+, Mini-Circuits), digitized by an *Acqiris Data Acquisition Board* (AP240) and finally passed onto a *Xilinx Xtreme DSP* board where data processing, averaging and recording of the measurement outcome takes place.

The Xilinx Xtreme DSP board has a sampling period of 10 ns on two channels but can be programmed to perform arbitrary operations on the data before averaging, which is the key feature in

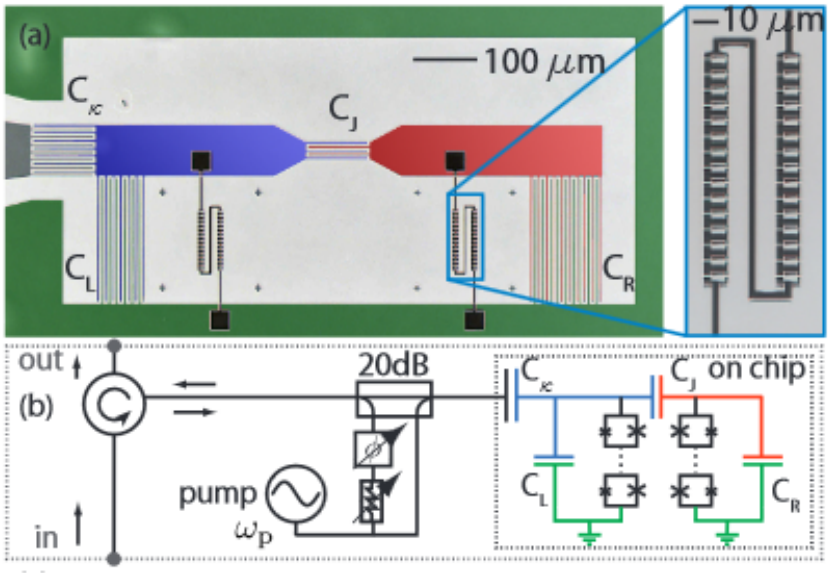

Figure 3.5.: Optical false colour image of a JPD and schematic lumped element circuit representation. The device operates in reflection. A circulator establishes the signal flow, coupling the input signal to the paramp via a directional coupler and coupling the reflected amplified signal to the output line. The directional coupler also allows to couple a pump signal to the paramp input with -20dB of attenuation. Since the pump signal power is usually strong, some power might get reflected together with the amplified signal. A pump cancellation signal is sent via another port of the directional coupler in order to destructively interfere with any reflected pump signal. Figure adopted from [4].

our signal processing schemes. The reason is that we perform non-linear operations on the measured data, and these do not commute with averaging.

CHAPTER 4

Coplanar Waveguide Resonators and Wire Bonds

During a considerable part of the project our samples were not working as expected. Namely, our resonators had a very low quality factor. This chapter tries to summarize some efforts we made to try to model possible origins for the observed low quality factors in our resonators. In chapter 2 we considered cavities as harmonic oscillators. We start by describing the implementation of the cavity as a superconducting transmission line resonator.

4.1. Coplanar waveguide resonators

The coplanar waveguide (CPW) ([22], [23]) is a type of transmission line [24] supporting quasi-TEM modes [25]. It can be thought as the planar counterpart of a co-axial cable, having the ground plane on the same plane as the center trace, as shown in Fig. 4.1.

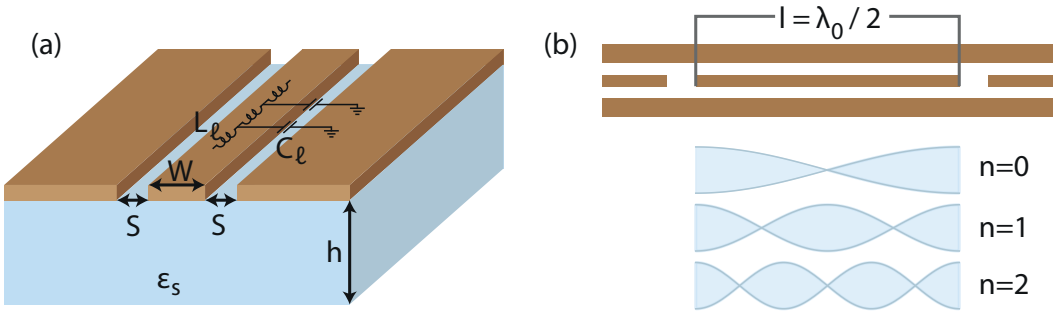

Figure 4.1.: (a) Schematic representation of a CPW, (b) first three resonant modes of a CPW. Image adopted from [26].

We can also think of a CPW as two coupled slot lines, whose geometry is defined by the width w of the center conductor, the gap s, and the height h of the substrate (Fig. 4.1). The relative permittivity ϵ_s of the substrate is also a design parameter. The thickness t of the conductive film is usually much smaller than all other dimensions, and hence commonly assumed as flat. The characteristic impedance of a loss-less transmission line in terms of its capacitance C_l and inductance L_l per unit

length can be expressed as [24]

$$Z_0 = \sqrt{\frac{L_l}{C_l}} \tag{4.1}$$

and its phase velocity can be expressed as the following

$$v_{ph} = \frac{1}{\sqrt{L_l C_l}} = \frac{c}{\sqrt{\epsilon_{eff}}} \tag{4.2}$$

where c is the speed of light in free space and ϵ_{eff} is the effective permittivity of the substrate. At non-zero frequencies the electric and magnetic field have longitudinal (i.e. in the direction of propagation) components, and hence the electromagnetic mode propagating in a CPW is referred as a quasi transverse electromagnetic (TEM) [24], [25]. Since the characteristic impedance of non TEM modes is not uniquely defined, there is no unique analytical expression for the characteristic impedance of a CPW. However, C_l can be estimated by means of conformal mapping techniques [27] which map the CPW structure into an effective parallel plate capacitor from which an effective permittivity ϵ_{eff} can be calculated. Having an expression for C_l, from equation 4.2 an expression for L_l can be obtained. In this way, expressions for C_l and L_l read [27].

$$C_l = 4\epsilon_0 \epsilon_{eff} \frac{K(k_0)}{K(k_0')} \tag{4.3}$$

$$L_l = \frac{\epsilon_{eff}}{c^2 C_l} = \frac{\mu_0}{4} \frac{K(k_0')}{K(k_0)} \tag{4.4}$$

Where K is a complete elliptic integral with modulus $k_0 = w/w + 2s$ and $k_0' = \sqrt{1 - k_0^2}$. Note that the inductance only depends on the geometry of the CPW, while the capacitance includes a dependance on ϵ_{eff}. Combining equations 4.1, 4.3, and 4.4 an expression for the characteristic impedance of a CPW can be obtained.

$$Z_0 = \frac{1}{4} \sqrt{\frac{\mu_0}{\epsilon_0 \epsilon_{eff}}} \frac{K(k_0')}{K(k_0)} \tag{4.5}$$

The effective relative permittivity depends on the geometry as well as on the permittivity of the substrate and the medium above the CPW:

$$\epsilon_{eff} = \epsilon_m + \frac{\epsilon_m - \epsilon_s}{2} \frac{K(k_1)}{K(k_1')} \frac{K(k_0')}{K(k_0)} \tag{4.6}$$

where $k_1 = \sinh(\pi w/4h_s)/\sinh(\pi(w+2s)/4h_s)$ and $k_1' = \sqrt{1 - k_1^2}$. In the limit of large substrate thickness $h_s \to \infty$, k_1 tends to k_0

$$\lim_{h_s \to \infty} \epsilon_{eff} = \epsilon_m + \frac{\epsilon_m - \epsilon_s}{2} = \frac{\epsilon_m + \epsilon_s}{2} \tag{4.7}$$

The medium surrounding our CPWs is usually vacuum, and hence $\epsilon_m = 1$. An intuitive interpretation of equation 4.7 is that the energy of the electric field gets equally distributed in vacuum and in the substrate, thus the effective permittivity is just the mean value of both. In this way one can tune the CPW dimensions to obtain a desired intrinsic impedance. To be compatible with the rest of the measurement setup, our CPWs are designed to have $Z_0 \approx 50\ \Omega$

4.2. Wire bonds and their influence

As shown in 4.2, CPWs support two propagating modes: an even mode and an odd (also called 'slot-line') mode. The desired mode profile of a CPW is symmetric [23], with both ground planes on either side of the center trace held to the same voltage. However, asymmetries and discontinuities in the structure can lead to the excitation of parasitic slot-line modes [28], which are in general undesired [29].

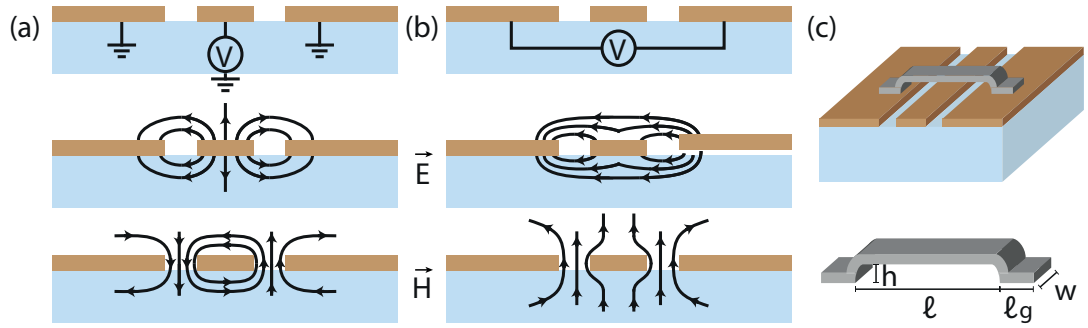

Figure 4.2.: (a) Even (quasi-TEM) mode and (b) odd (slot-line) mode of the CPW. Top: Excitation of the modes. Middle: Schematic of the transversal electric field. Bottom: Schematic of the transversal magnetic field. (c) schematic of an airbridge. Image adopted from [26].

Intuitively, slot line modes may get excited whenever there is potential difference between both ground planes (see Fig. 4.2). In order to suppress them, crossover connections can be made between the ground planes forcing their potential to be the same. Free standing crossovers, known as airbridges, have been a conventional solution in microwave CPW technology, and fabrication processes have been developed to include them on superconducting microwave circuits. Two important questions then arise, namely, what influence such crossover connections have on the performance of a CPW, and where to place them. In regard to their influence, airbridges have been proved to be an effective solution to suppress parasitic modes, but they may also present a source of loss. There have been recent attempts to characterize the losses introduced by airbridges in superconducting microwave resonators [30].

Due to the additional micro-fabrication work required to include airbridges on superconducting CPWs, connections between the different ground planes are alternatively made using wire bonds. In our lab, some tests of the influence of wire bonds on superconducting CPWs have been made [31], showing that they also help to attenuate parasitic modes.

During a considerable part of this project, our resonators had a very low quality factor, making them unsuitable to perform any experiments. Since we used wire bonds on our resonators, we intended to test whether the placement of wire bonds had a negative influence on our resonator samples. To this end, we made tests of our resonator design fabricated on a Niobium (conductor)/Sapphire (substrate) sample. Having a bonding plan, we measured the scattering parameters of our resonator at a temperature of 4.2 K for each step of bonding, and extracted quantities of interest such as the Q factor.

Figure 4.3 shows the bonding plan we followed to test the effect of wire bonds on our resonator design. For each bonding step we measured the scattering parameters using a 4-port vector network analyzer (VNA) (Agilent Technologies N5230C PNA-L) for different excitation powers going from -70 dBm to 0 dBm in steps of 5 dBm.

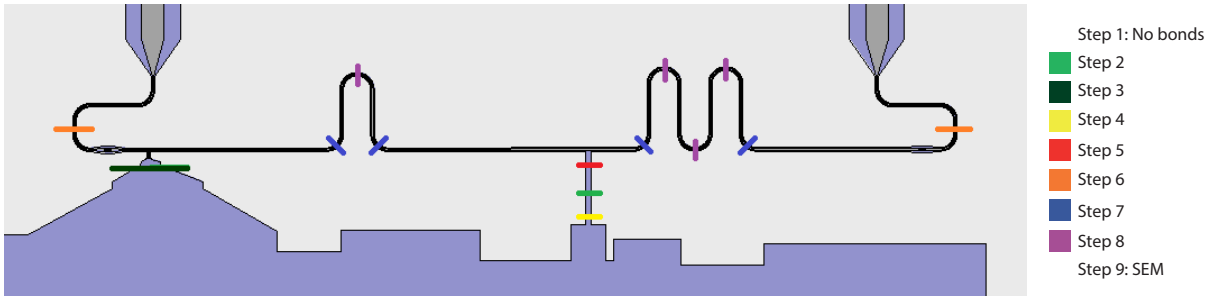

Figure 4.3.: Schematic of the bonding plan used for our bonding tests.

We tried to place wire bonds in such a way that symmetries were recovered. Considering that the path difference between the two slots of a CPW may lead to potential differences between the ground planes, we tried to place wire bonds wherever the structure bent or had discontinuities. Wire bond across the center inductor as well as across the mesa have the purpose of interconnecting the split ground plane. As we will show later, a guideline for this type of bonds is to place them as close as possible to the discontinuity, i.e. to the center trace, such that they present a low inductance path for the current. We used a dipstick setup for the experiment, which consists of a stick to which the sample is attached to and which is dipped in liquid helium allowing to reach a temperature of 4.2 K. On top of the dipstick are SMA connectors which are connected to the VNA. In order be able to get an estimate of the internal and external quality factors of our resonators, we calibrated the cables from the VNA ports down to the input ports the sample.

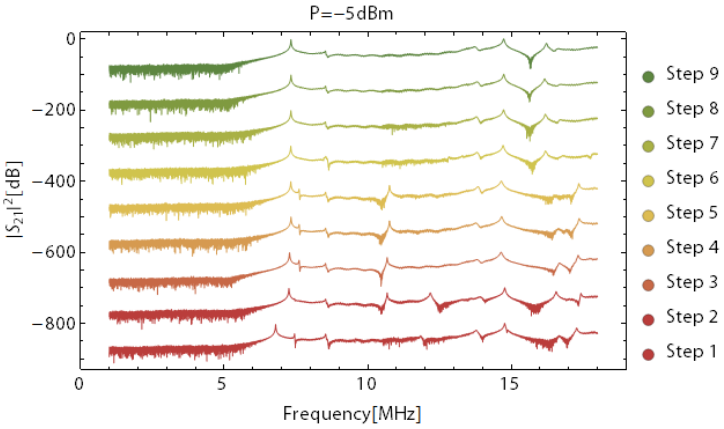

Figure 4.4.: Transmission spectra for each bonding step at P=-5 dBm. An offset of 100 dB has been added between the traces for clarity.

Figure 4.4 shows the power transmission spectra measured after each step of bonding. Near 7 Ghz we observe a transmission resonance, as expected for the first resonance mode of our sample design. The second resonance mode is also observed around 15 GHz. All peaks in between these two resonances are associated with parasitic slot-line modes in our resonator. We note how these parasitic resonances qualitatively get suppressed as we add wire bonds according to Fig. 4.3. We fit the first resonant mode of these traces to the theoretical scattering matrices [24] and extract the internal, external and loaded quality factors of our resonator and plot them as a function of the bonding step (Fig. 4.5). We observe an increase in the internal quality factor of our resonator, specially after steps 3 and 4 of bonding. Referring back to Fig. 4.3 we note that these steps correspond to bonds which interconnect the split ground plane in our sample. This is an indication that such discontinuities

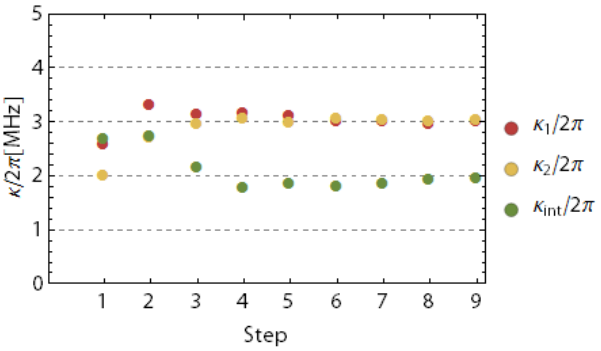

Figure 4.6.: Internal and external decay rates after each bonding step.

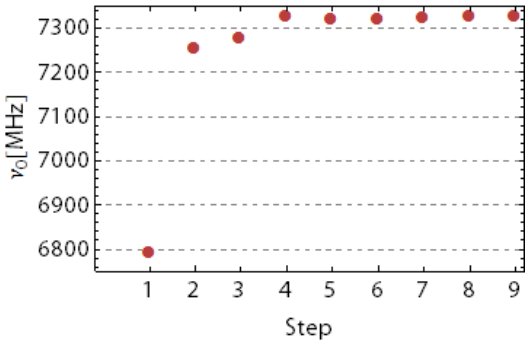

Figure 4.7.: Resonance frequency of the first resonant mode after each bonding step.

lead to strong internal losses and suggest that interconnections should be carefully made in order to restore the symmetry.

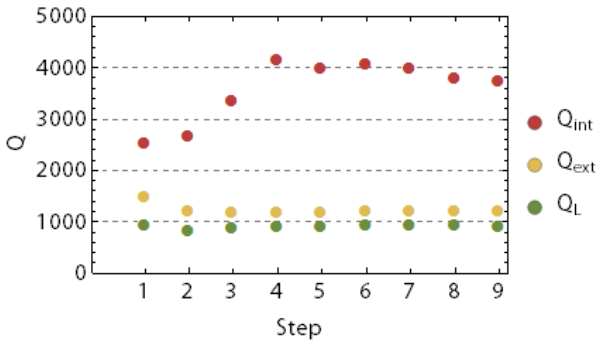

Figure 4.5.: Internal, external, and loaded quality factors after each bonding step.

In Fig. 4.6 we plot the external and internal decay rates κ of our resonator. Please note that the external decay rates $\kappa_{1(2)}$ are given by the coupling capacitances to the resonator, which by design should be equal. However, we observe that they only become symmetric after step 6 of bonding. As expected from Fig. 4.5 the internal decay rate decreases during steps 3 and 4. In Fig. 4.7 we plot the resonance frequency of the first mode after each bonding step. The shift in resonance frequency after step 2 and 3 indicates a change in the propagation constant of the CPW, namely C_l and L_l.

The goal of our bonding tests was mainly to verify whether presence or absence of wire bonding on our resonator design had a strong influence on the quality factor. We note the loaded quality factor in Fig. 4.5 stays roughly constant even if no wire bonds are added. This suggests that wire bonding problems are not likely a reason for the very low quality factors that we measured in our real samples. We also observe that, bonds interconnecting the split ground planes in our design are the most important ones, in terms of resonator quality factor. From Fig. 4.4 we also note that wire bonds qualitatively suppress parasitic modes. However, these measurements have several drawbacks and can only be regarded as a qualitative measure. First of all, with a wire diameter of 25 μm and a typical length of 1 mm, wirebonds have an inductance of the order of 1 nH and an impedance of 40 Ω at 6 GHz, making them an ineffective shunt. Furthermore, wire bond results do not produce uniform and reproducible results [26]. On the other hand, the dipstick measurement scheme used for our experiment has some drawbacks. For instance, since wire bonds are made of a mix of Aluminium

and Silicon, they do not reach the superconducting state in a dipstick due to its critical temperature T_c =1.2 K which is well below that of liquid helium. The possibility of a different behaviour at lower temperatures can not be totally excluded.

With this in mind, we suggest the introduction of airbridges for future sample designs. From the measurements presented in this section, an improvement in the quality factor of the resonator as well as a closer match to designed parameters such as external decay rates can be expected.

4.3. A short note on airbridge design

The term impedance miss-match refers to a difference in the characteristic impedance of a transmission line. At the interface where impedance miss-match occurs, two processes take place: part of the incident signal power is reflected and part is transmitted. Defining Z_0 and Z_L as two different characteristic impedances, the reflection coefficient is given by equation 4.8.

$$\Gamma = \frac{Z_L - Z_0}{Z_L + Z_0} \tag{4.8}$$

The transmission coefficient is defined as $T = 1 - \Gamma$. Referring to Fig. 4.2, we can think of an airbridge as adding a shunt capacitance between the center conductor and the ground plane of a CPW. Therefore, an airbridge introduces an impedance miss-match and reflections occur. If we consider the airbridge as a lumped element shunt capacitance, the impedance of the transmission line gets modified by the additional capacitance as

$$Z_0^{'} = \frac{1}{\left(C_{airbridge} + C_l\right) v_{ph}} \tag{4.9}$$

The reflection coefficient at this point in the CPW will be

$$\Gamma = \frac{Z_0^{'} - Z_0}{Z_0^{'} + Z_0} = -\frac{1}{1 + 2\frac{C_l}{C_{airbridge}}} \tag{4.10}$$

where the minus sign indicates a π radians phase shift. Using equation 4.2, we rewrite equation 4.10 as

$$\Gamma = -\frac{1}{1 + 2\frac{1}{Z_0 v_{ph} C_{airbridge}}} = -\frac{1}{1 + 2\frac{\sqrt{\epsilon_{eff}}}{c Z_0 C_{airbridge}}} \tag{4.11}$$

where c is the speed of light. If we consider the capacitance of the airbridge as a parallel plate capacitor, equation 4.11 becomes

$$\Gamma = -\frac{1}{1 + 2\frac{\sqrt{\epsilon_{eff}}}{c Z_0 \epsilon_0 \epsilon_r}\frac{h}{A}} \tag{4.12}$$

where h is the airbridge height and A is the airbridge area $A = wl$ as in Fig. 4.2. From equation 4.12 we observe that the height of the airbridge should be larger compared to its width and length in order to reduce reflections. A typical value for h is on the order of 1 or 2 μm. To reduce the airbridge inductance, the width can be increased and the length can be reduced. Whether the additional shunt capacitance should be large or small, depends on the purpose of the airbridge. If the purpose of adding an airbridge is to suppress parasitic modes, the capacitance and inductance should be small. If we want to connect split ground planes, the shunt capacitance might be large and the inductance small. On the other hand, there are important points to consider when fabricating airbridges. Please refer to chapter 2 of [26] for notes on this topic.

4.4. Capacitance simulations

As we will show in chapter 6, the interaction rate g between our DQD and the resonator is given by [11].

$$g_0 = \omega_0 \Delta\alpha \left(\frac{2Z_0 e^2}{h}\right)^{\frac{1}{2}} \tag{4.13}$$

where $\Delta\alpha = \alpha_{LPG,LD} - \alpha_{LPG,RD}$ is called the differential lever arm, in our case of LPG (since as we saw in section 3.1, our DQD is coupled to the resonator via LPG). $\alpha_{LPG,L(R)D}$ is called the lever arm of LPG on the left(right) dot, and is given by the ratio of the capacitance between LPG and the left(right) dot to the total capacitance, also called self capacitance, of the left(right) dot.

$$\alpha_{LPG,L(R)D} = \frac{C_{LPG,L(R)D}}{C_{00}} \tag{4.14}$$

We hence note that g_0 is proportional to the differential lever arm. In principle we would then want strong capacitive coupling between LPG to the left dot but weak to the right dot. One way to modify these capacitive couplings is by design of the sample geometry. With the aim of increasing the differential lever arm of the sample, a couple modifications had been introduced to the DC gates in the vicinity of the DQD. We intended to quantify the effect of such geometrical modifications on $\Delta\alpha$. For this, we numerically simulated the capacitance matrix of our DQD using the finite element method (FEM) simulator *Maxwell 3D*.

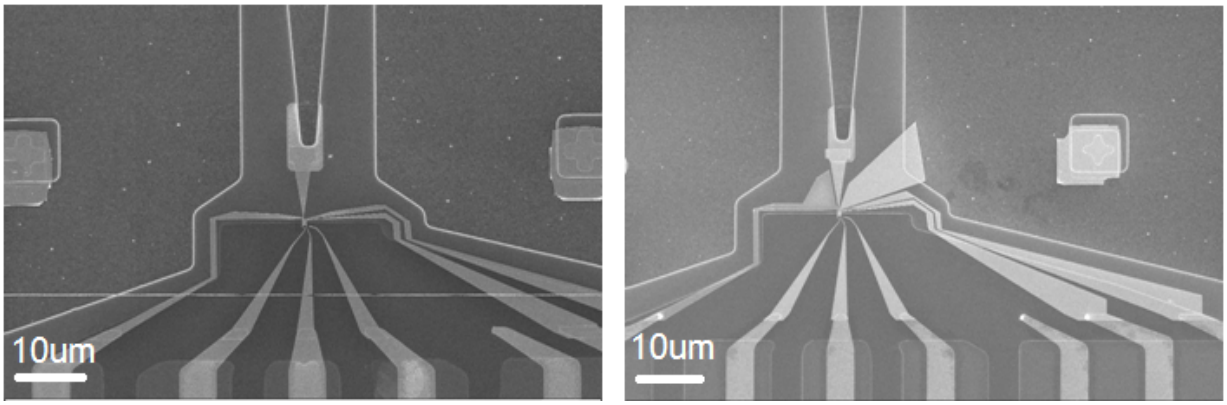

(a) (b)

Figure 4.8.: (a) SEM image of our sample without and (b) with additional metallic features.

the LPG samples the signal in the resonator at an anti-node of the electric field and couples it to the DQD. To increase the lever arm, we want this signal to couple more to the left dot than to the right dot. In Fig. 4.8 we observe metallic plates extending the area of LSG and the right ground plane. One may in principle think that the coupling between the left dot and the resonator could be enhanced, if the capacitance between LSG and LPG is increased. The reason would be that the AC signal in the LPG would couple to the LSG, and in this way act more on the left dot than on the right dot. In a similar way, one may think that by increasing the coupling between the LPG and the right ground plane, the coupling between the LPG and everything on its right side would be reduced. The above mentioned effects would then lead to an increase in the differential lever arm. The sample design shown in Fig. 4.8b is motivated by these considerations. Figure 4.9 shows

Table 4.1.: Capacitances in [fF] between the LPG and different gates in our sample model with and without metallic plates (MP) (see Fig. 4.9).

	SDB	VC	GroundLeft	GroundRight	LSG	QPC	RPG
With MP	5.07×10^{-2}	0.17	3.47	4.18	1.2	5.12×10^{-2}	7.16×10^{-2}
No MP	5.72×10^{-2}	0.32	3.62	3.49	0.41	5.84×10^{-2}	0.11
	RSG	2DEG1	2DEG2	2DEG3	2DEG4	LD	RD
With MP	4.68×10^{-2}	0.29	9.43×10^{-2}	9.48×10^{-2}	0.29	1.84×10^{-2}	2.99×10^{-3}
No MP	5.38×10^{-2}	0.41	0.12	0.12	0.39	1.96×10^{-2}	3.41×10^{-3}

Table 4.2.: Estimated resonator-DQD coupling $g_0/2\pi$ (equation 4.13) based on capacitances from table 4.1. Resonance frequency is assumed to be 6.8 GHz and $Z_0 = 50\ \Omega$.

Including metallic plates	59 MHz
No metallic plates	60 MHz
Including metallic plates and contribution from LSG	79 MHz
No metallic plates and contribution from LSG	80 MHz

a 100 μm side cubic section of the region around our DQD. We included in this model all relevant gates and simulated the depletion of the 2DEG by adding a thin metallic film (15 nm thick) 90 nm below the surface. To simulate a DQD, we further isolated 2 circular regions of 80 nm radius in the 2DEG, and placed them at the spot where the DQD is expected to be formed. We then proceed to calculate the capacitance matrix of the structure with and without the features discussed above.

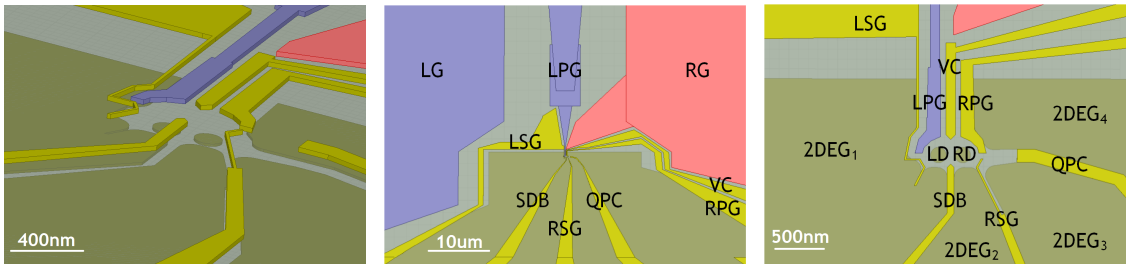

(a) (b) (c)

Figure 4.9.: CAD model of our sample. (a) 3D view showing a simulated depletion of the 2DEG 90 nm below the surface. (b) Top view showing sample gates and ground planes to the left and right of the resonator plunger gate. (c) Zoom of top view indicating the double dot and the naming convention for the depleted 2DEG, LG and RG stand for left and right ground respectively.

The motivation for adding the metallic plates was to achieve a greater differential lever arm and thereby a larger value for $g/2\pi$. As seen in table 4.1, while the coupling from the resonator gate (LPG) to the left side gate (LSG) is effectively increased, the influence on the differential lever arm is negligible even if we calculate an effective capacitance between the resonator and the dots as the sum of the capacitances between the LPG and the LSG to the dots (see table 4.2). This is due to the fact that the capacitance from the different gates to the dots does not get altered by the presence of the metallic plates.

We further tried to consider possible modifications to the gate design of our sample in order to increase the differential lever arm. One possibility, as considered in previous work [10], is to use asymmetric plunger gates. Here we intended to get a quick estimate of how much increase could

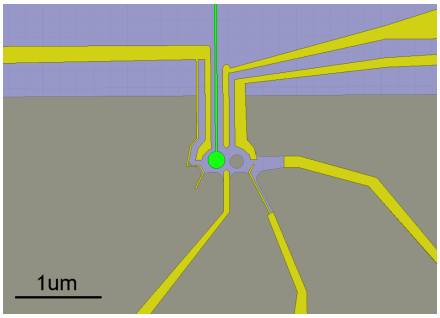

Figure 4.10.: Schematic of asymmetric plunger gate design. The LPG is extended on top of the left dot to increase its capacitive coupling.

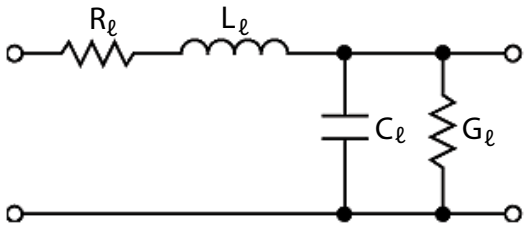

Figure 4.11.: Distributed element circuit model of a transmission line.

in principle be achieved with such a geometry. We modified the sample design to obtain maximum surface overlap between the LPG and the left dot (see Fig. 4.10) and again calculated the capacitance matrix of the structure. We calculate a factor of 2 increase in g_0, which although desirable, would still not allow to reach the strong coupling regime. Our simulation assumes that a DQD potential can be formed without applying any potential to the LPG. Please note that somewhat similar designs have been tested finding an increase in g_0 but a difficulty to tune the inter-dot tunnel coupling, due to the close location of LPG to the central barrier [10].

4.5. DC gate lines and their high frequency response

As shown in Fig. 3.1, the gate lines of our sample extend nearby the resonator ground plane. Wirebonds connecting the PCB and the gate lines are placed on the square pads at the end of each gate line. As depicted in Fig. 4.12, the gate line going closest to the resonator ground plane resembles a slot line waveguide, which has a length comparable to the resonator length. In general we want excitations being generated at the DQD to couple only to the resonator, and we want the DQD to be isolated from external excitations. One question of interest is then what the high frequency response of gate lines looks like, since they may offer a path for high frequency excitations to go into and out of the DQD. Ideally, the gate lines should show a high impedance at high frequency, such that the signal coming from the DQD does not escape through them, and high frequency noise from the measurement set up is filtered out.

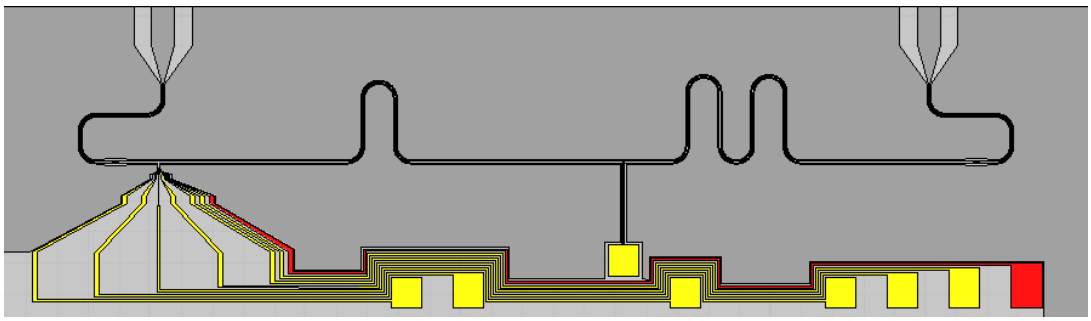

Figure 4.12.: Schematic of the gate lines in our sample design. The red highlighted gate going closest to the resonator ground plane resembles a slot-line transimission line.

We intended to simulate the high frequency response of our gate lines using a 3D FEM simulator

(HFSS, Ansoft) to calculate the scattering parameters of the structure. In an ideal case, the red-highlighted gate line in Fig. 4.12 going closest to the ground plane forms slot-line waveguide. The discontinuities in the structure, such as bendings and size changes, make the ideal waveguide a very bad one. We expect an impedance mismatch at the end of the gate line, where wirebonds are placed to connect to the PCB. This leads to reflections and a resonance at high frequency, close to 8 GHz. The addition of further gate lines close to the red-highlighted one, effectively change the intrinsic impedance (via changes in the capacitance and inductance per unit length), and hence the propagation constant of the slot-line like waveguide.

Having high frequency resonances in the gate lines, even if they are weak ones, is highly undesired. We thus suggest possible improvements for the sample design in order increase the impedance at high frequency of the gate lines. Gate lines should be shorter, this would move possible resonances to higher frequencies than the frequency range in which we are interested (6 to 8 GHz). Evaluating the possibility to reduce the number of gates would also be worth. Finally, it may be good to consider the addition of micro-strip filters in order to filter out high frequency noise coming from the measurement set up. Such filters should be added to each gate line and placed as close as possible to the DQD. To motivate the use of micro-strip filters, we give a quick overview of how such filters can be designed and what responses can be obtained.

Microwave filter design started around the years of the second world war. Various methods for filter design exist, the most common of them being the so-called *insertion loss method*. The design usually begins with filter prototypes normalized in impedance and frequency, which are then transformed to the desired impedance and frequency. Filter design is usually made for lumped element circuits and works well at low frequencies, but is difficult to implement at high frequencies. Two mathematical tools allow us to modify the designs to use transmission line sections, namely the *Richards Transformation* and *Kuroda's Identities*.

To introduce the Richards transformation let us start by remembering the input impedance of a transmission line. The distributed element transmission line model represents a transmission line as an infinite series of two-port elementary components, each representing an infinitesimally short segment of the transmission line. The primary line constants are given by a resistance R_l, inductance L_l, capacitance C_l and conductance G_l per unit length, as shown in Fig. 4.11. The voltage and current in an infinitesimal section of line can be expressed as (equation 4.15)

$$\begin{aligned} \frac{\partial V(x)}{\partial x} &= -(R_l + jwL_l)I(x) \\ \frac{\partial I(x)}{\partial x} &= -(G_l + jwC_l)V(x) \end{aligned} \tag{4.15}$$

Taking the second spatial derivative of equation 4.15 and solving for the voltage and current yield the so-called *Telegrapher's Equations*.

$$\begin{aligned} \frac{\partial^2 V(x)}{\partial^2 x} &= \gamma^2 V(x) \\ \frac{\partial^2 I(x)}{\partial^2 x} &= \gamma^2 I(x) \end{aligned} \tag{4.16}$$

Where we have defined the propagation constant $\gamma = \sqrt{(R_l + jwL_l)(G_l + jwC_l)}$. These are wave equations which are solved by any linear combination of space-time. Plane waves with equal

propagation speed in the forward and reverse directions are direct solutions.

$$\begin{aligned} V(x) &= V^+ \exp^{-\gamma x} + V^- \exp^{\gamma x} \\ I(x) &= I^+ \exp^{-\gamma x} + I^- \exp^{\gamma x} = \frac{1}{Z_0}\left(V^+ \exp^{-\gamma x} - V^- \exp^{\gamma x}\right) \end{aligned} \tag{4.17}$$

Where Z_0 is the characteristic impedance of the line defined as the ratio of the amplitude of a single voltage wave to its current wave, i.e. $V^{\pm}/I^{\pm}$. Note that for a loss-less transmission line $(R, G = 0)$, equation 4.18 becomes equation 4.1.

$$Z_0 = \sqrt{\frac{(R_l + jwL_l)}{(G_l + jwC_l)}} \tag{4.18}$$

We then define the input impedance as the impedance observed at a distance l from the load Z_L

$$Z_{in} = \frac{V(l)}{I(l)} = Z_0 \frac{1 + \Gamma \exp^{-2\gamma l}}{1 - \Gamma \exp^{-2\gamma l}} \tag{4.19}$$

Where γ is the propagation constant and Γ is the voltage reflection coefficient $\Gamma = Z_L - Z_0/Z_L + Z_0$ as in equation 4.8. This expression can be rewritten as

$$Z_{in} = Z_0 \frac{Z_L + Z_0 \tanh(\gamma l)}{Z_0 + Z_L \tanh(\gamma l)} \tag{4.20}$$

For a loss-less transmission line, $\gamma = j\beta$ and equation 4.20 becomes

$$Z_{in} = Z_0 \frac{Z_L + jZ_0 \tan(\beta l)}{Z_0 + jZ_L \tan(\beta l)} \tag{4.21}$$

Where $\beta = 2\pi/\lambda$ is the wavenumber. We observe that for an open or short circuited line, $Z_{in,oc} = -jZ_0 \cot(\beta l)$ and $Z_{in,sc} = jZ_0 \tan(\beta l)$. The Richards transformation was introduced by Richard [32] with the goal of synthesizing LC elements using short and open circuited transmission lines. The transformation maps the ω plane to the Ω plane with a period of $\omega l/v_p = 2\pi$

$$\Omega = \tan(\beta l) = \tan\left(\frac{\omega l}{v_p}\right) \tag{4.22}$$

Replacing ω with Ω, the reactance of an inductor becomes

$$jX_L = j\Omega L = jL \tan(\beta l) \tag{4.23}$$

and the susceptance of a capacitor becomes

$$jX_C = j\Omega C = jC \tan(\beta l) \tag{4.24}$$

According to equation 4.21, equations 4.23 and 4.24 show that an inductor can be replaced by a short circuited segment of transmission line (stub) of length βl and characteristic impedance L, while a capacitor can be replaced by an open circuited stub of length βl and characteristic impedance $1/C$. As already mentioned, filter prototypes are normalized. This means that the cutoff frequency $\omega_c = 1$. To obtain the same cutoff frequency in the Ω plane, i.e. $\Omega = 1 = \tan(\beta l)$, the stub length must be $l = \lambda/8$ where λ is the wavelength of the line at ω_c. This also means the response of the filter will be periodic every $4\omega_c$ and will differ from the prototype for frequencies away from ω_c.

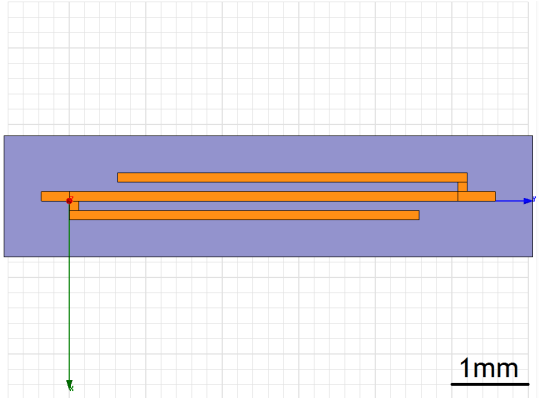

Figure 4.13.: Model schematic of a microstrip low pass filter.

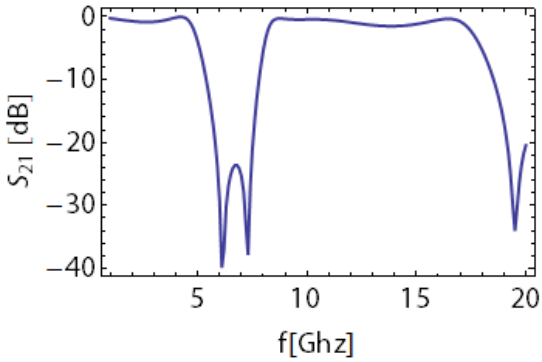

Figure 4.14.: Transmission response of the designed microstrip low pass filter shown in Fig. 4.13.

Kuroda's identities make filter implementation more practical by adding redundant transmission line sections of length $\lambda/8$. They allow to physically separate transmission line stubs, transform series stubs into parallel stubs or vice-versa, and to obtain realizable characteristic impedances. Please refer to chapter 8.5 of [24] for a longer treatment of microwave filter design.

Filters are usually designed based on polynomials such as *Butterworth* and *Chebyschev*. While the first is a good choice for maximally flat pass-band response, the latter provides a steeper cutoff but one obtains equal-ripple response in the pass-band. The use of the Richards transformation is usually good for so-called stepped impedance filter design, which consists of interleaved sections of high and low impedance. However, the dimensions of the calculated stubs are usually large. To circumvent the problem of stub dimensions, we follow the approach shown in Fig. 4.13 where we have connected two open circuited stubs with a $\lambda/4$ section of line. The design corresponds to a second order low-pass filter from a normalized Chebyschev prototype, however the characteristic impedance of the stubs is complicated to calculate given their L-shape. It is therefore easier to simulate their response starting from an initial estimate. We convert low pass prototype element values (chapter 8.5 in [24]) to normalized impedance values and estimate the length of a $\lambda/4$ section of microstrip Cu line ($\epsilon_r = 1$) to be around 5mm. With these initial estimates we tune the stub dimensions (width and length) in a simulation and extract the transmission response. For a filter length of 5 mm and width of 100 μm, we obtain a low-pass behaviour as shown in Fig. 4.14. The response shows the 3 dB ripple expected from the chosen Chebyschev normalized coefficients and is periodic in $4\omega_c$.

CHAPTER 5

Parallel FIR Filters

5.1. FPGA measurement setup

The full detection setup introduced in chapter 3 consist of a variety of devices including hardware and software components. For a conceptual treatment it can be simplified as shown in Fig. 5.1. The output signal is amplified, demodulated to an IF with an local oscillator by means of an IQ-mixer, analogue low pass filtered and subsequently digitized and digitally demodulated. The process of digitization means that conceptually we sample an input signal $x(t)$ every t_s seconds, where t_s is called the sampling period. We thus obtain the sequence $x_n = x(t_n)$ where $t_n = nt_s$ with n an integer number. Operations on this data sequence can then be performed.

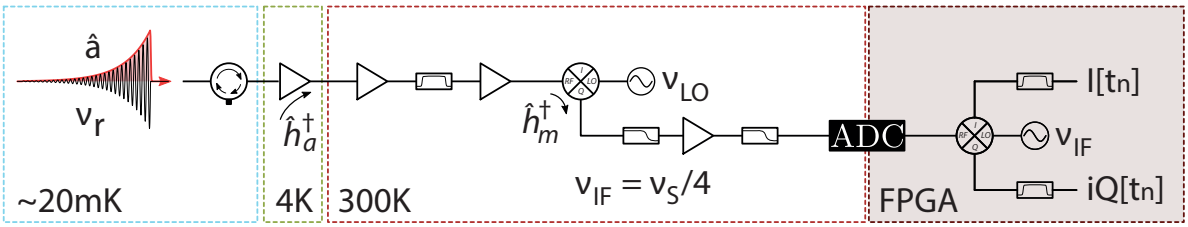

Figure 5.1.: Simplified measurement setup consisting of amplification, demodulation and low-pass filtering. Figure adapted from [33].

The input to the detection chain is given by the electric field $E(t)$ at the first amplifier input. Since the electric field can only take real values, its spectrum is hermitian symmetric [34] meaning $E(\omega) = E^*(-\omega)$. A powerful tool used to analyse our signals is the measurement of correlations. However, before talking about correlation measurements, lets agree on some definitions of how to talk about correlations.

What we measure is ultimately a quantum signal, which in turn is modelled by probabilities. We can thus think of a single measurement as a single sample function $x(t)$ of a random process $X(t)$. The correlation between any two complex random processes X and Y is defined as (equation 5.1)

$$R_{XY}(t_1, t_2) = E[X^*(t_1) Y(t_2)] \tag{5.1}$$

Where $E[\cdot]$ denotes the statistical average, i.e. the expected value. The correlation of process X with itself is called the autocorrelation. Roughly speaking, if a random process is *wide-sense stationary*, the (auto)correlation does not depend on absolute time, but only on time differences $\tau = t_2 - t_1$.

$$R_{XX}(t, t+\tau) = E[X^*(t) X(t+\tau)] = R_{XX}(\tau) \tag{5.2}$$

In real experiments, we can never measure the true correlation functions of a random process because we never have all of its sample functions at our disposal. Furthermore, we usually have available only part of one sample function of the random process. On the other side, detectors generally perform an integration over time either implicitly or explicitly. The only recourse left is then to determine time averages based on finite time portions of single sample functions. The time average A of any quantity is defined as

$$A[\cdot] = \lim_{T\to\infty} \frac{1}{2T} \int_{-T}^{T} [\cdot]\, dt \tag{5.3}$$

Denoting $x(t)$ as one sample function of a random process $X(t)$, time averages of interest are the mean value $\bar{x} = A[x(t)]$ and the time autocorrelation function $\Re_{xx}(\tau) = A[x(t)\, x(t+\tau)]$. According to equation 5.3, these quantities simply produce a number (for a fixed value of τ). Nevertheless, when all sample functions of $X(t)$ are considered, $\bar{x}$ and $\Re_{xx}(\tau)$ become random variables. By taking their expectation value we obtain

$$\begin{aligned} E[\bar{x}] &= \bar{X} \\ E[\Re_{xx}(\tau)] &= R_{XX}(\tau) \end{aligned} \tag{5.4}$$

Suppose that by some theorem $\bar{x}$ and $\Re_{xx}(\tau)$ could be made to have zero variances, then we could write equation 5.4 as

$$\begin{aligned} \bar{x} &= \bar{X} \\ \Re_{xx}(\tau) &= R_{XX}(\tau) \end{aligned} \tag{5.5}$$

In other words, equation 5.5 tells us that the time averages $\bar{x}$ and $\Re_{xx}(\tau)$ equal the statistical averages $\bar{X}$ and $R_{XX}(\tau)$ respectively. The *ergodic theorem* allows the validity of equations 5.5. More generally it allows all time averages to equal the corresponding statistical averages. Ergodicity is a very restrictive form of stationarity and it is often difficult to prove. Nevertheless, in practice we are basically forced to work with only one sample function of a random process and derive time mean value, time correlation functions, etc. By assuming ergodicity, we can infer the statistical characteristics of the process. If the above mentioned concepts result somewhat confusing, I strongly suggest you to refer to chapters 7 and 8 of [35].

In this way, all measurements we perform in the lab basically assume ergodicity. We can for instance measure the power spectral density (PSD) $S_{XX}(\omega)$ of a random process X using the so-called *Wiener-Khinchin relations* which state that $S_{XX}(\omega)$ and $R_{XX}(\tau)$ form a fourier transform pair [35].

$$\begin{aligned} S_{XX}(\omega) &= \int_{-\infty}^{\infty} R_{XX}(\tau)\, e^{-i\omega\tau} d\tau \\ R_{XX}(\tau) &= \frac{1}{2\pi} \int_{-\infty}^{\infty} S_{XX}(\omega)\, e^{i\omega\tau} d\omega \\ S_{XX}(\omega) &\leftrightarrow R_{XX}(\tau) \end{aligned} \tag{5.6}$$

In practice we measure correlations in the frequency domain by fourier transforming the digitized signals. For further details about the actual implementation of such a measurement in hardware, I strongly suggest to refer to [14] where the implementation of a FPGA-based correlator application using FFTs is described.

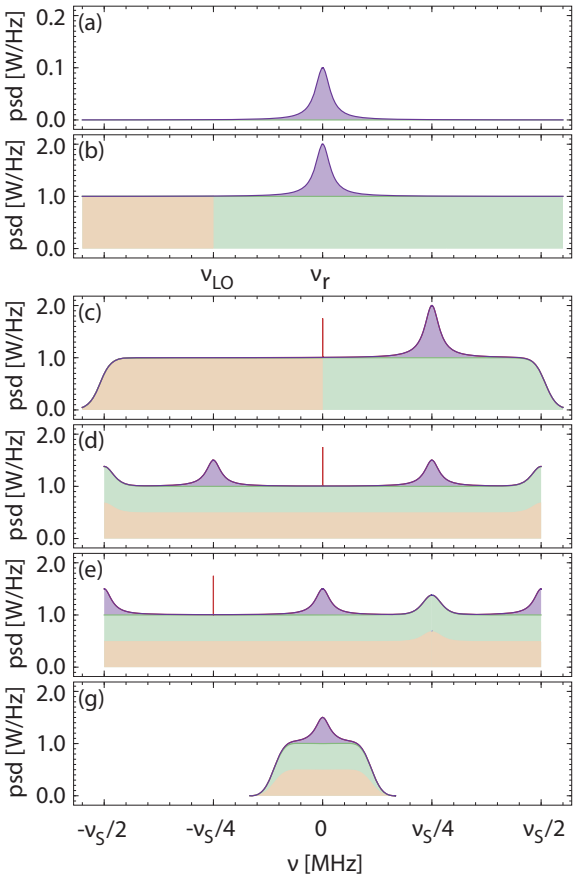

Figure 5.2.: Power spectral density (psd) of a signal (purple), noise (green and orange according to their frequency origin) and DC-offset (red) after various states of the signal processing: (a) signal of interest, (b) added noise during amplification, (c) analog down conversion to intermediate frequency, (d) digitizing single down converted quadrature, (e) digital down conversion, (g) FIR filter. Image adapted from [33].

Fig. 5.2 shows a schematic of our signal processing setup in the frequency domain 5.1. We start with an in principle band-limited signal at a frequency ν_r (usually the resonance frequency of the resonator). ν_{LO} denotes the frequency of a local oscillator. Upon amplification (Fig. 5.2b) noise is added and we denote it as green or orange according to their frequency origin (to the right or to the left of ν_{LO}, which after the next step become positive and negative frequency components). The signal is then IQ-mixed and thereby demodulated to an intermediate frequency (Fig. 5.2c), usually set to be one quarter of the sampling frequency $\nu_s = 1/t_s$. The reason for this is that in hardware, digital demodulation is made by multiplying the input sequence with a sequence $e^{-i2\pi\nu_{IF}t_s n}$ where n is an integer number. For $\nu_{IF} = \nu_s/4$, this sequence collapses to $1, -i, -1, i, 1, \ldots$. The multiplication of that sequence with the digitized signal x_n can be performed on the FPGA using only a two-bit counter, a sign flip, and signal routing. During IQ-mixing only the I-component is taken in order to avoid having to deal with imperfections of IQ-mixers such as different DC offsets, phase between I and Q outputs not being exactly $\pi/2$, amplitude differences, etc. The signal is then digitized. Since

we only take I-component (it is real and symmetric), the positive and negative frequency components can not be distinguished. This means that half of the negative frequency components will appear on the positive side and vice-versa. The bumps at the edge of the frequency axis in Fig. 5.2d are aliases of non-filtered components beyond the nyquist frequency $f_s/2$. Finally digital down conversion and eventually digital filtering is applied (Fig. 5.2e).

We use digital filters to filter out: mirror frequency components, DC-offsets, additional noise outside the desired detection band, and to obtain maximum signal to noise ratio (SNR) by means of so-called matched filters. Furthermore, the measurement of time resolved correlation functions might even require the use of digital filters. Currently we have two hardware platforms at our disposal for signal processing purposes. One is a Virtex-4 FPGA supporting 100MHz bandwidth and another is a Virtex-6 FPGA featuring 1GHz bandwith. While applications for measuring different observables with the Virtex-4 have been well developed in our lab during the past years, development on the Virtex-6 FPGA is still an ongoing task. However, programming the Virtex-6 FPGA is not trivial. The main reason is that in order to support the 1GHz bandwidth, we need to deal with (usually) 8 parallel samples due to the clocking characteristics of the internal Virtex-6 and the analog to digital (ADC) converter. This parallelism introduces a large programming complexity. Please refer to [36] for further details regarding development efforts on the Virtex-6 FPGA. An important desired feature for the Virtex-6 platform is the support of arbitrary finite impulse response (FIR) filters. During the course of the project I engaged in the development of this feature. The rest of this chapter summarizes the strategies I took to enable the use of parallel FIR filters in the Virtex-6 platform.

Debugging PSD measurements During the course of the project we eventually observed additional signal features appearing in our measured PSDs which differed from the behaviour expected in Fig. 5.2. It may then be worth mentioning a couple points in regard to our measurement setup, in case you observe unexpected signals in a PSD measurement.

1. By sweeping the local oscillator frequency (ν_{LO}), the intermediate frequency $\nu_{IF} = \nu_r - \nu_{LO}$ is effectively changed. If the unexpected signals you observe move as you sweep ν_{LO}, they come from somewhere before the IQ-mixing. If they do not move, they must come from somewhere after the IQ-mixing.

2. The direction in which the unexpected signals move in the PSD with relation to the direction in which ν_{LO} is swept, allows to tell their real frequency. If they move in opposite directions, you can directly read their frequency from the PSD, remembering that everything is centered around ν_r with a bandwidth ν_s. If they move in the same direction, their real frequency lies somewhere on the opposite side of the spectrum (i.e. If they appear on the positive(negative) side, in reality they are somewhere on the negative(positive) side). Their real detuning from ν_r would be obtained by adding ν_{IF} to the observed value and multiplying by -1.

5.2. Polyphase decomposition

To get a feeling of a parallel filter, it is useful to look at its response in the Z transform domain. A general FIR filtering operation is a linear, time invariant network whose output is given by the weighted sum of the most recent input values (equation 5.7). h_k is the value of the filter's impulse response at the $k-th$ instant, N is the filter length (also called number of taps) and $0 \leq k < N$.

$$y_n = \sum_{k=0}^{N-1} h_k x_{n-k} \tag{5.7}$$

Equation 5.7 is also a convolution between the filter and the input signal. In terms of its Z transform, a filter can be expressed as

$$H(z) = \sum_n h[n] z^{-n} \tag{5.8}$$

Where $h[n]$ are the filter coefficients. Equation 5.8 can be decomposed into its even and odd components.

$$H(z) = \sum h[2n] z^{-2n} + z^{-1} \sum h[2n+1] z^{-2n} = H_0 + z^{-1} H_1 \tag{5.9}$$

Equation 5.9 decomposes a general filter H into two filters H_0 and H_1 each one of length $N/2$. This process is called poly-phase decomposition, and can in general be applied for M components

$$\begin{aligned} H(z) &= \sum h[nM] z^{-nM} + z^{-1} \sum h[nM+1] z^{-nM} + \ldots + z^{-(M-1)} \sum h[nM+M-1] z^{-nM} \\ &= \sum_{m=0}^{M-1} z^{-m} H_m^M \end{aligned} \tag{5.10}$$

Remembering that in the Z domain, the filtering operation expressed in equation 5.7 is a multiplication $Y = XH$, using the poly-phase representation we can then express a parallel FIR filtering operation in terms of L poly-phase components, where L is the filter's block length, i.e. the number of parallel samples.

$$\sum_{i=0}^{L-1} Y_i^L z^{-i} = \left(\sum_{j=0}^{L-1} X_j^L z^{-j} \right) \left(\sum_{k=0}^{L-1} H_k^L z^{-k} \right) \tag{5.11}$$

To get a feeling of this, lets apply a poly-phase decomposition to a 2-parallel FIR filtering operation

$$\begin{aligned} Y = Y_0 + z^{-1} Y_1 &= \left(X_0 + z^{-1} X_1 \right) \left(H_0 + z^{-1} H_1 \right) \\ &= X_0 H_0 + z^{-1} \left(X_1 H_0 + X_0 H_1 \right) + z^{-2} X_1 H_1 \end{aligned} \tag{5.12}$$

Hence, the even and odd output sequences are given by

$$\begin{aligned} Y_0 &= X_0 H_0 + z^{-2} X_1 H_1 \\ Y_1 &= X_1 H_0 + X_0 H_1 \end{aligned} \tag{5.13}$$

Equation 5.13 can be schematically represented by Fig. 5.3. For a filter of length N, we observe that each term in equation 5.13 has $N/2$ multiplications, i.e. a 2-parallel filter requires $2N$ multiplications. In general, a L-parallel FIR filter requires LN multiplications of length N/L and $L(N-1)$ additions.

Our signal processing platform is based on a *Xilinx Virtex6* FPGA and a *DSPextreme* analogue to digital converter. We are interested in implementing filters of length $N = 40$ which process 8 parallel samples every clock cycle. A straight forward implementation of an 8-parallel 40-tap filter would hence require $LN = 320$ multiplications. In the *Xilinx Virtex6* hardware, multiplications are implemented by means of so-called *DSP48E1* slices. As explained in [36] and [37], for our digital signal processing application we are interested in filtering the in-phase and quadrature components for two channels. To fit this requirements, a total of 1280 multipliers would be required. However,

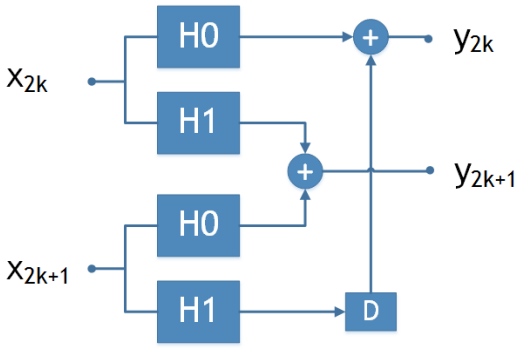

Figure 5.3.: 2-parallel filtering operation.

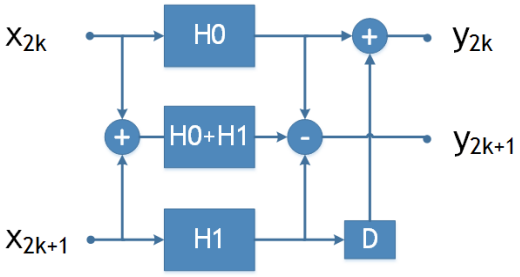

Figure 5.4.: 2by2 FFA.

the number of available *DSP48E1* slices in our FPGA is 768. Since the current implementation of a correlator by means of a parallel FFT [36] already uses nearly 90% of these hardware resources, a straight forward implementation of even a single 8-parallel 40-tap FIR filter exceeds the device capabilities.

The so-called *moving average* or *boxcar* filters are a type of FIR filters of particular interest because all their coefficients are equal. From equation 5.7 we observe that when all weights h_k are the same, the output y_n becomes simply a scaled sum. Boxcar filters are thus relatively simple and cost-effective to implement in hardware, and during a semester project a variable-length version for our Virtex-6 platform was implemented [37]. However, these filters present a couple drawbacks, namely: their frequency response is not flexible, and they are not well suited for measuring time resolved intensity correlations since the result is strongly affected by the square-window nature of their time response [37].

5.3. Parallel fast FIR algorithm

To overcome our hardware limitations, we start by trying to simplify the filtering structures by means of the so-called fast parallel FIR algorithm (FFA) [38]. If B is the number of bits of our input samples, the number of bits at the output of a multiplication gets doubled while for an addition it increases only by one. Therefore, the hardware cost of a multiplication is much larger than that of an addition. The general idea is to try to reduce the number of multiplications while paying an increase in the number of additions.

We start by noting that equation 5.12 can be written in a different form:

$$\begin{aligned} Y &= Y_0 + z^{-1}Y_1 = \left(X_0 + z^{-1}X_1\right)\left(H_0 + z^{-1}H_1\right) \\ &= X_0H_0 + z^{-1}\left((X_0 + X_1)(H_0 + H_1) - X_0H_0 - X_1H_1\right) + z^{-2}X_1H_1 \\ Y_0 &= X_0H_0 + z^{-2}X_1H_1 \\ Y_1 &= \left((X_0 + X_1)(H_0 + H_1) - X_0H_0 - X_1H_1\right) \end{aligned} \tag{5.14}$$

Fig. 5.4 is a schematic representation of equation 5.14. The block marked with a D stands for a delay of 1 clock cycle. Do not get confused by the delay z^{-2} in equation 5.14, it is implemented as a delay of 1 clock cycle since it delays the odd phases (x_{2k+1}). As an example, consider a 4-tap FIR filter $H = h_0 + z^{-1}h_1 + z^{-2}h_2 + z^{-3}h_3$. The 2by2 FFA decomposes the original filter 4-tap filter into three 2-tap filters: $H_0 = h_0 + z^{-1}h_2$, $H_1 = h_1 + z^{-1}h_3$ and $H_0 + H_1 = (h_0 + h_1) + z^{-1}(h_2 + h_3)$.

Although looking at equation 5.14 it may seem that now more multiplications are required, we note that the additional terms in Y_1 only need to be computed once. As shown in Fig. 5.4 this structure requires $3\,(N/2)$ multipliers and $3\,(N/2-1)$ additions which in comparison to the traditional 2-parallel filter structure (see Fig. 5.3) represent almost 25% of hardware savings, i.e. number of multiplications. Using this approach, a parallel filter can be implemented using approximately $2L-1$ filtering operations of length N/L.

In principle, structures of larger block length L can be also simplified. However, the algebraic complexity gets exponentially large [38]. One approach to reduce the design complexity is to cascade the FFA algorithm. In this way, for instance, a 4-parallel FFA can be obtained by cascading two 2-parallel FFAs [39]. In general, the number of multipliers for such a design strategy can be estimated as (equation5.15) [39], where r is the number of FFAs used , L_i is the block size of the FFA at step i and M_i is the number of filters that result from the application of the $i-th$ FFA.

$$M = \frac{N}{\prod_{i=1}^{r} L_i} \prod_{i=1}^{r} M_i \tag{5.15}$$

As described in appendix A we have synthesized an 8-parallel fast FIR filter by cascading three 2by2 FFAs. Since each application of a 2by2 FFA results in three filtering operations, we end up with 27 individual filters of length $N/8$. Fig. 5.5 shows a schematic diagram of our 8by8 fast parallel FIR filter design. We denote all operations before (after) the individual filters as pre(post)-processing. Enclosed in dashed rectangles are the post-processing blocks for each 2by2 (red), 4by4 (orange), and 8by8 (green) filters. Observe how the 8-parallel filter consists of three 4-parallel filters, each 4-parallel filter consists of three 2-parallel filters, and each 2-parallel filter consists of three individual filters. Please note that all individual filtering operations are denoted as $H0$, $H0+H1$ and $H1$. This is only to indicate the nature of each 2 parallel filter, since the actual coefficients are given by the inputs. For instance, the three filtering operations for the 2by2 filter with inputs $x_{8k}+x_{8k+2}$, $x_{8k}+x_{8k+2}+x_{8k+4}+x_{8k+6}$ and $x_{8k+2}+x_{8k+6}$ are H_0+H_2, $H_0+H_2+H_4+H_6$ and H_2+H_6. Please also remember that the blocks marked with a D stand for a delay of 1 clock cycle.

Fig. 5.6 shows a diagram of our 8by8 fast parallel FIR filter design implementation. Additionally to the pre- and post-processing blocks, we have added a controlling block to each parallel structure. This allows us to configure, i.e. write, the correct coefficients of each individual filter.

In comparison to $8N$ multipliers required in a traditional parallel FIR implementation, our design introduces hardware savings of around 58%. It is worth noting that a trade-off between the number of multipliers and adders must be kept. An exaggerated increase in the number of adders can at some point introduce design drawbacks, such as latency [38]. However, even with these hardware savings, together with the parallel FFT the design still exceeds the available resources.

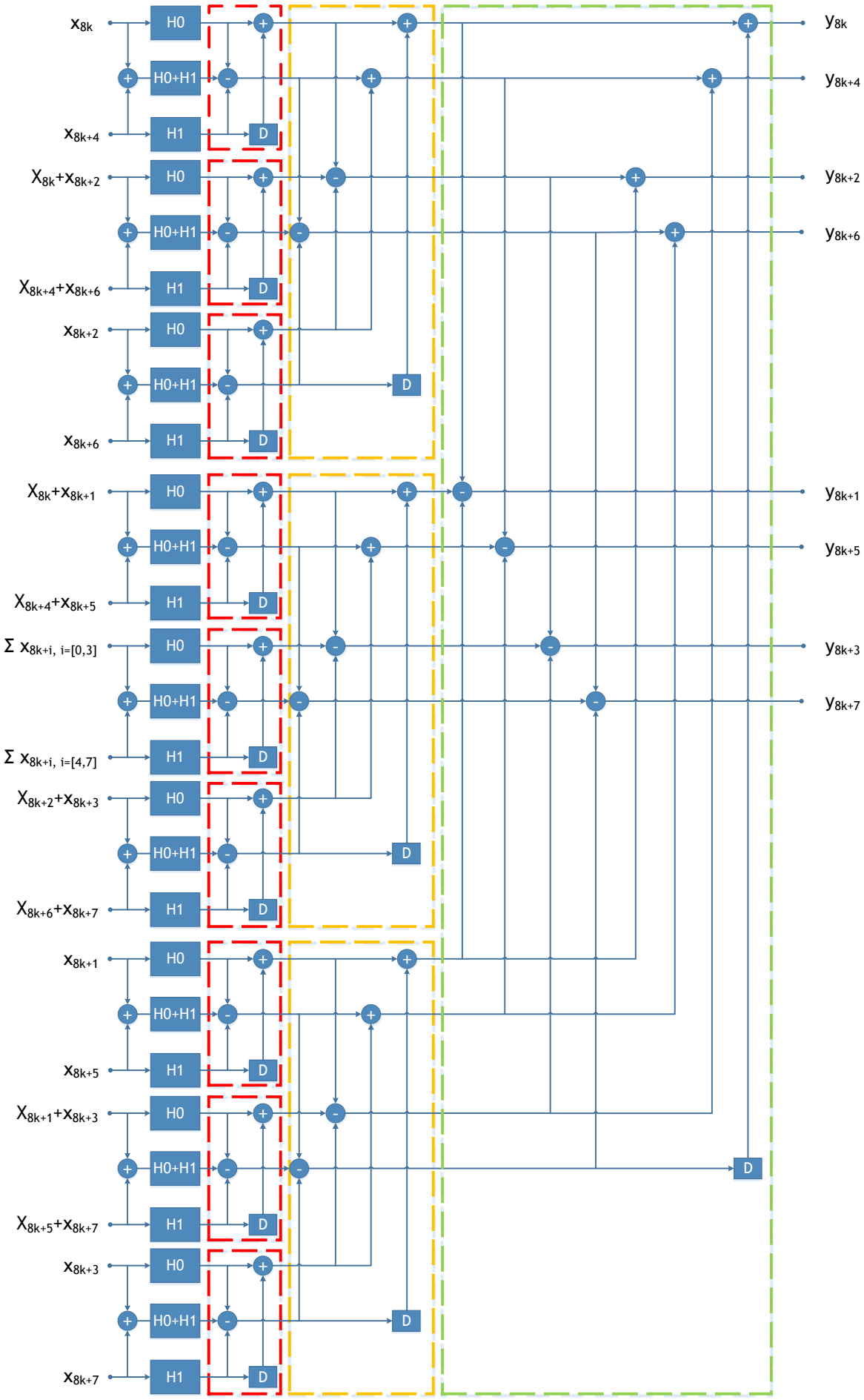

Figure 5.5.: 8-parallel filtering structure.

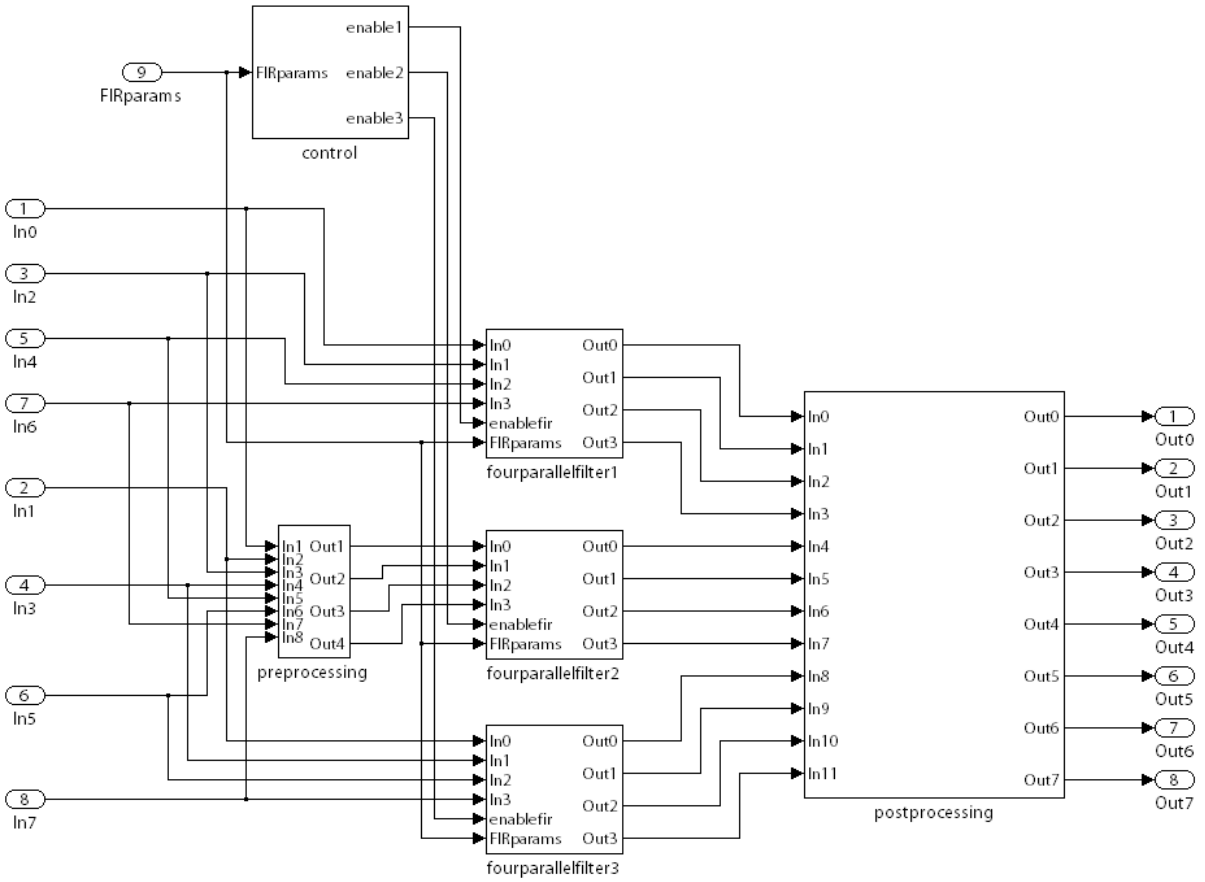

Figure 5.6.: Schematic diagram of our 8-parallel filtering structure. Additionally to pre- and post-processing blocks, a control block allows us to configure the 27 individual filters with their right coefficients.

5.4. Distributed arithmetic

The multiply intensive nature of equation 5.7 can be appreciated by observing that 1 output response requires the accumulation of N terms. Distributed Arithmetic (DA) intends to replace the task of summing product terms by table look-up procedures that are easily implemented in hardware logic blocks.

The number format used in our signal processing application is two's complement - a standard practice for fixed-point microprocessors in order to bound number growth multiplication. The input signal x_k in equation 5.7 may be written in this format as following:

$$x_k = -x_{k0} + \sum_{b=1}^{B-1} x_{kb} 2^{-b} \tag{5.16}$$

Where x_{kb} is a binary variable and can only assume values of 0 and 1. A sign value of -1 is indicated by x_{k0}. Plugging equation 5.16 into equation 5.7, we obtain:

$$y_n = \sum_{k=0}^{N-1} h_k \left(-x_{k0} + \sum_{b=1}^{B-1} x_{kb} 2^{-b} \right) = -\sum_{k=0}^{N-1} x_{k0} \cdot h_k + \sum_{k=0}^{N-1} \sum_{b=1}^{B-1} h_k \cdot x_{kb} 2^{-b} \tag{5.17}$$

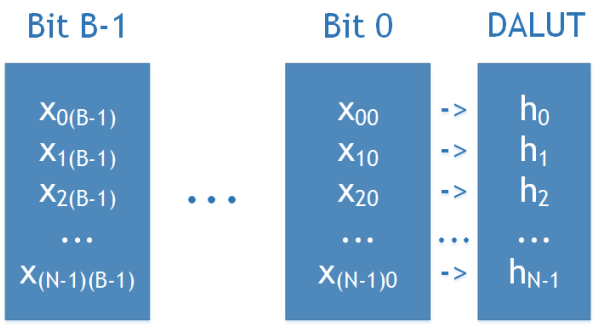

Figure 5.7.: Dalut addressing. In one clock cycle, the contents are addressed by taking bit b of all input samples. The filtering operation thus requires B clock cycles.

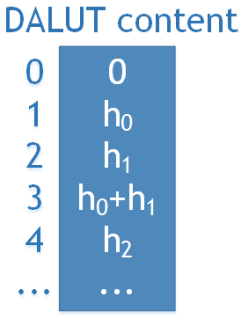

Figure 5.8.: Dalut contents for each address number as they are pre-stored in memory.

Equation 5.17 can in turn be expressed in matrix form

$$y_n = \left(\begin{pmatrix} x_{00} & \cdots & x_{0(B-1)} \\ \vdots & \ddots & \vdots \\ x_{(N-1)0} & \cdots & x_{(N-1)(B-1)} \end{pmatrix}^{\mathsf{T}} \begin{pmatrix} h_0 \\ \vdots \\ h_{N-1} \end{pmatrix} \right) \begin{pmatrix} -1 \\ \vdots \\ 2^{-(B-1)} \end{pmatrix} \tag{5.18}$$

$$y_n = (X^T H)C \tag{5.19}$$

Where X is the filter's input samples as matrix, and H the vector of coefficients of the filter. Since elements in matrix X can only take binary values, i.e. 0 or 1, we observe that all possible values that equation 5.19 takes, can be pre-stored in memory. In practice, one can construct a so-called distributed arithmetic look-up table (Dalut) that can be addressed by the same scaled bit of all input samples and can access all possible values for the product $X^T H$. Fig. 5.7 shows schematically how the look up table is addressed and Fig. 5.8 shows what the contents for each address are.

In this way, we have replaced all multiplications by storing pre-computed values in memory. This means that each of our 27 individual filters designed in appendix A is implemented using DA. The drawback of this approach is that the number of clock cycles required to produce 1 output sample is equal to the number of bits B of the input samples. This can be overcome by creating B look-up tables, so that all bits are processed in parallel. In practice, we have implemented DA by means of the FIR compilers readily available from *Xilinx*. There is a very important point to be mentioned: looking at Fig. 5.5 we note that the inputs to the individual filters are in general sums of the 8-parallel input samples. This means that their bit lengths are different, and hence the latency of all DA implementations is not the same. In other words, some of the 27 individual filters will take B clock cycles to produce one output sample, while others will take $B+i$ clock samples, where i is an integer. The latency of all individual filters must be the same, otherwise the parallel structure will produce wrong results. We hence added configurable delays at the output of each individual filter, such that the overall latency before any post-processing was the same.

5.5. Simulations and measurements

To check the validity of our designs and implementations, we first simulated the output of our 8-parallel filter in *Simulink* by using quasi white noise source blocks. We computed the filter response by storing its input and output sequence, and comparing the spectrum of the theoretical filtered

input with the spectrum if the simulated output. Furthermore, we implemented our design in the Virtex-6 platform and tested the response by recording PSD measurements of filtered and unfiltered artificial white noise (Tektronix AWG-520). We then estimate the filter response by dividing the filtered noise spectrum with the unfiltered noise spectrum. For testing purposes we picked up a symmetric and asymmetric filter. Fig. 5.9 shows the simulated and measured responses for a 10-tap boxcar filter (symmetric) and Fig. 5.10 for a 40-tap asymmetric filter. The filter coefficients were taken from the existent filter set designed for the Virtex-4 platform. In this way we have also verified the flexibility of our approach.

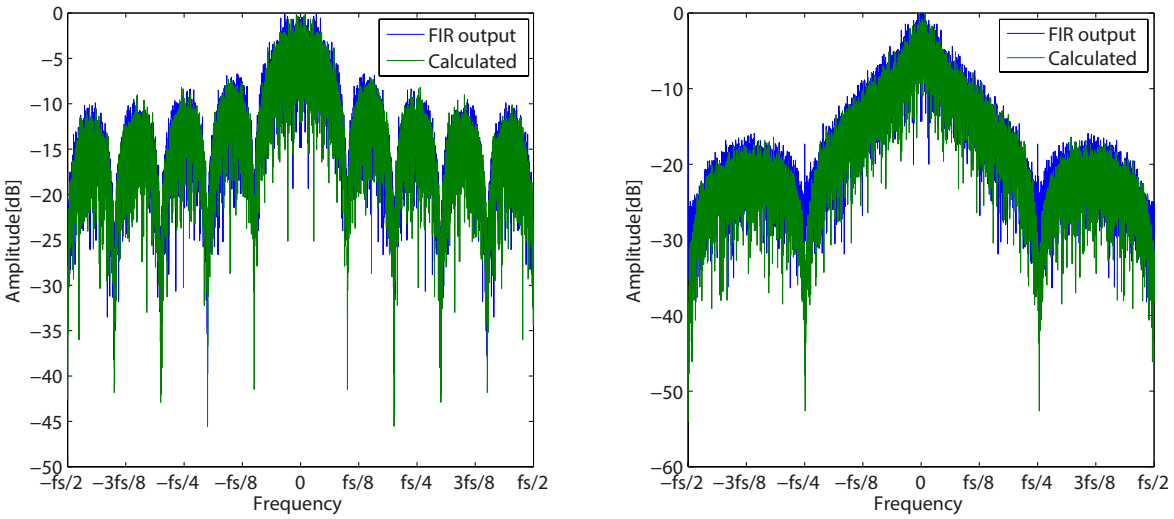

Figure 5.9.: (a) Simulated output of a 10-tap boxcar filter (blue) and calculated (green). (b) Chebyschev+Lorentzian+4-tap boxcar filter.

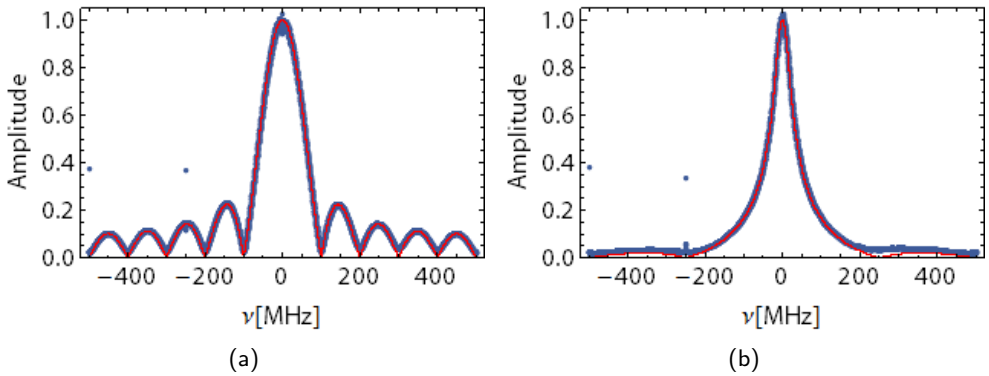

Figure 5.10.: (a) Measured (blue) and theoretical (red) filter response output of a 10-tap boxcar filter, and (b) an asymmetric Chebyschev+Lorentzian+4-tap boxcar filter.

CHAPTER 6

DC Experiments with a Double Quantum Dot

In this chapter we will start by covering a few relevant basics in regard with DC experiments with quantum dots. Please refer to review articles ([40], [41]) and books ([42], [9]) for a wider coverage of the theoretical aspects of electronic transport in quantum dots.

6.1. Transport in the linear regime

Single quantum dots A simple way to model a quantum dot is to think of it as a metallic island [9] tunnel-coupled to source (S) and drain (D) contacts/leads, see Fig. 6.1. The tunnel barriers are modelled as a combination of tunable resistive and capacitive components. Additionally, the electrostatic potential on the dot can be tuned with help of a gate voltage (V_{PG}).

The first measurement one may think of is to apply a small source-drain voltage (V_{SD}) and measure the current flowing through the sample as a function of V_{PG}. As shown in Fig. 6.1(b), a set of peaks in the current is observed. These peaks are called conductance resonances and their spacing is caused by the so-called Coulomb blockade effect, which appears as a manifestation of the repulsive interaction of electrons in the dot. Fitting a Lorentzian function to one of the resonances allows to estimate the electronic temperature of the reservoirs [9]. Two requirements have to be fulfilled in order to observe such behaviour. Thinking of the dot again as a metallic island with a self-capacitance C_Σ, the energy required to increase the number of electrons in the dot by one is $E_C = e^2/C_\Sigma$, also called charging energy [9]. The first condition which arises is that the charging energy needs to be larger than the thermal energy of the electrons, otherwise electrons could enter the dot via thermal excitation.

$$E_C = e^2/C_\Sigma >> k_B T_e \tag{6.1}$$

Modelling C_Σ as the capacitance of a thin metallic plate with a radius around 80 nm, at cryogenic temperatures (T=10 mK to 100 mK) equation 6.1 holds. The tunneling resistance needs to be larger than the resistance quantum in order to resolve individual electrons tunneling through it $R_T >> h/e^2$. If instead of measuring the current at a fixed V_{SD} we now measure it for several values of V_{SD} as a function of V_{PG}, so-called Coulomb diamonds appear as shown in Fig. 6.1(c). Figures 6.1(d-g) sketch the energy levels of the dot (μ_N) with respect to the leads for different positions in the Coulomb diamond diagram (Fig. 6.1(c)). Please note that we do not consider the

temperature broadening of the Fermi distribution. Applying a bias V_{SD} creates a difference in the fermi energies of the leads (μ_S, μ_S). V_{PG} acts on the energy levels of the dot by moving them up and down. Typically we observe three cases: an energy level in the dot μ_N aligned with the fermi energy of both leads μ_S, μ_S (Fig. 6.1(d)), μ not aligned with any of the leads (Fig. 6.1(e)), and μ_N aligned only with one of the leads (Fig. 6.1 (f) and (g)).

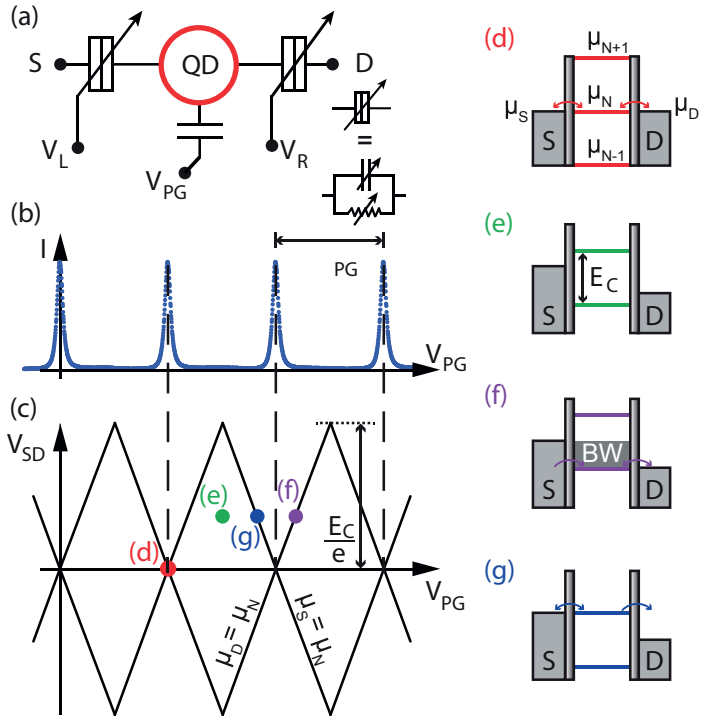

Figure 6.1.: (a) Electric circuit representation of a single quantum dot as a metallic island connected to reservoirs. (b) Schematic of Coulomb resonances as a function of plunger gate voltage (V_{PG}). (c) Schematic of Coulomb diamonds typical for a charge stability diagram of a single quantum dot. (d-g) Schematic of different energy level configurations: (d) an energy level in the dot aligned with the fermi energy of both leads, (e) not aligned with any of the leads and (f-g) aligned only with one of the leads. Figure adapted from [43].

The extent of the diamonds in source-drain voltage is a direct measure of the E_C. The voltage difference between two Coulomb resonances (ΔV_{PG}) can be converted into an energy using the so-called lever-arm of a plunger gate α_{PG}. You may think of the lever-arm as a translation factor from applied gate voltage to a change in the static potential energy in the dot.

$$\alpha_{PG} = \frac{|V_{SD}|}{|\Delta V_{PG}|} \tag{6.2}$$

An additional energy scale not mentioned so far is the single particle level spacing γ. In order to resolve charge transport through excited states, the thermal energy of the electrons ($k_B T_e$) has to be smaller than the single particle level spacing. Whether the charging energy or the single particle level spacing is dominant depends on the size of the quantum dots. A crossover from charging energy to single-particle level spacing can be estimated to be at a radius of approximately 10 nm [9] for circular dots in GaAs. Single-particle levels are observed in transport measurements as additional steps in the current outside the Coulomb diamonds. For the experiments and sample characteristics in this project charging energy was the dominant energy scale.

Double quantum dots We now intend to intuitively describe some features of linear electron transport (i.e. $V_{SD} = 0$) when we couple two metallic islands together, i.e. we form a double quantum dot (DQD). We initially couple both dots with a resistive barrier (Fig. 6.4(a)). Each dot is again tunnel coupled to either the source (S) or drain (D) contact and its electrostatic potential can again be tuned with a corresponding plunger gate (V_{LPG}, V_{RPG}). The measurement now consists of sweeping V_{LPG} and V_{RPG} while recording the current I_{SD} through the DQD. We observe the charge stability diagram in Fig. 6.4(a). It consists of vertical and horizontal lines. Along the horizontal (vertical) lines a quantum dot energy level in the right (left) dot (RD (LD)) is resonant with its corresponding drain (source) lead. The crossing of the two lines highlighted by red circles indicate points where an energy level in LD is aligned with an energy level in RD and hence resonant electron transport, also referred as elastic tunneling, through the double quantum dot occurs. These points are called triple-points. Within each rectangle the number of charge carriers is fixed and is indicated by the number (M,N). We have so far ignored any cross-couplings in our model. In reality, all elements in the model are coupled to each other forming a matrix. The magnitude of the couplings depends on many parameters such as the sample geometry. Due to the cross-couplings all gates may effectively act as a plunger gate on each dot. As result, the horizontal and vertical lines in the charge stability diagram become tilted and our measurement looks like in Fig. 6.4(b). The slope in the charge stability diagram is a measure of the cross-coupling strength. In general, coupling between LD and RD is not only resistive but also capacitive. As a result a new energy scale, the interdot charging energy (ϵ) appears. If an electron is loaded into LD when the energy levels in LD and RD are resonant both with each other and the leads, ϵ has to be overcome in order to also load an electron into RD. The different effects lead to a splitting in the triple-points and thereby a charge stability diagram which consists of tilted hexagon structures as shown in Fig. 6.4(c). Finally, Fig. 6.4(d) shows a detailed view around a line connecting two triple points, a so-called interdot charge transfer line. Along this line, energy levels in LD and RD are resonant with each other but not with the leads. Only at the triple points energy levels in LD and RD are resonant with the fermi energies of the leads, and resonant transport occurs. Going from one end of the interdot charge transfer line to the other adds one electron to each dot. Similar to Fig. 6.4(a), along one set of parallel lines (blue and purple Fig. 6.4(d)) the left(right) dot is resonant with its neighbouring lead. Due to energy conservation, along these lines higher order tunneling processes referred to as cotunneling [9] can take place in order to observe electron transport.

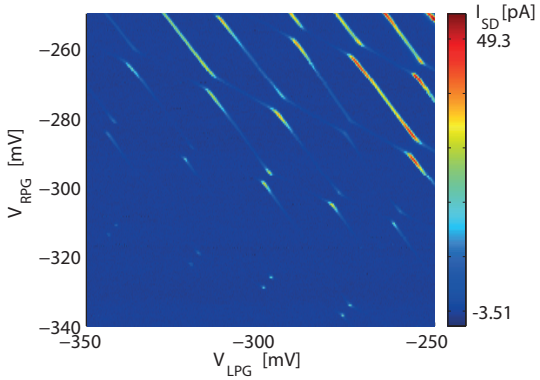

Figure 6.2.: Charge stability diagram in the few electron regime measuring DC current through the DQD.

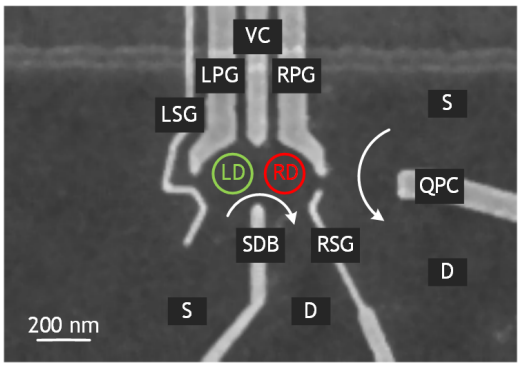

Figure 6.3.: SEM image of the sample gate design. White arrows indicate directions in which current flows.

In the case of a non-zero bias ($V_{SD} \neq 0$), also referred to as non-linear transport regime, a bias window is opened in which current can flow through the DQD. As result, the triple points expand into so-called finite bias triangles and current is measured within them. Please refer to [40] for a further presentation on the origin of these processes.

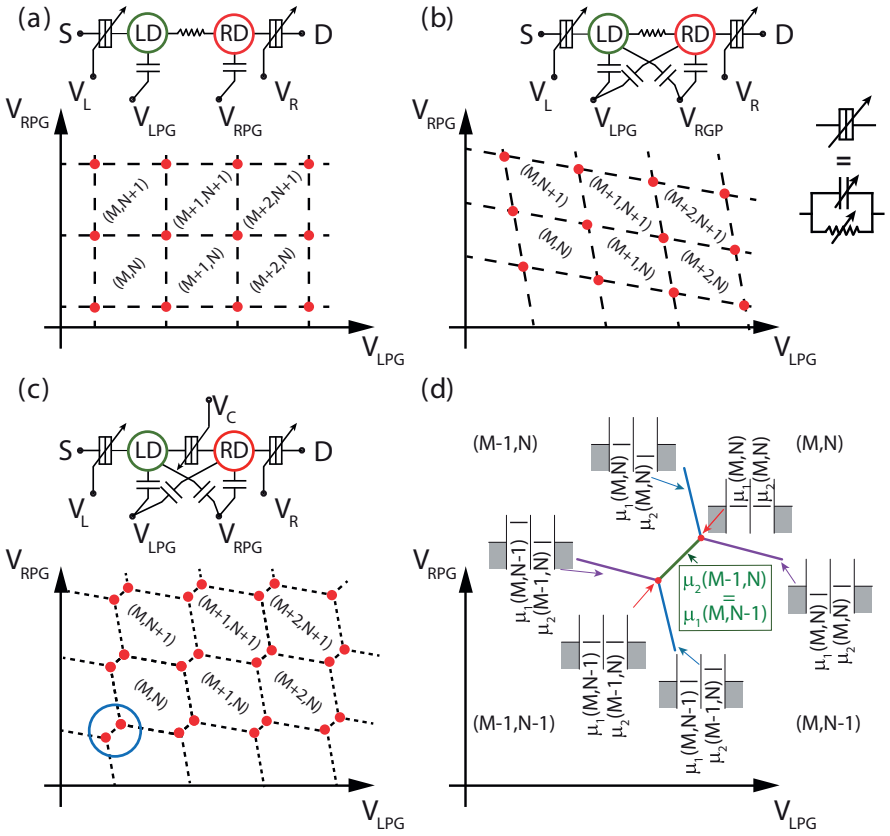

Figure 6.4.: (a-c) Different double quantum dot models with their corresponding charge stability diagrams as a function of plunger gate voltages V_{LPG} and V_{RPG}, as explained in the text. Red points label configurations where elastic electron transport takes place. (M,N) label stable charge configurations. (d) Close view of the charge stability diagram close to an interdot charge transfer line. Figure adapted from [43].

Fig. 6.2 shows a typical measurement of a charge stability diagram. Cotunneling lines and triple points are observable measuring DC current. Although our sample design includes a quantum point contact (QPC), see Fig. 6.3 which allows for charge detection measurements [44], for the measurements presented in this report we did not make use of it. The reason is that we only got a working sample at the very end of the project and charge detection did not work as expected with it. Some gates, namely LSG and QPC did also behave strangely. Nevertheless, we were able to form a double dot potential landscape and perform a variety of interesting experiments presented in this report.

6.2. Transport in the non-linear regime

The term non-linear transport regime refers to the case when a finite source drain bias is applied ($V_{SD} \neq 0$). A bias window opens in which electron transport is possible for different quantum state configurations [40]. As result, triple points extend to triangular shaped regions in the charge stability diagram and direct current is measured within them. Such a transport measurement can be used to estimate the lever arms of a plunger gate on left and right dot. An approximate of the lever arms $\alpha_{LL(RR)}$ of the left(right) plunger gate on the left(right) dot can be calculated to be

$$\alpha_{LL(RR)} = \frac{|eV_{SD}|}{\left|\delta V_{LPG(RPG)}\right|} \tag{6.3}$$

where δV_{PG} is related to the projected dimension of a finite bias triangle on the V_{LPG} axis of the charge stability diagram. Please refer to [40] for a complete calculation. Fig. 6.5a shows DC measurement of finite bias triangles. From this measurements we extracted a lever-arm $\alpha_{LL} \approx \alpha_{RR}$ =0.105 meV/mV following the method presented in [45]. Fig. 6.5b shows a closer view to the center triangle (enclosed in a white star) in Fig. 6.5a. White arrows indicate excited states which contributes to the measured conductance. The spacing between the states indicated with a cyan arrow, allows to estimate the confinement energy and thereby the dot size.

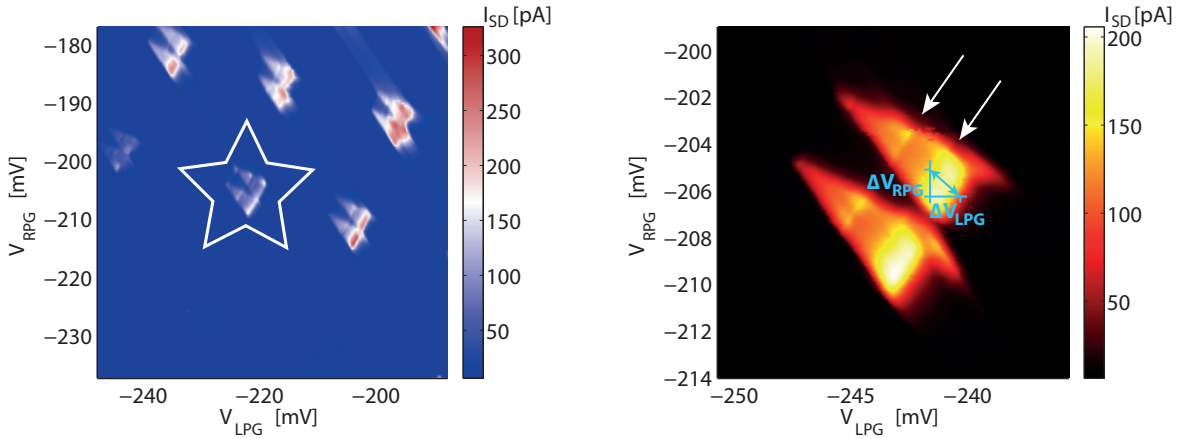

Figure 6.5.: (a) Finite bias triangles in a DC measurement. (b) Closer look to triangle in (a). White arrows indicate excited states. The cyan arrow indicates the spacing between the states, allowing to estimate the confinement energy and thereby the dot size.

Considering the QD as a 2D thin metallic disc, the confinement energy can be estimated from the 2D density of states. The k-space volume per k state is $(2\pi/L)^n$, where n is the number of dimensions. Therefore $(L/2\pi)^n$ is the number of states per k-space volume. The number density of states (number of states per real space volume) is thus given by:

$$n_v = \frac{N_v}{V_r} = \left(\frac{1}{2\pi}\right)^n V_k \tag{6.4}$$

Where $V_{r(k)}$ is the real(k-space) volume. V_k can be estimated from the dispersion relation

$$k\,(E) = \sqrt{\frac{2m^* E}{\hbar^2}} \tag{6.5}$$

where m^* is the effective mass. The density of states is defined as $\partial n_v/\partial E$. For 2D ($n = 2$), $V_k = \pi k^2$, hence by pluging equation 6.5 into equation 6.4 and differentiating by E we obtain the 2D density of states

$$D_{2D}(E) = \frac{\partial n_V}{\partial E} = \frac{\left(\frac{1}{2\pi}\right)^n \pi k^2(E)}{\partial E} = \frac{m^*}{\pi\hbar^2} \tag{6.6}$$

This shows that the 2D density of state is constant. Multiplying equation 6.6 by $V_r = \pi r^2$ gives an estimate of the number of states per energy interval. Hence the energy interval per state, i.e. confinement energy is given by equation 6.7

$$\begin{aligned} E_{conf} &= \frac{energy\ interval}{state} = \frac{V_r}{D_{2D}(E)} \\ E_{conf} &= \frac{\hbar^2}{m^* r^2} \end{aligned} \tag{6.7}$$

From Fig. 6.5b we can estimate the confinement energy $E_{conf} = 0.171$ meV and by using equation 6.7 get an estimate for the size of the dot $r \approx 57$ nm.

$$E_{conf} = \frac{\hbar^2}{m^* r^2} = \sqrt{(\alpha_{LL}\Delta V_{LPG})^2 + (\alpha_{RR}\Delta V_{RPG})^2} \tag{6.8}$$

CHAPTER 7

RF Experiments with a Double Quantum Dot

7.1. Microwave readout

In section 2.2 we introduced the concept of electron tunneling between both dots leading to a hybridization of their electronic states (Fig. 2.4b), thereby forming something analogue to an effective two level system. We can also think of tunneling of an electron between both dots as a process in which the electron density effectively changes, which in turn can be associated to a change in polarizability. When an electron tunnels into one dot, the electron density changes and thereby the potential landscape confining the dot. Hence, the shape of the ground state electronic wave function in the respective dot changes [9]. This leads to a change in polarization and therefore in the AC susceptibility χ which depends on the tunnel coupling t and is maximal for zero detuning δ [46]. We may then interpret measurements performed in chapter 6 as measurements of the low frequency polarizability of the DQD.

At high frequency we can associate susceptibility changes with a change in the effective impedance (admittance) of the DQD. In a first approximation, a resistive component accounting for tunneling and a capacitive component defined as the change in charge with respect to a change in gate voltage can be considered. The effective capacitance includes a geometric contribution and a so-called quantum capacitance C_Q which is a function of the curvature in the band structure. The effective admittance can be probed by coupling a resonant circuit to the system. The additional admittance from the DQD changes the effective resonator admittance and thereby its resonance frequency [47]. This microwave readout is valid in the dispersive regime discussed in section 2.1.

Fig. 7.1 shows a lumped element representation of the DQD coupled to a resonator. As described in chapter 3, the resonator (red box) is coupled capacitively to input and output lines. A DQD coupled to it (green box) induces a dispersive shift and also dissipation (e.g. losses due to inelastic tunneling) in the resonator. These effects can be observed by driving the resonator with a coherent microwave tone at its resonance frequency ν_r recording the transmitted amplitude and phase [48]. In a first approximation, changes in phase relate to dispersive effects (frequency shifts) while changes in amplitude relate to dissipative effects. Fig. 7.3 shows the transmitted amplitude and phase in V_{LPG}, V_{RPG} space of a microwave tone driven at ν_r for $V_{SD} = 0$. Fig. 7.2 shows an SEM image of the DQD region where the $\Gamma_{L(R)}$ are the tunneling rates to the left(right) lead and t is the interdot tunnel rate. What we observe in Fig. 7.3 is basically the relation between the tunneling rates in the

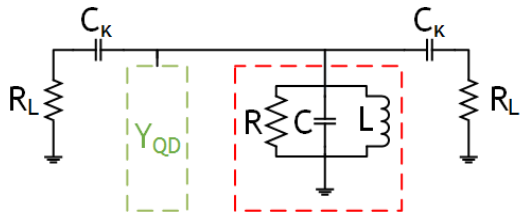

Figure 7.1.: Lumped element representation of the resonator-DQD system. The DQD is represented by a dynamic admittance $Y_{QD}(\omega)$.

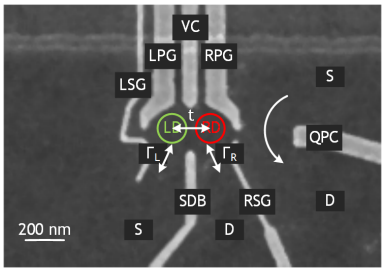

Figure 7.2.: SEM image of the sample gate design. $\Gamma_{L(R)}$ indicate the tunneling rate to the left(right) lead. t indicates the interdot tunneling rate.

DQD and the frequency of the microwave excitation in the resonator. When the tunneling rates are faster(slower) than the microwave excitation, the DQD response is capacitive(inductive) leading to negative(positive) frequency shifts [48].

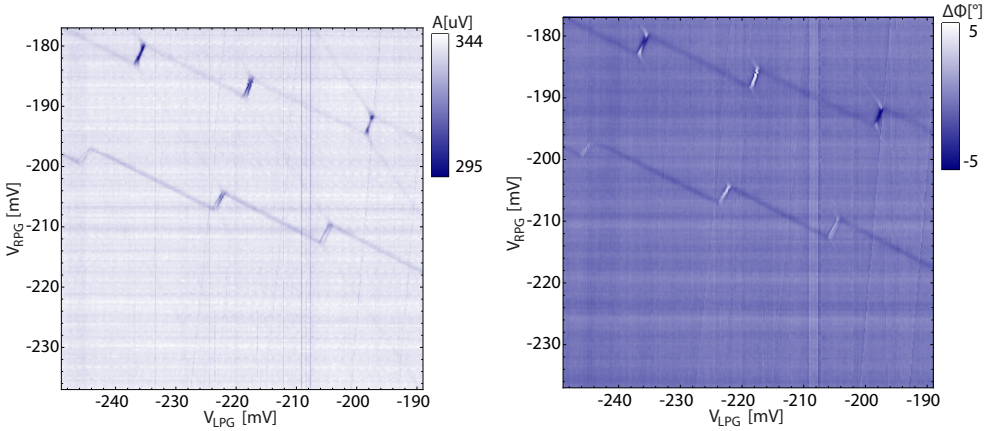

(a) (b)

Figure 7.3.: Charge stability diagrams measured at high frequency. (a) Transmitted amplitude of a microwave tone at the resonator eigenfrequency ν_r and (b) phase.

As mentioned in section 2.2, the interaction between the DQD qubit and the resonator exhibits a behaviour analogous to the cavity QED setup and which can be modelled by the Jaynes-Cummings hamiltonian (equation 2.1). Fig. 7.4 shows the two lowest eigenenergies of the coupled (resonator + DQD qubit) system (black solid lines) as a function of the interdot detuning δ for the case (a) when $2t < h\nu_r$ and (b,c) $2t > h\nu_r$. The energies are offset such that E=0 corresponds to the vacuum. As mentioned in section 2.1, when the DQD qubit and the resonator exhibit strong coherent coupling ($g > \kappa,\ \gamma$), the resonator eigenfrequency ν_r (green dashed line) and the bare transition frequency of the DQD qubit ν_q (red dotted line) exchange coherent interactions at a rate $g/2\pi$, and the coupled system shows anti-crossings at the points where $\nu_r = \nu_q$ (see black solid lines).

However, when the system is not strongly coupled, what remains at $\nu_r = \nu_q$ is a resonant interaction [49] that can be observed with a resolved spectral measurement as a function of δ [2]. Making a cut along a detuning axis (white arrow in Fig. 7.5a) would show phase shifts as a function of δ from which dispersive resonance shifts could be implied. However, such a measurement does not allow to unambiguously distinguish dispersive and dissipative effects [3]. In order to do so, a

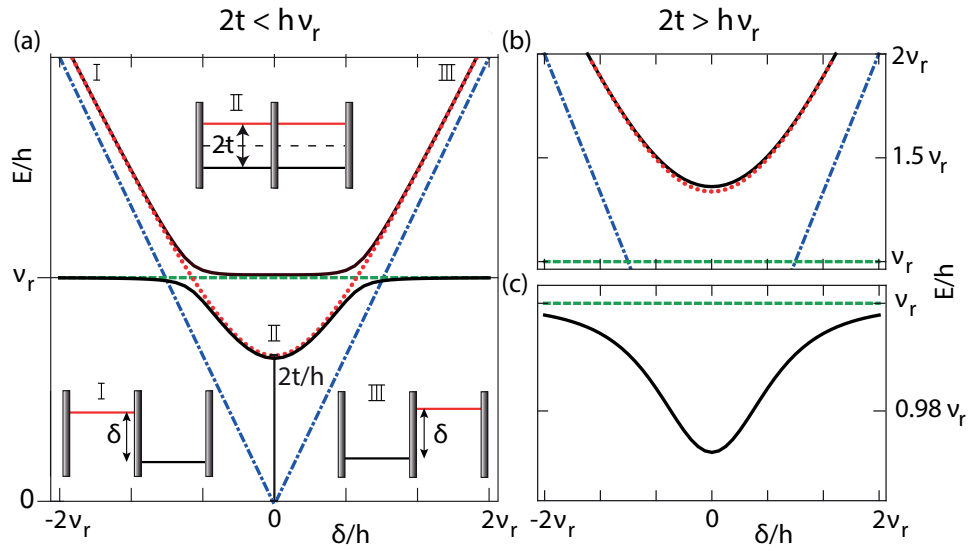

Figure 7.4.: Schematic of the two lowest eigenenergies of the coupled system (black line) for $2t < h\nu_r$. Horizontal green dashed line indicates the bare resonator frequency ν_r. Red dotted line indicate the DQD transition frequency ν_q. Insets I, III: Schematic of the charge states on each dot detuned by energy $\delta >> t$. Inset II: Schematic of the hybridized charge states in the double quantum dot, split by $2t$ at $\delta = 0$. (b) Transition frequency of the DQD for $2t > h\nu_r$. (c) Resonator frequency for $2t > h\nu_r$. Figure adapted from [43].

resolved spectral measurement, i.e. full frequency-dependent spectra at all values of δ, needs to be acquired ([2], [3]). Fig. 7.5a indicates the detuning axis along which resolved spectra (the magnitude of a transmitted microwave tone as a function of frequency) are measured (Fig. 7.5b).

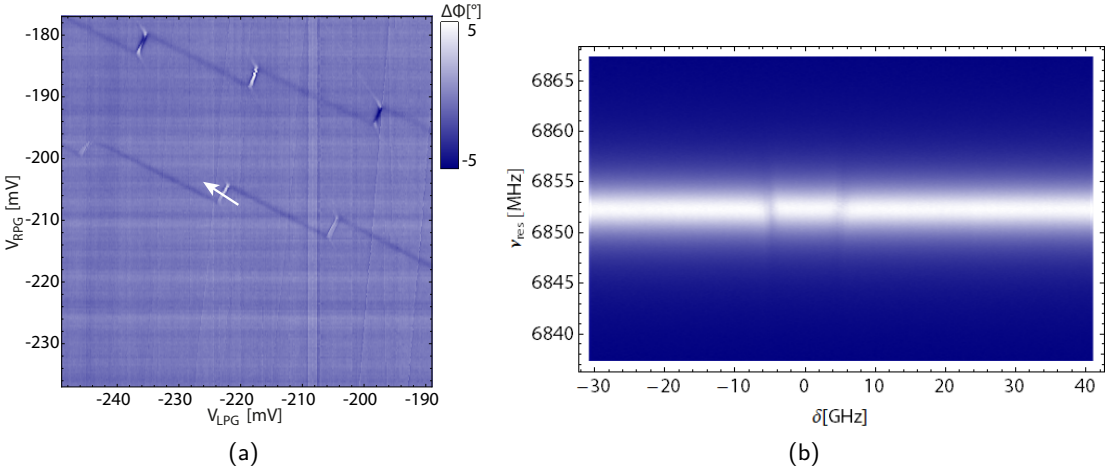

Figure 7.5.: (a) Detuning δ axis and (b) frequency dependent spectra acquired at various values of δ.

By fitting each spectrum to a Lorentzian function the resonance frequency ν_r and linewidth $\kappa/2\pi$ of the resonator response can be calculated. Fig. 7.6 shows the resonance frequency shift $\Delta\nu$ and linewidth of the resonator as a function of δ.

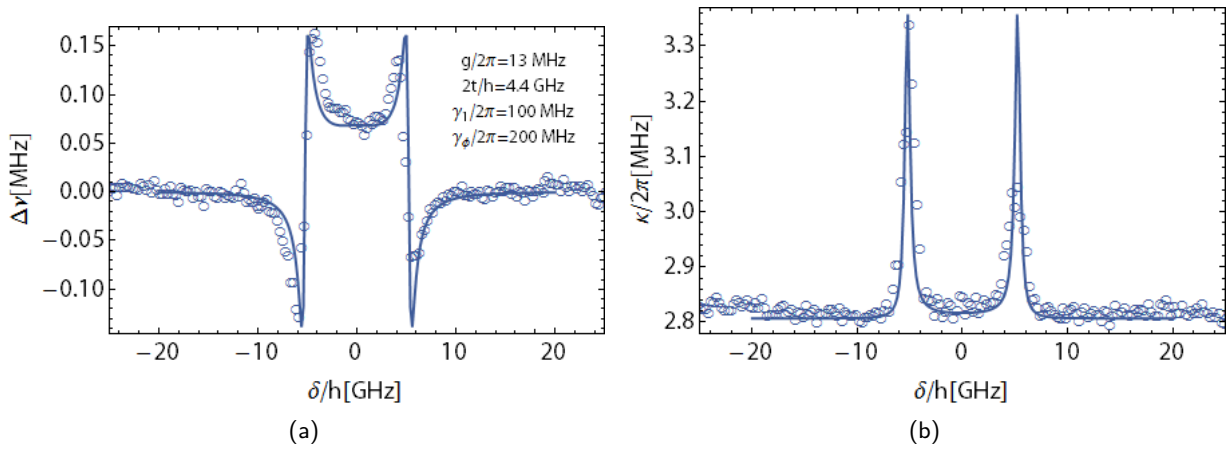

(a) (b)

Figure 7.6.: (a) Resonance frequency shift $\Delta\nu$ and (b) linewidth $\kappa/2\pi$ as a function of detuning δ.

So far we have only considered the unitary evolution of the Hamiltonian taking into account only interactions between a photon in the resonator and the DQD qubit. However, the Jaynes-Cummings Hamiltonian (equation 2.1) does not account for additional degrees of freedom, such as energy losses for the qubit or the cavity decay rate. To account for such dynamics, two theoretical concepts are helpful: the *input-output formalism* and the *equations of motion* in the Heisenberg picture.

Fig. 7.7 shows a resonator with an electric field mode a coupled to input and output transmission lines with a coupling given decay rates κ_1, κ_2, and a total decay rate $\kappa_1 + \kappa_2$. The behaviour of this system is described by the input-output formalism [50]. In this formalism each transmission line is described by an input mode ($a_{1,in}$, $a_{2,in}$) and an output mode ($a_{1,out}$, $a_{2,out}$). These modes interact with the field mode a in the resonator according to the following boundary conditions

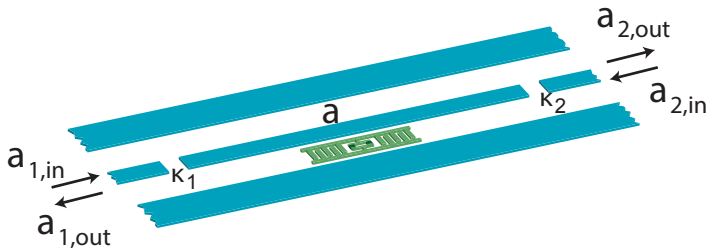

Figure 7.7.: Input-output theory applied to two-port circuit QED. Port modes a_1 and a_2 are decomposed into input $a_{1,in}$, $a_{2,in}$ and output modes $a_{1,out}$, $a_{2,out}$.

$$\begin{aligned} a_{1,out}(t) &= \sqrt{\kappa_1}a(t) - a_{1,in} \\ a_{2,out}(t) &= \sqrt{\kappa_2}a(t) - a_{2,in} \end{aligned} \tag{7.1}$$

Where $a\,(t)$ describes the field in the resonator. In the experiments performed during this project, we always measured the ouput at one port. Assuming port 2 as the port whose output we measure, equal decay rates $\kappa_1 = \kappa_2 = \kappa$, and remembering that on this side circulators are placed (see chapter 3) allows us to assume $a_{2,in} \approx 0$.

$$a_{out}(t) = \sqrt{\kappa/2}a(t) \tag{7.2}$$

The equations of motion tell us how the mode in the resonator a (remember that a is formally an annihilation operator) evolves in time. Using the same approximations they read [51]

$$\begin{aligned}\dot{a}(t) &= \frac{\partial a(t)}{\partial t} = -\frac{i}{\hbar}\left[a(t), H\right] - \frac{\kappa}{2}a(t) + \sqrt{\kappa}a_{in}(t) \\ \dot{\sigma^-}(t) &= \frac{\partial \sigma^-(t)}{\partial t} = -\frac{i}{\hbar}\left[\sigma^-(t), H\right] - \frac{\gamma}{2}\sigma^-(t)\end{aligned} \tag{7.3}$$

Where $\gamma = \gamma_1/2 + \gamma_\phi$ stands for the DQD decoherence rate, γ_1 the relaxation rate and γ_ϕ the dephasing rate. σ^- stands for the Pauli lowering operator. The first term on the equation for a describes the unitary evolution of the resonator, which is independent of κ. The second term is a damping term, which leads to a decay of the resonator field. The last term is an external driving force. Equation 7.3 is equivalent to the equation of motion for a driven and damped oscillator. To solve it, it is useful to work in Fourier space, thus we define the time Fourier transforms of a and σ^-

$$\begin{aligned}a(\omega) &= \frac{1}{\sqrt{2\pi}}\int a(t)e^{i\omega t}dt \\ \sigma^-(\omega) &= \frac{1}{\sqrt{2\pi}}\int \sigma^-(t)e^{i\omega t}dt\end{aligned} \tag{7.4}$$

Thus in Fourier space equation 7.3 reads (see also [51])

$$\begin{aligned}-i\omega a(\omega) &= -i\omega_r a(\omega) - ig\sigma^-(\omega) - \frac{\kappa}{2}a(\omega) + \sqrt{\kappa}a_{in}(\omega) \\ -i\omega\sigma^-(\omega) &= -i\omega_q\sigma^-(\omega) - iga(\omega) - \frac{\gamma}{2}\sigma^-(\omega)\end{aligned} \tag{7.5}$$

Defining $\Delta\omega_r = \omega_r - \omega$ and $\Delta\omega_q = \omega_q - \omega$ we can rewrite equation 7.5

$$\begin{aligned}0 &= -\left(i\Delta\omega_r + \frac{\kappa}{2}\right)a(\omega) - ig\sigma^-(\omega) + \sqrt{\kappa}a_{in}(\omega) \\ 0 &= -\left(i\Delta\omega_q + \frac{\gamma}{2}\right)\sigma^-(\omega) - iga(\omega)\end{aligned} \tag{7.6}$$

While the input-output approach results in a Heisenberg equation of motion for the field operator, the system dynamics can alternatively be expressed in terms of a density matrix ρ resulting an a *master equation* [51]. Equations 7.6 can be solved for a and σ^- analytically using a symbolic mathematical software such as *Mathematica*. Alternatively, using equations 7.2 and 7.6 we can define the transmission through the resonator as

$$T(\omega) = \frac{a_{out}(\omega)}{a_{in}(\omega)} \tag{7.7}$$

Equation 7.7 is an analytical expression for the measurement in Fig. 7.5b (remembering that what we measure is $|T(\omega)|$). Note that $\sqrt{\kappa}a_{in}(\omega)$ relates to the average occupation in the resonator and therefore depends on the input power. Furthermore, the relaxation and dephasing rates (γ_1 and γ_ϕ) mix along the detuning δ [11]

$$\begin{aligned}\gamma_1 &= \gamma_1 \sin^2(\theta) + \gamma_\phi \cos^2(\theta) \\ \gamma_\phi &= \gamma_\phi \sin^2(\theta) + \gamma_1 \cos^2(\theta)\end{aligned} \tag{7.8}$$

Where $\theta = \arctan(2t/\delta)$. Thus, we can alternatively write equation 7.8 as

$$\gamma_1 = \gamma_1 \left(\frac{2t/h}{\nu_q}\right)^2 + \gamma_\phi \left(\frac{\delta/h}{\nu_q}\right)^2$$
$$\gamma_\phi = \gamma_\phi \left(\frac{2t/h}{\nu_q}\right)^2 + \gamma_1 \left(\frac{\delta/h}{\nu_q}\right)^2 \tag{7.9}$$

We now observe that the solution to equation 7.6 can be used to simulate the measurement in Fig. 7.5b and thereby fit the measurement in Fig. 7.6 obtaining estimates for parameters of interest such as the interdot tunnel coupling t, dephasing γ_ϕ or relaxation γ_1. In practice we fix $\gamma_1/2\pi$ =100 Mhz assuming it to be a reasonable value for charge qubits [52]. The resonator resonance frequency $\omega_r = 2\pi\nu_r$ and linewidth $\kappa/2\pi$, or equivalently its quality factor, are parameters which can be obtained by measuring its spectrum while the DQD is Coulomb blockaded. As shown in Fig. 7.6a, for the sample used in the experiments presented in this report, we estimated a dephasing rate $\gamma_\phi/2\pi$ =200 MHz which represents an improvement of roughly 20 times in relation to previous samples [3]. This is a significant improvement which could enable experiments which previously were quite challenging or even impossible, such as qubit spectroscopy [53]. During the course of the project several improvements took place: a RF filter was added to the DC gate lines inputs and the sample was fabricated on a new wafer. It is therefore not yet clear which of the changes had the most influence on the improved qubit dephasing.

Microwave readout in the non-linear transport regime The same dispersive readout measurements made at zero bias (Fig. 7.3) can be made when $V_{SD} \neq 0$. The strategy is identical: driving the resonator at its resonance frequency ν_r, measure the transmitted amplitude and phase. The observed shifts in amplitude and phase are the result of the dispersive interaction between the resonator excitation and the DQD. Fig. 7.8 shows a dispersive readout measurement for the finite bias triangles shown in Fig. 6.5b. The white arrows indicate the an excited state.

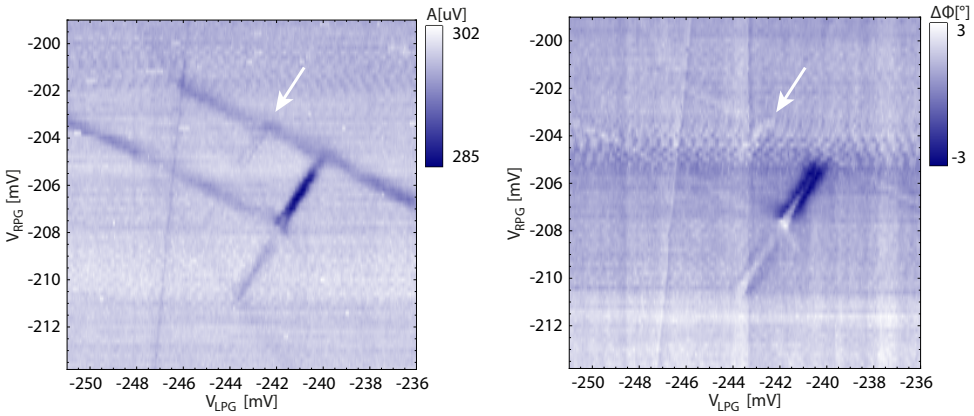

Figure 7.8.: Charge stability diagrams measured at high frequency for $V_{SD} \neq 0$. (a) Transmitted amplitude of a microwave tone at the resonator eigenfrequency ν_r and (b) phase.

Fig. 7.9 schematically shows the case when the DQD is biased. The idea is that $V_{SD} \neq 0$ leads to inelastic tunneling processes which eventually can lead to photon emission. We intend to use the

resonator as a sensitive tool to probe this emission. Given its limited linewidth κ, frequencies away from ν_r do not couple into the resonator making it act as a filter for the radiation emitted by the DQD.

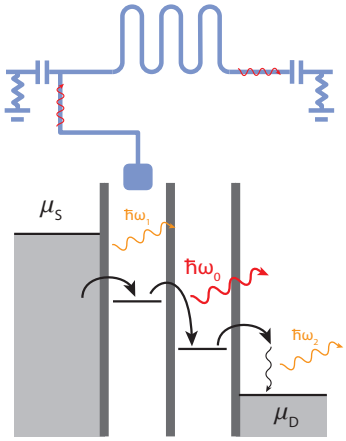

Figure 7.9.: Schematic of a biased DQD coupled to a resonator. Red arrows indicate a radiative transition when an electron tunnels from one dot to the other emitting a photon with frequencies in a bandwidth κ around $\nu_q = \nu_r$. Yellow arrows account for transitions when an electron tunnels from(to) the leads emitting a photon (with a frequency outside the resonator bandwidth), a phonon or both.

In the next sections we will deal with emission experiments. The experiments presented here were performed at resonance, i.e. $\delta = 0$. The reason is that due to conservation of energy, strong emission is expected close to resonance; elastic processes into and out of the DQD dominate when $\delta = 0$ [54] and the effective coupling $g = g_0\,(2t/\nu_q)$ vanishes for large δ ([11], [46]). To check this, we tuned the DQD to a gate configuration in which $2t/h \approx \nu_r$ using the same strategy as for the measurement in Fig. 7.6. Fig. 7.10a shows a dispersive readout at zero bias of the phase shifts around the interdot transfer line in Fig. 7.8. The white arrow indicates the detuning axis along which a spectral measurement similar to that in Fig. 7.5b is taken. Fig. 7.10b shows the resonance frequency shift $\Delta\nu$ together with estimated qubit parameters.

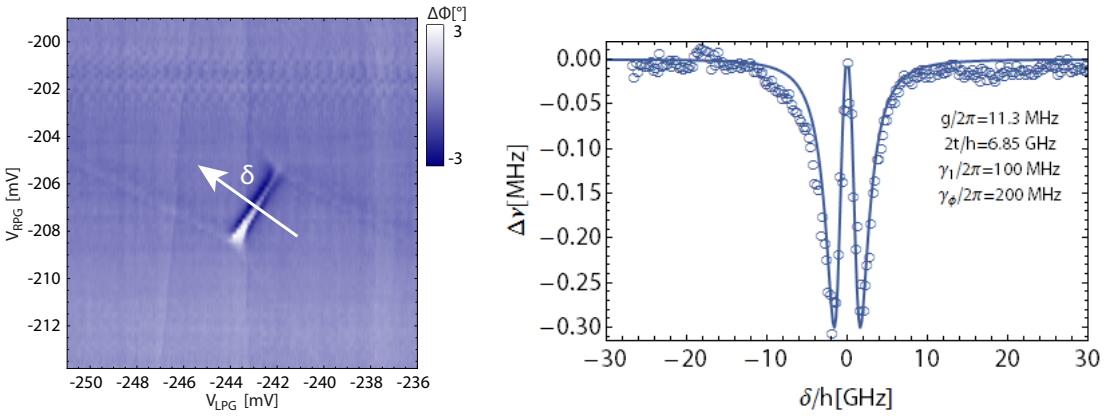

(a) (b)

Figure 7.10.: (a) Phase shifts of a transmitted microwave tone at frequency ν_r around the finite bias triangle region (Fig. 6.5b). Frequency shift $\Delta\nu$ as a function of detuning δ for a spectral measurement at each point along the detuning line (white arrow in (a)).

7.2. First order correlation function

In section 5.1 we described the setup used to measure observables such as mean amplitude, power and correlations. In this section we describe the main theoretical aspects involved in the measurement of first order correlation functions, which by the Wiener-Khinchin theorem (equation 5.6) are equivalent to power spectral densities. We follow a close description to that in [55] and [56]. Fig. 7.11 shows a schematic of our signal processing setup in a simplified way.

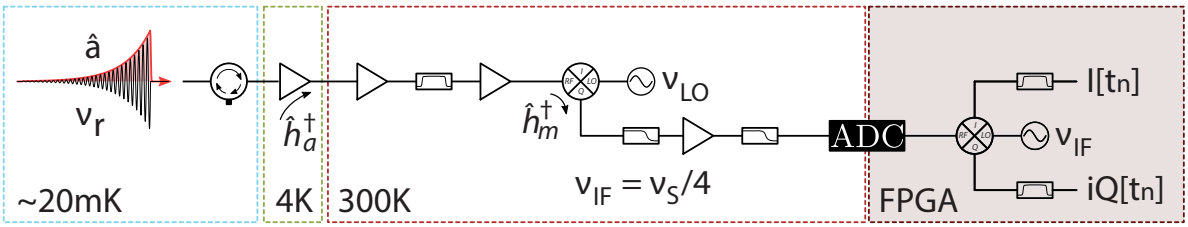

Figure 7.11.: Simplified measurement setup consisting of amplification, demodulation and low-pass filtering. Fig. adapted from [33].

The field in the resonator can be decomposed into two propagating plane waves travelling in the forward and backward direction $E(t) = E^+(t) + E^-(t)$ which correspond to the positive and negative frequency components of its spectrum. Since $E(t)$ can only take real values, its spectrum is hermitian symmetric $E(\omega) = E(-\omega)^*$.

$$E(t) = E^+(t) + E^-(t) = E^+(t) + \left(E^+(t)\right)^* \tag{7.10}$$

Assuming that the electric field is quasi-monochromatic with a center frequency $\omega_0 = 2\pi\nu_0$ and limited in bandwidth $B << \nu_0$, we can rewrite $E^+(t)$ in terms of a complex valued function $S(t)$ with center frequency 0 and bandwitdth B called the complex envelope of $E(t)$ [34].

$$E^+(t) = S(t)e^{-i\omega_0 t} \tag{7.11}$$

Equation 7.10 can then be written as

$$E(t) = S^*(t)e^{i\omega_0 t} + S(t)e^{-i\omega_0 t} \tag{7.12}$$

Our measurement setup extracts precisely $S(t)$. In a conceptual way we can think of the process as follows (equation 7.13): after amplification (1) the electric field becomes $\sqrt{g}E(t)$ where g is the power gain of the amplifier. Upon demodulation (2) the signal is multiplied by $e^{i\omega_0 t}$ and is finally low pass filtered (3).

$$\begin{aligned} E(t) &\xrightarrow{1} \sqrt{g}E(t) \xrightarrow{2} \sqrt{g}E(t)e^{i\omega_0 t} \\ \sqrt{g}E(t)e^{i\omega_0 t} &= \sqrt{g}S^*(t)e^{i2\omega_0 t} + \sqrt{g}S(t) \xrightarrow{3} \sqrt{g}S(t) \end{aligned} \tag{7.13}$$

Associating an operator s to the complex envelope function, it has been shown [55] that $s^\dagger = s^*$ and $\left[s^\dagger, s\right] = 0$, meaning that it is a classical operator. We thus observe that the complex envelope is formally equivalent to the annihilation operator

$$E(t) \propto a + a^\dagger \propto s + s^* \tag{7.14}$$

Let us consider an output mode of the resonator a_k. After amplification we obtain $a_{k,a} = \sqrt{g}e^{i\phi_a}a_k + \ noise$, where $e^{i\phi_a}$ accounts for a phase shift because the signal has to travel to and through the amplifier. Since photons are bosons, the creation(annihilation) operators between any two modes should obey the boson commutation relations given by [51].

$$\begin{aligned} [a_i, a_j] &= \left[a_i^\dagger, a_j^\dagger\right] = 0 \\ \left[a_i, a_j^\dagger\right] &= \delta_{ij} \end{aligned} \tag{7.15}$$

In order to fulfill $\left[a_{k,a}, a_{k,a}^\dagger\right] = 1$, a noise mode needs to be associated with the amplifier [57].

$$a_{k,a} = \sqrt{g}e^{i\phi_a}a_k + \sqrt{g-1}h_{k,a}^\dagger \tag{7.16}$$

Where $h_{k,a}^\dagger$ is the noise mode added by the amplifier. As explained in section 5.1 and depicted in Fig. 7.11 we use a heterodyne detection scheme measuring only one signal component after IQ-mixing. Therefore, the mixing process also adds noise because the positive and negative frequency components can not be distinguished after this step (see Fig. 5.2).

$$s_k = \frac{1}{\sqrt{2}}\left(a_{k,a}e^{i\phi_m} + h_{k,m}^\dagger\right) = \sqrt{\frac{g}{2}}e^{i\left(\phi_{k,a}+\phi_{k,m}\right)}a_k + \sqrt{\frac{g-1}{2}}e^{i\phi_{k,m}}h_{k,a}^\dagger + \sqrt{\frac{1}{2}}h_{k,m}^\dagger \tag{7.17}$$

Where the $\sqrt{1/2}$ factor accounts for the rms value and the subindex m for noise and phase added during the mixing process. Making the following substitutions

$$\begin{aligned} \phi &= \phi_{k,a} + \phi_{k,m} \\ g^{'} &= \sqrt{\frac{g}{2}} \\ h &= \sqrt{\frac{g-1}{g}}e^{i\phi_a}h_{k,a} + \sqrt{\frac{1}{g}}e^{i\phi}h_m \end{aligned} \tag{7.18}$$

We obtain equation 7.19 where h is an effective noise mode, $g^{'}$ is the effective gain, and ϕ the effective phase shift after passing the amplifier and mixer.

$$s = s_k = \sqrt{g'}e^{i\phi}\left(a_k + h^\dagger\right) \tag{7.19}$$

It is worth remembering that a_k is given by the input-output formalism (equation 7.1). According to equation 5.2, the first order correlation for two modes i, j is given by

$$\begin{aligned} G^1(\tau) &= \langle E^*(t)E(t+\tau)\rangle = \langle E^*E(\tau)\rangle \\ G_{ij}^1(\tau) &= \left\langle a_i^\dagger a_j(\tau)\right\rangle \end{aligned} \tag{7.20}$$

For simplicity and because it is what we actually measured during the project, let us assume $i = j$, i.e. the autocorrelation. Since the quantity we measure is s the autocorrelation measurement is:

$$\begin{aligned}\Gamma^1(\tau) = \left\langle s_k^\dagger s_k(\tau)\right\rangle &= g^{'}\left\langle \left(a_k + h^\dagger\right)^\dagger \left(a_k(\tau) + h^\dagger(\tau)\right)\right\rangle \\ &= g^{'}\left\langle \left(a_k^\dagger + h\right)\left(a_k(\tau) + h^\dagger(\tau)\right)\right\rangle \\ &= g^{'}\left\langle a_k^\dagger a_k(\tau) + hh^\dagger(\tau) + a_k^\dagger h^\dagger(\tau) + ha_k(\tau)\right\rangle\end{aligned} \tag{7.21}$$

Remembering that the expectation value of the noise $\langle h(\tau)\rangle = 0$ and assuming that the field and noise modes are uncorrelated we obtain

$$\Gamma^1(\tau) = g^{'}\left\langle a_k^\dagger a_k(\tau) + hh^\dagger(\tau)\right\rangle \tag{7.22}$$

Assuming the noise to be white [34], the first order correlations of noise read

$$H_{ij}^1(t+\tau) = \left\langle h_i^\dagger(t) h_j(t+\tau)\right\rangle = N_{ij}\delta(\tau) \tag{7.23}$$

Where $N_{ij}\delta(\tau)$ is an effective noise photon number. Equation 7.22 can then be rewritten as

$$\Gamma^1(\tau) = g^{'}G^1 + g^{'}\underbrace{\left\langle hh^\dagger(\tau)\right\rangle}_{H^1=(N+1)\delta(\tau)} \tag{7.24}$$

The general assumption is that when the resonator is left in the ground state, a_k is in the vacuum and hence all moments are zero $\left\langle \left(a^\dagger\right)^n (a)^m\right\rangle = 0$ and thereby a reference measurement accounts for how much noise is added by the amplifiers and mixer.

$$\Gamma_{ss}^1(\tau) \approx g^{'}H^1 \tag{7.25}$$

The autocorrelation function can therefore be estimated as the difference between two measurements: one with the source turned on and one with the source turned off.

$$G^1(\tau) = \frac{1}{g^{'}}\left(\Gamma^1(\tau) - \Gamma_{ss}^1(\tau)\right) \tag{7.26}$$

Using this measurement scheme, correlations up to second order have been measured ([14], [58], [21]). According to Fig. 7.9, our reference measurement simply consists of a measurement where $V_{SD} = 0$. Fig. 7.12a shows a PSD measurement when the source is on S_{on}(blue) and off S_{off} (purple). As observed, the difference is typically small and we therefore usually average over many on/off repetitions. The features of these measurement are identical to those shown conceptually in Fig. 5.2. Fig. 7.12b shows the difference $S_\Delta = S_{on} - S_{off}$ (blue) and an analytical fit (purple) where the axis has been normalized from the measured units (mV per Hz) to photons per Hz per second.

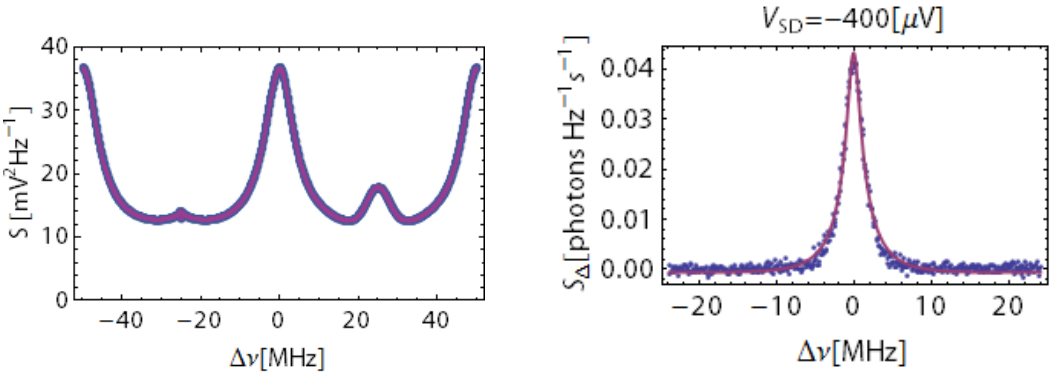

(a) (b)

Figure 7.12.: (a) Power spectral density measurement when the source is on (blue) S_{on} and off (purple) S_{off}. (b) PSD difference $S_\Delta = S_{on} - S_{off}$ with axis scaled using the vacuum assumption (equation 7.27).

The analytical fit in Fig. 7.12b is made to a multiplication of two Lorentzian functions. This is to account for the fact that the gain of our paramp exhibits a non-linear gain at around a selected frequency and bandwidth. From such a fit we can estimate the peak PSD, i.e. peak photon flux. With this measurement scheme, we measured S_Δ along the detuning axis (white arrow in Fig. 7.13a). Fig. 7.13b shows the peak S_Δ as a function of detuning δ.

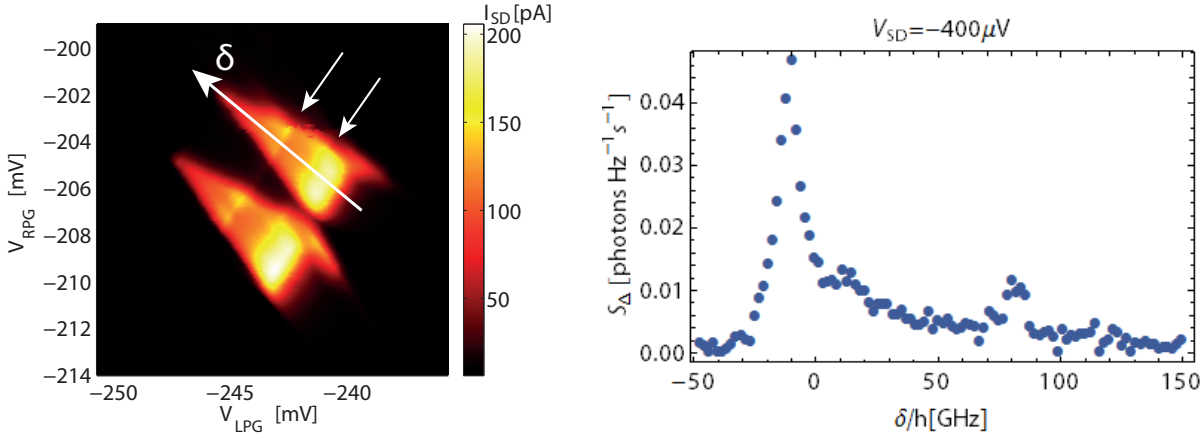

(a) (b)

Figure 7.13.: (a) Cut along the detuning axis in the top finite bias triangle. (b) Peak PSD (S_Δ) as a function of detuning.

To gain an insight into the features in Fig. 7.13b it is useful to plot it together with the measured DC current (purple dots in Fig. 7.14). Fig. 7.14 shows a background which follows with the current, plus two additional signal peaks. The background being linear with the current probably originates from inelastic processes whose frequency is within the resonator linewidth. The left most peak is associated with the configuration where the photon flux into the resonator is maximum, and the right most peak can be associated to the excited state shown in Fig. 7.13a. We also observe that the peak photon flux is quite small ≈ 0.05 photons per Hz per sec. Since we tuned the DQD to a configuration where its transition frequency was close to the interdot tunel coupling, the origin of the large peak close to zero detuning likely originates from inelastic processes when the DQD transition

frequency (red arrow in figure 7.4) matches the resonator eigenfrequency. We observe then how the resonator basically behaves as a sensitive probe for the radiation emitted by the DQD.

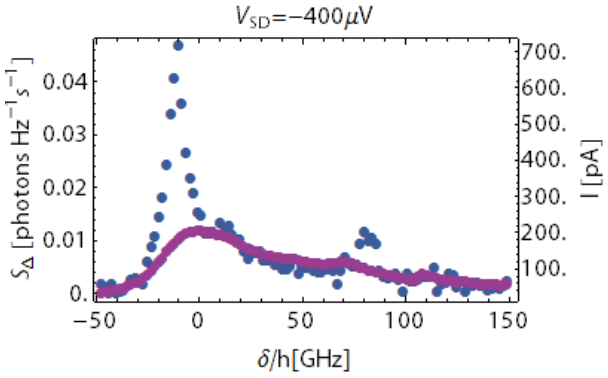

Figure 7.14.: Maximum PSD (blue) and measured DC current (purple) as a function of detuning δ.

Defining the average power coming out of the resonator $P = \hbar\omega_r \bar{n}_{out}$, where $\bar{n}_{out} = \bar{n}\kappa$ is the average number of photons leaving the resonator per Hz and per second. Being κ the linewidth of the resonator, we obtain at the current of approx 110 pA (where the maximum S_Δ occurs) $\bar{n}_{out} \approx 0.1675$ photons per μsec, which corresponds to approximately 2.2×10^{-4} photons per electron. This very low conversion efficiency has also been observed in a very similar experiment using a DQD formed on a InAs nanowire [59].

Approximate calibration of the measurement setup Scaling our PSD measurements as in Fig. 7.12b was only possible thanks to the use of a parametric amplifier. As mentioned in section 3.3 the device was developed in our lab by Christopher Eichler ([60],[4]). The quantum limited nature of the amplification obtained with such a device allowed us to make an rough calibration of our measurement setup. Following the description presented in appendix A6 of [60] we assume that when the resonator is left in the ground state, the input of the paramp is in the vacuum state plus some thermal occupation due to attenuation in the cables from the resonator output to the paramp input. In this way, measuring a PSD when the paramp is on and a PSD reference measurement when the paramp is turned off (i.e. only the cold HEMT amplifier is left in the amplification chain) the PSD difference at the point of maximum gain is given by equation 7.27

$$S_\Delta = S_{on} - S_{off} = (1 + 2\epsilon)\,(gain - 1)\,vacuum\ noise \tag{7.27}$$

We therefore observe that the ratio $(1 + 2\epsilon)\,(gain - 1)\,/S_\Delta = vacuum\ noise^{-1}$ gives us a scaling factor to convert from the measurement units to photons. Fig. 7.15a shows the paramp spectrum from which an amplitude gain can be extracted by fitting to a Lorentzian function. Fig. 7.15b shows a PSD measurement for the paramp pump on (blue) and off (purple). By subtracting both measurements (Fig. 7.16a) $S_\Delta = S_{on} - S_{off}$ can be estimated and using equation 7.27 we obtain a scaling factor which allows us to calibrate our measurement setup as shown in Fig. 7.16b. Note that the noise offset N_0 of our HEMT amplifier close to the resonator frequency lies around 100 while the paramp lies around 4. The deviation from the vacuum level is associated with attenuation in the cables and microwave components as well as noise added by the parametric amplifier and the HEMT [60].

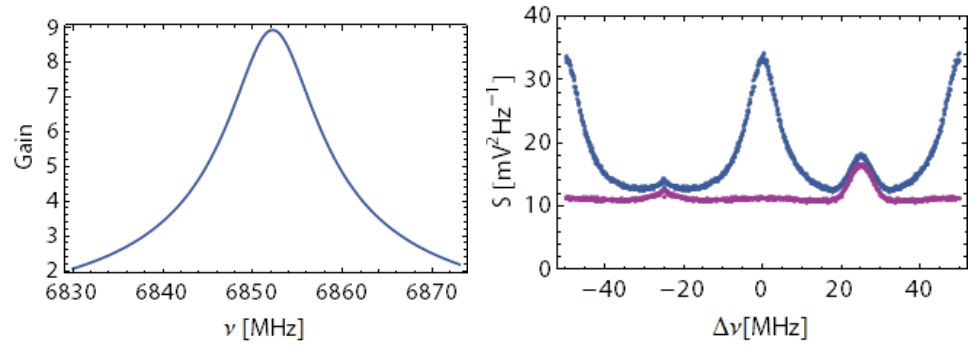

(a) (b)

Figure 7.15.: (a) Paramp spectrum response. (b) Measured PSD relative to the resonator frequency for the parametric amplifier pump turned on (blue) and turned off (purple).

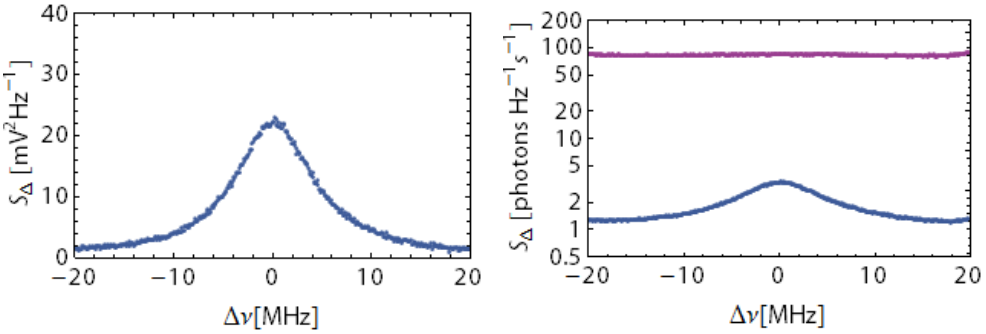

(a) (b)

Figure 7.16.: (a) PSD difference $S_\Delta = S_{on} - S_{off}$ for a measurement for the paramp pump turned on and off (Fig. 7.15b). (b) Measured power spectral density S_Δ relative to the resonator frequency for the parametric amplifier pump turned on (blue) and for the pump turned off (purple) scaled according to equation 7.27.

7.3. Second order correlation function

Having observed peaked emission for a particular detuning, as a last measurement we intended to probe other correlation of great interest for the radiation at the emission peak. The field intensity autocorrelation

$$\begin{aligned} G^2(t, t+\tau) &= \langle I(t) I(t+\tau) \rangle \\ &= \left\langle a^\dagger(t) a(t) a^\dagger(t+\tau) a(t+\tau) \right\rangle \\ &= \left\langle a^\dagger(t) a^\dagger(t+\tau) a(t) a(t+\tau) \right\rangle \end{aligned} \tag{7.28}$$

In the context of stellar interferometry, the first experiments to measure this function were performed by Hanbury Brown and Twiss (HBT) in 1956 [61]. For classical light sources, it can be shown that $G^2(0) > G^2(\tau)$ whereas for non-classical light $G^2(0) < G^2(\tau)$. An interpretation of these observations for classical light is that detecting two photons simultaneously is more probable

than one after another. Photons tend to arrive in *bunches* and the effect is called *photon bunching*. For non-classical light the opposite holds: photons tend to arrive one after another, called *photon antibunching*. Using microwaves, measurements of this function have been performed in our lab using the same offset substraction strategy described in section 7.2 measuring the field intensity $s^\dagger s \propto a^\dagger a$ instead of the field amplitude $s \propto a$ ([14], [58]). These experiments are performed conceptually in the following way. A qubit is prepared in an excited state and its transition frequency is tuned to match the resonator frequency. The qubit excitation decays into the resonator in form of a photon which leaves the cavity after a time $1/\kappa$ and is acquired by the measurement setup. A reference measurement corresponds to the case when the resonator is left in the ground state (i.e. the qubit is left in the ground state). This process is repeated several times to obtain an average result. As you may observe, there must be a delicate control of the timing during the experiments, i.e. qubit preparation and signal acquisition are triggered in a controlled way [14]. As shown in equation 7.24, correlations are in principle measurable without the need of reference substraction. The problem is that the effective noise photon numbers are typically larger than the signals we are interested in, and therefore the quantities of interest are typically hidden in a large noise background. Furthermore, the noise background may fluctuate in time (fluctuations in the amplifiers, cables, etc.).

Here we used a different approach introduced in ([60], [19], [18]). We now intuitively and briefly introduce the strategy. The quantity we access in our experiments is the complex envelope function $s = I + iQ = a + h^\dagger$. One can fill a 2 dimensional histogram by recording samples of s and storing them in the complex plane. It has been shown in ([60], [18]) that these histograms formally correspond to a probability distribution. We are interested in the correlations of s, and since correlations are moments, they can be calculated based on their probability distribution. As shown in [18], the moments of s at $\tau = 0$ are given by equation 7.29

$$\left\langle \left(s^\dagger\right)^n (s)^m \right\rangle_{\rho_a} = \int_s (s^*)^n (s)^m D^{[\rho_a]}(s) \tag{7.29}$$

Where $D^{[\rho]}(s)$ is the probability distribution of s for a state a characterized by the density matrix ρ_a. Once more, assuming that the signal and the noise are uncorrelated $\rho = \rho_a + \rho_h$ the moments can be decomposed into products [60]

$$\left\langle \left(s^\dagger\right)^n (s)^m \right\rangle_{\rho_a} = \sum_{i,j=0}^{m,n} \begin{pmatrix} m \\ j \end{pmatrix} \begin{pmatrix} n \\ i \end{pmatrix} \left\langle \left\langle \left(a^\dagger\right)^i (a)^j \right\rangle \left\langle (h)^{n-i} \left(h^\dagger\right)^{m-j} \right\rangle \right\rangle \tag{7.30}$$

Assuming that when the resonator is left in the ground state a is in the vacuum, and hence all moments are zero $\left\langle \left(a^\dagger\right)^n (a)^m \right\rangle = 0$, a reference measurement gives access to the noise moments

$$\left\langle \left(s^\dagger\right)^n (s)^m \right\rangle_{\rho_n} = \left\langle (h)^n \left(h^\dagger\right)^m \right\rangle \tag{7.31}$$

We now observe from equation 7.30 that having a measurement $\left\langle \left(s^\dagger\right)^n (s)^m \right\rangle$ and a reference $\left\langle (h)^n \left(h^\dagger\right)^m \right\rangle$ a set of equations for the moments we are interested in $\left\langle \left(a^\dagger\right)^i (a)^j \right\rangle$ is obtained. It is further shown in appendix A1 of [60] that in terms of cumulants equation 7.30 reads

$$\left\langle \left\langle \left(a^\dagger\right)^n (a)^m \right\rangle \right\rangle = \left\langle \left\langle \left(s^\dagger\right)^n (s)^m \right\rangle \right\rangle - \left\langle \left\langle (h)^n \left(h^\dagger\right)^m \right\rangle \right\rangle \tag{7.32}$$

Using existing data analysis tools we performed histogram measurements of the radiation emitted from the biased DQD at the configuration where maximum emission was observed (Fig. 7.14). The experiment consists of measuring a pair of histograms (one when $V_{SD} \neq 0$ and one when $V_{SD} = 0$) many times, calculating the moments for each histogram pair (intuitively as in equation 7.32) and

finally averaging the moments. Fig. 7.17 shows the average histogram of the complex envelope s for the case when the source (DQD biased) is turned on (a), off (b) and the difference on-off ((a)-(b)).

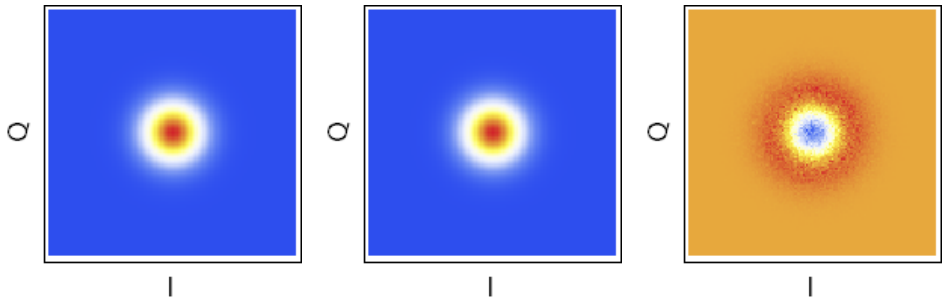

Figure 7.17.: (a) Histogram of complex envelope s when the source is turned on, i.e. DQD is biased, (b) turned off and (c) difference.

Fig. 7.18a shows the marginal distribution of the histogram in Fig. 7.17c. Fig. 7.18b shows the average absolute value of the moments $\left|\left\langle \left(a^{\dagger}\right)^{n}(a)^{m}\right\rangle\right|$ up to $n, m = 2$.

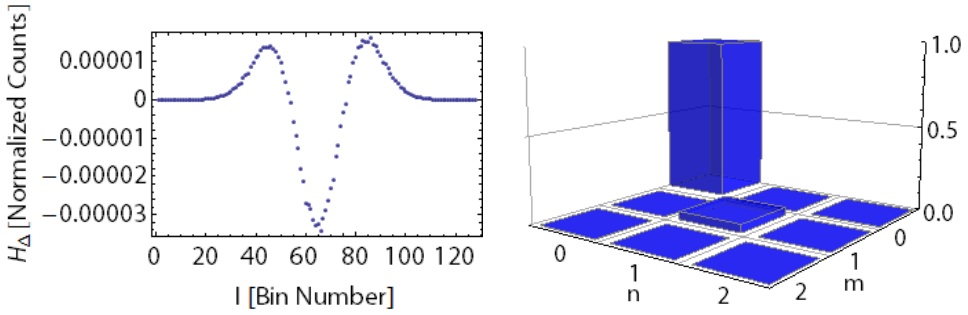

Figure 7.18.: (a) Marginal distribution of the histogram with substracted background (Fig. 7.17c). (b) Absolute value of the field moments $\left|\left\langle \left(a^{\dagger}\right)^{n}(a)^{m}\right\rangle\right|$ up to order $n, m = 2$.

Fig. 7.19 shows the calculated value of the first and second order correlation functions at $\tau = 0$ for each measured histogram. The estimated mean and standard deviation are $\mu_{g1} = 0.0501$, $\sigma_{g1} = 0.0212$ and $\mu_{g2} = 9.936 \times 10^{-6}$, $\sigma_{g2} = 0.11$.

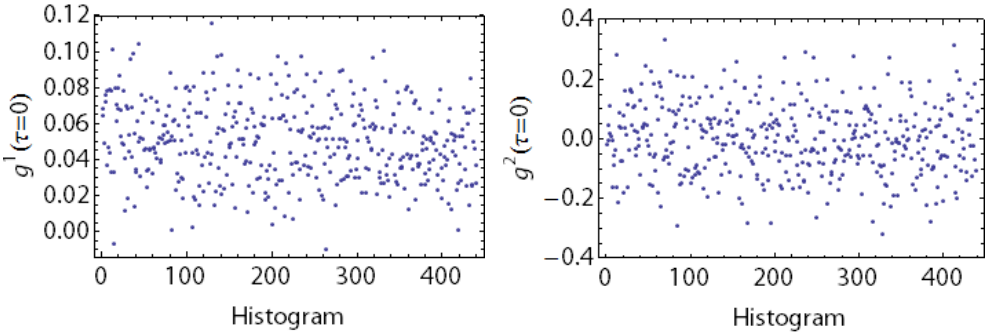

(a) (b)

Figure 7.19.: (a) First and (b) second order correlation function at $\tau = 0$ for each measured histogram.

Fig. 7.20a shows the measured current as a function of time during the period over which the histograms were measured. Note the high stability of the DQD configuration over this period of time. Using the *Jacknife* statistical re-sampling technique we calculated the mean and standard deviation of the mean for g_1 and g_2 (i.e. mean and standard deviation of the mean for data in figures 7.19a and 7.19b). Fig. 7.20b shows the real (red) and imaginary (blue) part of the mean g_1 and g_2 normalized according to

$$\left(\tilde{a}^\dagger\right)^n \tilde{a}^m = \frac{\left\langle \left(a^\dagger\right)^n a^m \right\rangle}{\left\langle a^\dagger a \right\rangle^{\frac{n+m}{2}}} \tag{7.33}$$

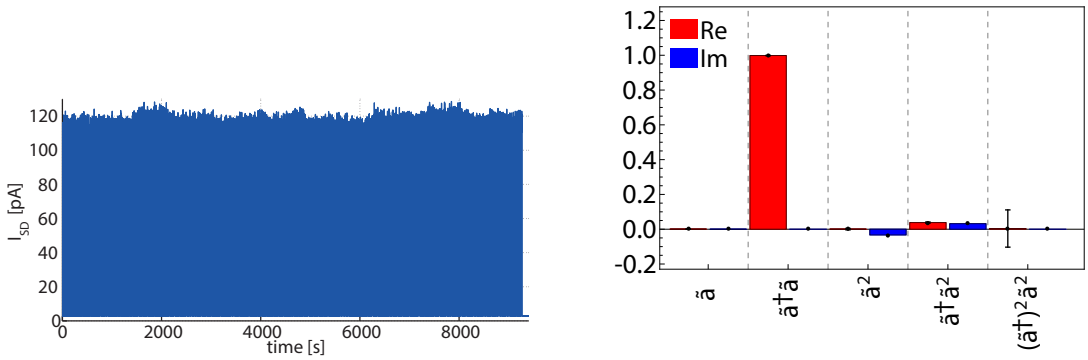

(a) (b)

Figure 7.20.: (a) Measured current as a function of time during the period over which histograms were measured. (b) Real (red) and imaginary (blue) part of the mean g_1 and g_2 normalized according to equation 7.33. Vertical lines are an estimate of the error in the calculated mean.

In Fig. 7.18b and 7.20b we observe vanishing off-diagonal moments and the higher order moments exponentially going to zero. This behaviour corresponds to that expected for a single photon source [60], [19], [18]. In order to check these estimates, we intended to make the same histogram measurement but instead of using the DQD as a radiation source, using a weak coherent signal with an average power similar to the average maximum power emitted by the DQD. The first thing we found out was that the phase of the acquired signal was not stable at all over time, showing random jumps over 2π radians. After checking the experimental setup, we found out that there was an

incorrect timing configuration. As shown in Fig. 7.11, after IQ-mixing the signal is centered around an intermediate frequency ν_{IF} and digitized every 10 ns. For the case of histogram measurements, we use a trigger which indicates when a sample is picked and stored in a histogram. The point here is that this trigger needs to be commensurate with the intermediate frequency ν_{IF}. We were using a trigger of 20 MHz to sample a signal at 25 MHz, as result the acquired complex envelope showed random phase shifts. Furthermore, the clock used as a trigger has small delays which may result in $\pi/2$ phase shifts depending on the trigger arrival time at the FPGA. As explained in Fig. 5.2, due to the way digital downconversion is made, if the histogram trigger arrives delayed with respect to the internal clock of the FPGA, the sample stored in the histogram will be shifted by $\pi/2$ radians. Changing the triggering device and adjusting its rate to 12.5 MHz allowed us to avoid random phase variations, however phase shifts of roughly 40 degrees over a period of 3 hours were still observed. Fig. 7.21 shows an average histogram with substracted reference (a) for a weak microwave tone as well as its marginal distribution (b). Fig. 7.22a shows the measured power spectral density S_Δ for the weak microwave tone in Fig. 7.21a. The absolute value of the normalized moments is shown in Fig. 7.22b. Coherent states of light are those that most closely resemble a classical description of the electromagnetic field. For such a signal with mean amplitude α, $a = \alpha$ and $a^\dagger = \alpha^*$. Hence the moments scale as $\left\langle \left(a^\dagger\right)^n (a)^m \right\rangle = \alpha^{n+m}$. Therefore, the normalized moments (equation 7.33) should be 1. As observed in Fig. 7.22b all moments tend to go to 1, however the moment $n+m=4$ shows a deviation from this value. As investigated theoretically in [55], the statistical error of the moments increases with increasing order. The number of measurements required to extract a moment of order M with a given precision scales with $(1+N_0)^M$, where N_0 is the effective noise photon number (see Fig. 7.16b). Therefore, the measurement time necessary to determine higher order moments with a fixed precision scales exponentially with increasing order [60].

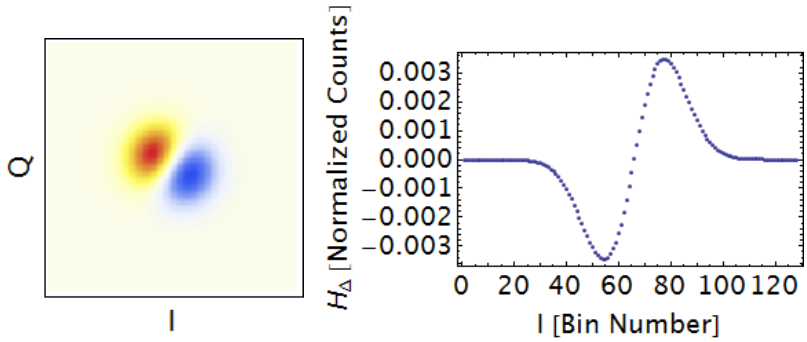

(a) (b)

Figure 7.21.: Histogram measurements for a weak coherent signal. (a) Average histogram with substracted background. (b) Marginal distribution of the histogram in (a).

With the modified trigger settings we tried to repeat the histogram measurement using again DQD as photon source. Figures 7.23 and 7.24 show qualitatively somewhat similar results as for the first measurement (Fig. 7.20), although some residual bunching is observed (Fig. 7.24b) as $\left(a^\dagger\right)^2 a^2$ deviates from zero.

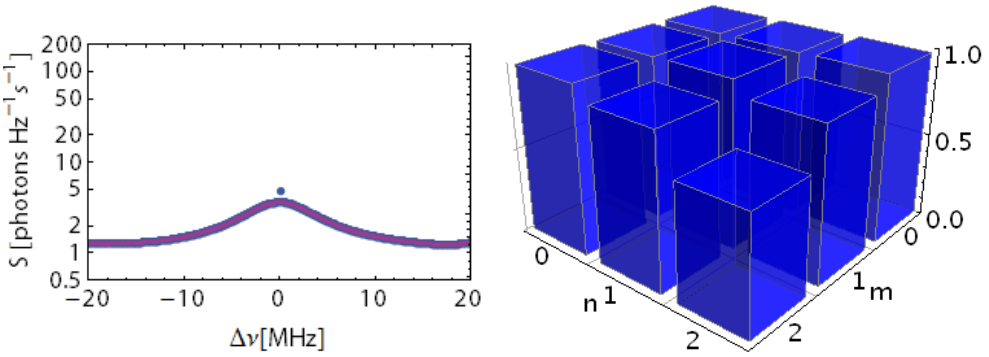

(a) (b)

Figure 7.22.: (a) Power spectral density measured for a weak coherent signal. (b) Absolute value of the normalized field moments for a weak coherent signal up to order $n, m = 2$ (equation 7.33).

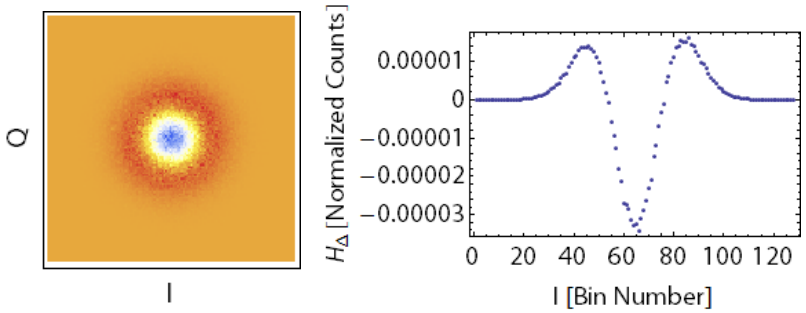

(a) (b)

Figure 7.23.: Histogram measurement with modified trigger settings. (a) Average histogram with substracted background. (b) Marginal distribution of the histogram in (a).

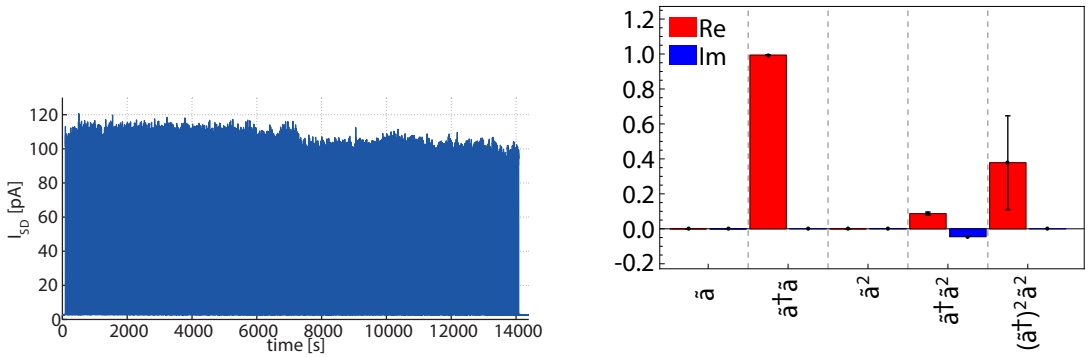

(a) (b)

Figure 7.24.: Histogram measurement with modified trigger settings. (a) Measured current as a function of time during the period over which histograms were measured. (b) Real (red) and imaginary (blue) part of the mean g_1 and g_2 normalized according to equation 7.33. Vertical lines are an estimate of the error in the calculated mean.

Second order moments give an insight in the nature of the light being probed. The behaviour we observe, of vanishing off-diagonal moments and the higher order moments exponentially going to zero corresponds to that expected for single photons. As presented in section 7.2, we tuned the DQD in a configuration such that the DQD transition frequency was approximately equal to the interdot tunnel $2t/h$ coupling. Our measurements suggest that the inelastic tunneling processes taking place under this conditions when the DQD is biased lead to a peak photon emission when the transition frequency of the DQD matches the resonator frequency. As shown in chapter 6, the DQD is in a Couloumb blockade regime, i.e. a regime where conceptually electrons tunnel one by one through it. Our observations suggest that in this regime, inelastic processes corresponding to the DQD transition frequency (red arrows in Fig. 7.4) lead to emission of single photons. This results should nevertheless be considered as preliminary, and are subject of further verification.

CHAPTER 8

Conclusion and Prospects

The initial goal of this project was the realization of measurements of correlation functions of the electric field to investigate radiation emitted from a DQD. However, during the most part of the project we did not have a working sample. Either our resonators had a very low quality factor, or DC gate lines did not allow to form a nice double dot potential. We therefore tried to investigate whether possible origins for the low quality factors by means of simulations and dip stick measurements as described in chapter 4. We found that neither wire bond placement or features in the gate design of our samples were likely to have had a strong influence on the quality factor of the resonator. However, results in chapter 4 allowed us to get a better understanding of the effects of wire bonds on the resonator characteristics and motivate the future use of airbridges. Based on simulations we also suggested possible improvements in the sample design.

Digital filters make a fundamental part of our signal processing scheme. While the Virtex-4 FPGA platform has been very well developed over the last years, work on a high bandwidth (currently a Virtex-6 platform) is still an ongoing task. The difficulty in programming applications for the Virtex-6 FPGA lies in the fact that the signal processing needs to be done in a parallel fashion. As described in chapter 5, during this project I engaged in the firmware development of the Virtex-6 FPGA platform by designing and implementing a configurable parallel filter. The developed firmware now enables the measurement of autocorrelations with a high bandwidth (1 GHz).

During the course the project several improvements to our measurement setup were made. The addition of a low pass filter to the DC wiring of the sample allowed to reduce the electronic temperature down to $\approx$ 60 mK. A parametric amplifier was introduced into the measurement setup, increasing our signal to noise ratio and thereby reducing the measurement time of experiments such as those presented in section 7.3 from days to hours.

Towards the end of the project we obtained a working sample on which the experiments presented in chapters 6 and 7 were made. We characterized the DQD both at low and high frequency. In sections 7.2 and 7.3 we intended to probe the emission from the biased DQD. A power spectral density measurement as a function of detuning between the electronic charge states in the DQD revealed peaked emission at particular values of detuning. The observed that maximum photon emission did not match the configuration of maximum current flowing through the DQD. As shown in figure 7.14, peaks in current are observed both near zero detuning as well as around an excited state in the DQD. The observed emission peak appears before the maximum in current, while a second peak associated to an excited state in the DQD appears to the right of its local current maximum.

The observed behaviour is not yet understood and is subject of current investigation. Furthermore, all measurements in chapters 6 and 7 were performed using the same DQD configuration (i.e. interdot tunnel coupling and couplings to the leads). It may well be possible that different behaviour arises for different tunnel couplings. This is also subject of current experiments.

Observing a peak in emission from the DQD, towards the very end we intended to get an insight on the nature of the emitted radiation. In section 7.3 we presented some measurements of the second order correlation function by means of histogram measurements developed in [60]. We observed correlations which correspond to those of single photons. In a first attempt to verify these observations, we tried to compare them with a weak coherent signal whose behaviour is in principle known. As shown in section 7.3 we found a fundamental problem in our measurement timing settings which lead to the observation of random phase shifts in the measured signal. With commensurate timing settings, the behaviour we observed for a weak coherent signal looks qualitatively different than that of the radiation originating from the DQD. We did not have time to further verify and check these measurements; it is therefore a task subject of future experiments. Nevertheless, considering the very low photon emission rate of the DQD, it may not be too surprising if future experiments verify the apparent observation of individual photons.

Bibliography

[1] A. Wallraff, D. Schuster, A. Blais, L. Frunzio, R. Huang, J. Majer, S. Kumar, S. Girvin, and R. Schoelkopf, "Strong Coupling of a Single Photon to a Superconducting Qubit using Circuit Quantum Electrodynamics," *Nature*, vol. 431, pp. 162–167, Sep 9 2004.

[2] T. Frey, P. J. Leek, M. Beck, A. Blais, T. Ihn, K. Ensslin, and A. Wallraff, "Dipole Coupling of a Double Quantum Dot to a Microwave Resonator," *Physical Review Letters*, vol. 108, Jan 25 2012.

[3] J. Basset, D.-D. Jarausch, A. Stockklauser, T. Frey, C. Reichl, W. Wegscheider, T. M. Ihn, K. Ensslin, and A. Wallraff, "Single-electron Double Quantum Dot dipole-coupled to a Single Photonic Mode," *Phys. Rev. B*, vol. 88, p. 125312, Sep 2013.

[4] Eichler, C. and Salathe, Y. and Mlynek, J. and Schmidt, S. and Wallraff, A., "Quantum-Limited Amplification and Entanglement in Coupled Nonlinear Resonators," *Phys. Rev. Lett.*, vol. 113, p. 110502, Sep 2014.

[5] Cohen-Tannoudji, C. and Dupont-Roc, J. and Grynberg, G., *Photons and Atoms: Introduction to Quantum Electrodynamics*. A Wiley-Inerscience publication, Wiley, 1997.

[6] A. Blais, J. Gambetta, A. Wallraff, D. I. Schuster, S. M. Girvin, M. H. Devoret, and R. J. Schoelkopf, "Quantum-Information Processing with Circuit Quantum Electrodynamics," *Physical Review A*, vol. 75, Mar 2007.

[7] Wallraff, A. and Schuster, D. I. and Blais, A. and Frunzio, L. and Majer, J. and Devoret, M. H. and Girvin, S. M. and Schoelkopf, R. J., "Approaching Unit Visibility for Control of a Superconducting Qubit with Dispersive Readout," *Phys. Rev. Lett.*, vol. 95, p. 060501, Aug 2005.

[8] A. Blais, R.-S. Huang, A. Wallraff, S. M. Girvin, and R. J. Schoelkopf, "Cavity Quantum Electrodynamics for Superconducting Electrical Circuits: An Architecture for Quantum Computation," *Phys. Rev. A*, vol. 69, p. 062320, Jun 2004.

[9] T. Ihn, *Semiconductor Nanostructures*. Oxford University Press, 2010.

[10] Anna Stockklauser, "Few Electron Double Quantum Dots for a Circuit QED Architecture," Master's thesis, ETH Zürich, 2012.

[11] L. Childress, A. Sorensen, and M. Lukin, "Mesoscopic Cavity Quantum Electrodynamics with Quantum Dots," *Physical Review A*, vol. 69, Apr 2004.

[12] M. Panish, "Molecular-Beam Epitaxy," *Science*, vol. 208, no. 4446, pp. 916–922, 1980.

[13] Pobell, F., *Matter and Methods at Low Temperatures*. Springer, 2007.

[14] Deniz Bozyigit, "Correlation Function Measurements of a Microwave Single Photon Source," Master's thesis, ETH Zürich, 2010.

[15] Mallet, F. and Castellanos-Beltran, M. A. and Ku, H. S. and Glancy, S. and Knill, E. and Irwin, K. D. and Hilton, G. C. and Vale, L. R. and Lehnert, K. W., "Quantum State Tomography of an Itinerant Squeezed Microwave Field," *Phys. Rev. Lett.*, vol. 106, p. 220502, Jun 2011.

[16] Kinion, D. and Clarke, John, "Microstrip Superconducting Quantum Interference Device Radio-Frequency Amplifier: Scattering Parameters and Input Coupling," *Applied Physics Letters*, vol. 92, no. 17, 2008.

[17] Vijay, R. and Slichter, D. H. and Siddiqi, I., "Observation of Quantum Jumps in a Superconducting Artificial Atom," *Phys. Rev. Lett.*, vol. 106, p. 110502, Mar 2011.

[18] Eichler, C. and Bozyigit, D. and Wallraff, A., "Characterizing Quantum Microwave Radiation and its Entanglement with Superconducting Qubits using Linear Detectors," *Phys. Rev. A*, vol. 86, p. 032106, Sep 2012.

[19] Eichler, C. and Bozyigit, D. and Lang, C. and Steffen, L. and Fink, J. and Wallraff, A., "Experimental State Tomography of Itinerant Single Microwave Photons," *Phys. Rev. Lett.*, vol. 106, p. 220503, Jun 2011.

[20] Eichler, C. and Bozyigit, D. and Lang, C. and Baur, M. and Steffen, L. and Fink, J. M. and Filipp, S. and Wallraff, A., "Observation of Two-Mode Squeezing in the Microwave Frequency Domain," *Phys. Rev. Lett.*, vol. 107, p. 113601, Sep 2011.

[21] Lang, C. and Bozyigit, D. and Eichler, C. and Steffen, L. and Fink, J. M. and Abdumalikov, A. A. and Baur, M. and Filipp, S. and da Silva, M. P. and Blais, A. and Wallraff, A., "Observation of Resonant Photon Blockade at Microwave Frequencies Using Correlation Function Measurements," *Phys. Rev. Lett.*, vol. 106, p. 243601, Jun 2011.

[22] C. Wen, "Coplanar Waveguide: A Surface Strip Transmission Line Suitable for Nonreciprocal Gyromagnetic Device Applications," *Microwave Theory and Techniques, IEEE Transactions on*, vol. 17, pp. 1087–1090, Dec 1969.

[23] R. N. Simons, *Coplanar Waveguide Circuits, Components, and Systems*. Wiley Series in Microwave and Optical Engineering, Newark, NJ: Wiley, 2001.

[24] D. M. Pozar, *Microwave engineering; 3rd ed.* Hoboken, NJ: Wiley, 2005.

[25] I. Wolff, *Coplanar Microwave Integrated Circuits*. Wolff, 2005.

[26] Lars Steffen, *Quantum Teleportation and Efficient Process Verification with Superconducting Circuits*. PhD thesis, ETH Zürich, 2013.

[27] Gevorgian, S. and Linner, L.J.P. and Kollberg, E.L., "CAD models for Shielded Multilayered CPW," *Microwave Theory and Techniques, IEEE Transactions on*, vol. 43, pp. 772–779, Apr 1995.

[28] Ponchak, G.E. and Papapolymerou, J. and Tentzeris, M.M., "Excitation of Coupled Slotline Mode in finite-ground CPW with unequal Ground-Plane Widths," *Microwave Theory and Techniques, IEEE Transactions on*, vol. 53, pp. 713–717, Feb 2005.

[29] Houck, A. A. and Schreier, J. A. and Johnson, B. R. and Chow, J. M. and Koch, Jens and Gambetta, J. M. and Schuster, D. I. and Frunzio, L. and Devoret, M. H. and Girvin, S. M. and Schoelkopf, R. J., "Controlling the Spontaneous Emission of a Superconducting Transmon Qubit," *Phys. Rev. Lett.*, vol. 101, p. 080502, Aug 2008.

[30] Chen, Zijun and Megrant, A. and Kelly, J. and Barends, R. and Bochmann, J. and Chen, Yu and Chiaro, B. and Dunsworth, A. and Jeffrey, E. and Mutus, J. Y. and ÓMalley, P. J. J. and Neill, C. and Roushan, P. and Sank, D. and Vainsencher, A. and Wenner, J. and White, T. C. and Cleland, A. N. and Martinis, John M., "Fabrication and Characterization of Aluminum Airbridges for Superconducting Microwave Circuits," *Applied Physics Letters*, vol. 104, no. 5, 2014.

[31] Adrian Stalder, "Influence of Wire Bonds on Coplanar Waveguide Resonators," Master's thesis, ETH Zürich, 2010.

[32] Richards, P.I, "Resistor-Transmission-Line Circuits," *Proceedings of the IRE*, vol. 36, pp. 217–220, Feb 1948.

[33] Lang, C. and Bozygit, D. and Salathe, Y. and Eichler, C. and Wallraff, A., "Quantum Signal Analyzer for Itinerant Microwave Radiation." Work in progress, Mar 2013.

[34] Mandel, L. and Wolf, E., *Optical Coherence and Quantum Optics*. Cambridge University Press, 1995.

[35] Peebles, P., *Probability, Random Variables, and Random Signal Principles*. McGraw-Hill Series in Electrical and Computer Engineering Series, McGraw-Hill Companies,Incorporated, 2001.

[36] Yves Salathe, "Towards Gigahertz Bandwidth Digital Signal Processing in Circuit Quantum Electrodynamics," Master's thesis, ETH Zürich, 2011.

[37] Christian Kern, "Measurement of Correlation Functions with a High Bandwidth FPGA," Master's thesis, ETH Zürich, 2013.

[38] Y.-C. Tsao and K. Choi, "Area-Efficient Parallel FIR Digital Filter Structures for Symmetric Convolutions Based on Fast FIR Algorithm," *IEEE Trans. Very Large Scale Integr. Syst.*, vol. 20, pp. 366–371, Feb 2012.

[39] Parker, D.A and Parhi, K.K., "Area-efficient parallel FIR digital filter implementations," in *Application Specific Systems, Architectures and Processors, 1996. ASAP 96. Proceedings of International Conference on*, pp. 93–111, Aug 1996.

[40] W. van der Wiel, S. De Franceschi, J. Elzerman, T. Fujisawa, S. Tarucha, and L. Kouwenhoven, "Electron Transport through Double Quantum Dots," *Reviews OF Modern Physics*, vol. 75, pp. 1–22, Jan 2003.

[41] Reimann, Stephanie M. and Manninen, Matti, "Electronic structure of quantum dots," *Rev. Mod. Phys.*, vol. 74, pp. 1283–1342, Nov 2002.

[42] Y. Nazarov and Y. Blanter, *Quantum Transport: Introduction to Nanoscience*. Cambridge University Press, 2009.

[43] Tobias Frey, *Interaction between Quantum Dots and Superconducting Microwave Resonators*. PhD thesis, ETH Zürich, 2013.

[44] David-Dominik Jarausch, "Quantum Dots in a Hybrid Superconducting-Semiconducting Architecture," Master's thesis, ETH Zürich, 2013.

[45] D. Taubert, D. Schuh, W. Wegscheider, and S. Ludwig, "Determination of Energy Scales in Few-Electron Double Quantum Dots," *Review of Scientific Instruments*, vol. 82, no. 12, 2011.

[46] K. D. Petersson, L. W. McFaul, M. D. Schroer, M. Jung, J. M. Taylor, A. A. Houck, and J. R. Petta, "Circuit Quantum Electrodynamics with a Spin Qubit," *Nature*, vol. 490, pp. 380–383, Oct 18 2012.

[47] K. D. Petersson, C. G. Smith, D. Anderson, P. Atkinson, G. A. C. Jones, and D. A. Ritchie, "Charge and Spin State Readout of a Double Quantum Dot Coupled to a Resonator," *Nano Letters*, vol. 10, no. 8, pp. 2789–2793, 2010. PMID: 20698590.

[48] T. Frey, P. J. Leek, M. Beck, J. Faist, A. Wallraff, K. Ensslin, T. Ihn, and M. Büttiker, "Quantum dot admittance probed at microwave frequencies with an on-chip resonator," *Phys. Rev. B*, vol. 86, p. 115303, Sep 2012.

[49] A. Wallraff, A. Stockklauser, T. Ihn, J. R. Petta, and A. Blais, "Comment on Vacuum Rabi Splitting in a Semiconductor Circuit QED System," *Phys. Rev. Lett.*, vol. 111, p. 249701, Dec 2013.

[50] C. W. Gardiner and M. J. Collett, "Input and Output in Damped Quantum Systems: Quantum Stochastic Differential Equations and the Master Equation," *Phys. Rev. A*, vol. 31, pp. 3761–3774, Jun 1985.

[51] D. F. Walls and Milburn, G.J., *Quantum Optics*. Springer Study Edition, Springer-Verlag, 1995.

[52] J. R. Petta, A. C. Johnson, C. M. Marcus, M. P. Hanson, and A. C. Gossard, "Manipulation of a Single Charge in a Double Quantum Dot," *Phys. Rev. Lett.*, vol. 93, p. 186802, Oct 2004.

[53] D. I. Schuster, A. Wallraff, A. Blais, L. Frunzio, R.-S. Huang, J. Majer, S. M. Girvin, and R. J. Schoelkopf, "ac Stark Shift and Dephasing of a Superconducting Qubit Strongly Coupled to a Cavity Field," *Phys. Rev. Lett.*, vol. 94, p. 123602, Mar 2005.

[54] T. Fujisawa, T. H. Oosterkamp, W. G. van der Wiel, B. W. Broer, R. Aguado, S. Tarucha, and L. P. Kouwenhoven, "Spontaneous Emission Spectrum in Double Quantum Dot Devices," *Science*, vol. 282, no. 5390, pp. 932–935, 1998.

[55] M. P. da Silva, D. Bozyigit, A. Wallraff, and A. Blais, "Schemes for the observation of photon correlation functions in circuit QED with linear detectors," *Phys. Rev. A*, vol. 82, p. 043804, Oct 2010.

[56] Lang, C., "Model for Measuring Correlation Functions." Unpublished, Sep 2011.

[57] C. M. Caves, "Quantum Limits on Noise in Linear Amplifiers," *Phys. Rev. D*, vol. 26, pp. 1817–1839, Oct 1982.

[58] D. Bozyigit, C. Lang, L. Steffen, J. M. Fink, C. Eichler, M. Baur, R. Bianchetti, P. J. Leek, S. Filipp, M. P. da Silva, A. Blais, and A. Wallraff, "Antibunching of Microwave-Frequency Photons Observed in Correlation Measurements using Linear Detectors," *Nature Physics*, vol. 7, pp. 154–158, Feb 2011.

[59] Y.-Y. Liu, K. D. Petersson, J. Stehlik, J. M. Taylor, and J. R. Petta, "Photon Emission from a Cavity-Coupled Double Quantum Dot," *Phys. Rev. Lett.*, vol. 113, p. 036801, Jul 2014.

[60] Christopher Eichler, *Experimental Characterization of Quantum Microwave Radiation and its Entanglement with a Superconducting Qubit*. PhD thesis, ETH Zürich, 2013.

[61] R. H. Brown and R. Q. Twiss, "Interferometry of the Intensity Fluctuations in Light. I. Basic Theory: The Correlation between Photons in Coherent Beams of Radiation," *Proceedings of the Royal Society of London. Series A. Mathematical and Physical Sciences*, vol. 242, no. 1230, pp. 300–324, 1957.

List of Figures

List of Tables

APPENDIX A

Design of a 8-parallel fast FIR filter

For compatibility with the existent FIR filters used for the Virtex-4 platform we decided to work with filters of length $N = 40$. Our general filter is thus given by

$$H = \sum_{n=0}^{39} h_n z^{-n} \tag{A.1}$$

By cascading a 2-parallel FFA 3 times, we have designed an 8-parallel FIR filter which requires a number $M = 9N/4$ of multipliers. We begin with a parallel FIR filter of block length $L = 8$ and express the filtering operation in the form of equation 5.11.

$$Y = \sum_{i=0}^{7} Y_i^L z^{-i} = \left(\sum_{j=0}^{7} X_j^L z^{-j} \right) \left(\sum_{k=0}^{7} H_k^L z^{-k} \right) \tag{A.2}$$

Where each H_k is obtained by decomposing equation A.1 it into $L = 8$ phases. Each phase is thus given by

$$H_k = \sum_{n=0}^{4} h_{8n+k} z^{-n} \; ; k \in \{0, \ldots, 7\} \tag{A.3}$$

Applying the 2by2 FFA algorithm (equation 5.14) to the filtering operation in equation A.2 yields

$$\begin{aligned} Y &= Y_0^{'} + z^{-1} Y_1^{'} = \left(X_0^{'} + z^{-1} X_1^{'} \right) \left(H_0^{'} + z^{-1} H_1^{'} \right) \\ &= X_0^{'} H_0^{'} + z^{-1} \left(\left(X_0^{'} + X_1^{'} \right) \left(H_0^{'} + H_1^{'} \right) - X_0^{'} H_0^{'} - X_1^{'} H_1^{'} \right) + z^{-2} X_1^{'} H_1^{'} \\ Y_0^{'} &= X_0^{'} H_0^{'} + z^{-2} X_1^{'} H_1^{'} \\ Y_1^{'} &= \left(\left(X_0^{'} + X_1^{'} \right) \left(H_0^{'} + H_1^{'} \right) - X_0^{'} H_0^{'} - X_1^{'} H_1^{'} \right) \end{aligned} \tag{A.4}$$

This has the same structure as figure 5.4. However, the application of the FFA algorithm has decomposed a 8-parallel filter into three 4-parallel filters, namely $H_0^{'}$, $H_1^{'}$, and $H_0^{'} + H_1^{'}$. We have

basically grouped the even(odd) terms of X and H according to

$$\begin{aligned}[\cdot]_0^{'} &= \sum_{i=0}^{L/2-1} z^{2i}\,[\cdot]_{2i} \\ [\cdot]_1^{'} &= \sum_{i=0}^{L/2-1} z^{2i}\,[\cdot]_{2i+1}\end{aligned} \tag{A.5}$$

Observing that each term in equation A.4 (i.e. $X_0^{'}H_0^{'}$, $X_1^{'}H_1^{'}$, and $\left(X_0^{'}+X_1^{'}\right)\left(H_0^{'}+H_1^{'}\right)$) is a filtering operation, we can apply the 2by2 FFA algorithm to each of them. In this way, each of these 4-parallel filter gets decomposed into three 2-parallel filters. Starting with $X_0^{'}H_0^{'}$ we obtain

$$\begin{aligned}X_0^{'}H_0^{'} = Y_0^0 + z^{-2}Y_1^0 &= \left(X_0^0 + z^{-2}X_1^0\right)\left(H_0^0 + z^{-2}H_1^0\right) \\ &= X_0^0H_0^0 + z^{-2}\left(\left(X_0^0+X_1^0\right)\left(H_0^0+H_1^0\right) - X_0^0H_0^0 - X_1^0H_1^0\right) + z^{-4}X_1^0H_1^0 \\ Y_0^0 &= X_0^0H_0^0 + z^{-4}X_1^0H_1^0 \\ Y_1^0 &= \left(\left(X_0^0+X_1^0\right)\left(H_0^0+H_1^0\right) - X_0^0H_0^0 - X_1^0H_1^0\right)\end{aligned} \tag{A.6}$$

Where we have again grouped the even(odd) terms of $[\cdot]_0^{'}$ into $[\cdot]_0^0$ and $[\cdot]_1^0$ respectively. Each term in equation A.6 is a 2-parallel filtering operation. The superscript 0 is simply an identifier to differentiate these terms from further applications of the FFA algorithm. We then apply the FFA a third time to synthesize each 2-parallel filter from equation A.6.

$$\begin{aligned}1)\ X_0^0H_0^0 &= \left(X_0 + z^{-4}X_4\right)\left(H_0 + z^{-4}H_4\right) \\ &= X_0H_0 + z^{-4}\left(\left(X_0+X_4\right)\left(H_0+H_4\right) - X_0H_0 - X_4H_4\right) + z^{-8}X_4H_4 \\ 2)\ X_1^0H_1^0 &= \left(X_2 + z^{-4}X_6\right)\left(H_2 + z^{-4}H_6\right) \\ &= X_2H_2 + z^{-4}\left(\left(X_2+X_6\right)\left(H_2+H_6\right) - X_2H_2 - X_6H_6\right) + z^{-8}X_6H_6 \\ 3)\ \left(X_0^0+X_1^0\right)\left(H_0^0+H_1^0\right) &= \left(\left(X_0+X_2\right) + z^{-4}\left(X_4+X_6\right)\right)\left(\left(H_0+H_2\right) + z^{-4}\left(H_4+H_6\right)\right) \\ &= \underbrace{\left(X_0+X_2\right)\left(H_0+H_2\right)}_{a} \\ &\quad + z^{-4}\left(\left(\sum_{i=0}^{3}X_{2i}\right)\left(\sum_{i=0}^{3}H_{2i}\right) - a - b\right) \\ &\quad + z^{-8}\underbrace{\left(X_4+X_6\right)\left(H_4+H_6\right)}_{b}\end{aligned} \tag{A.7}$$

Going back to equation A.4, we now apply the same process to $X_1^{'}H_1^{'}$

$$\begin{aligned} X_1^{'}H_1^{'} = Y_0^1 + z^{-2}Y_1^1 &= \left(X_0^1 + z^{-2}X_1^1\right)\left(H_0^1 + z^{-2}H_1^1\right) \\ &= X_0^1H_0^1 + z^{-2}\left(\left(X_0^1 + X_1^1\right)\left(H_0^1 + H_1^1\right) - X_0^1H_0^1 - X_1^1H_1^1\right) + z^{-4}X_1^1H_1^1 \\ Y_0^1 &= X_0^1H_0^1 + z^{-4}X_1^1H_1^1 \\ Y_1^1 &= \left(\left(X_0^1 + X_1^1\right)\left(H_0^1 + H_1^1\right) - X_0^1H_0^1 - X_1^1H_1^1\right) \end{aligned} \tag{A.8}$$

And by applying the 2by2 FFA algorithm to each of the terms in equation A.8 we obtain another set of three 2-parallel fast FIR filters.

$$\begin{aligned} 1)\ X_0^1H_0^1 &= \left(X_1 + z^{-4}X_5\right)\left(H_1 + z^{-4}H_5\right) \\ &= X_1H_1 + z^{-4}\left(\left(X_1 + X_5\right)\left(H_1 + H_5\right) - X_1H_1 - X_5H_5\right) + z^{-8}X_5H_5 \\ 2)\ X_1^1H_1^1 &= \left(X_3 + z^{-4}X_7\right)\left(H_3 + z^{-4}H_7\right) \\ &= X_3H_3 + z^{-4}\left(\left(X_3 + X_7\right)\left(H_3 + H_7\right) - X_3H_3 - X_7H_7\right) + z^{-8}X_7H_7 \\ 3)\ \left(X_0^1 + X_1^1\right)\left(H_0^1 + H_1^1\right) &= \left(\left(X_1 + X_3\right) + z^{-4}\left(X_5 + X_7\right)\right)\left(\left(H_1 + H_3\right) + z^{-4}\left(H_5 + H_7\right)\right) \\ &= \underbrace{\left(X_1 + X_3\right)\left(H_1 + H_3\right)}_{a} \\ &\quad + z^{-4}\left(\left(\sum_{i=0}^{3} X_{2i+1}\right)\left(\sum_{i=0}^{3} H_{2i+1}\right) - a - b\right) \\ &\quad + z^{-8}\underbrace{\left(X_5 + X_7\right)\left(H_5 + H_7\right)}_{b} \end{aligned} \tag{A.9}$$

Finally we apply the same process to $\left(X_0^{'} + X_1^{'}\right)\left(H_0^{'} + H_1^{'}\right)$

$$\begin{aligned} \left(X_0^{'} + X_1^{'}\right)\left(H_0^{'} + H_1^{'}\right) &= Y_0^2 + z^{-2}Y_1^2 \\ &= \left(\left(\left(X_0 + X_1\right) + z^{-4}\left(X_4 + X_5\right)\right) + z^{-2}\left(\left(X_2 + X_3\right) + z^{-4}\left(X_6 + X_7\right)\right)\right) \\ &\quad + \left(\left(\left(H_0 + H_1\right) + z^{-4}\left(H_4 + H_5\right)\right) + z^{-2}\left(\left(H_2 + H_3\right) + z^{-4}\left(H_6 + H_7\right)\right)\right) \\ &= \left(X_0^2 + z^{-2}X_1^2\right)\left(H_0^2 + z^{-2}H_1^2\right) \\ &= X_0^2H_0^2 + z^{-2}\left(\left(X_0^2 + X_1^2\right)\left(H_0^2 + H_1^2\right) - X_0^2H_0^2 - X_1^2H_1^2\right) + z^{-4}X_1^2H_1^2 \\ Y_0^2 &= X_0^2H_0^2 + z^{-4}X_1^2H_1^2 \\ Y_1^2 &= \left(\left(X_0^2 + X_1^2\right)\left(H_0^2 + H_1^2\right) - X_0^2H_0^2 - X_1^2H_1^2\right) \end{aligned} \tag{A.10}$$

And again synthesize three 2-parallel fast FIR filters

$$
\begin{aligned}
1)\ X_0^2 H_0^2 &= \Big((X_0+X_1)+z^{-4}(X_4+X_5)\Big)\Big((H_0+H_1)+z^{-4}(H_4+H_5)\Big) \\
&= \underbrace{(X_0+X_1)(H_0+H_1)}_{a} \\
&\quad + z^{-4}\left((X_0+X_1+X_4+X_5)(H_0+H_1+H_4+H_5)-a-b\right) \\
&\quad + z^{-8}\underbrace{(X_4+X_5)(H_4+H_5)}_{b} \\
2)\ X_1^2 H_1^2 &= \Big((X_2+X_3)+z^{-4}(X_6+X_7)\Big)\Big((H_2+H_3)+z^{-4}(H_6+H_7)\Big) \\
&= \underbrace{(X_2+X_3)(H_2+H_3)}_{a} \\
&\quad + z^{-4}\left((X_2+X_3+X_6+X_7)(H_2+H_3+H_6+H_7)-a-b\right) \\
&\quad + z^{-8}\underbrace{(X_6+X_7)(H_6+H_7)}_{b} \\
3)\ \left(X_0^2+X_1^2\right)\left(H_0^2+H_1^2\right) &= \left(\left(\sum_{i=0}^{3} X_i\right)+z^{-4}\left(\sum_{i=4}^{7} X_i\right)\right)\left(\left(\sum_{i=0}^{3} H_i\right)+z^{-4}\left(\sum_{i=4}^{7} H_i\right)\right) \\
&= \underbrace{\left(\sum_{i=0}^{3} X_i\right)\left(\sum_{i=0}^{3} H_i\right)}_{a} \\
&\quad + z^{-4}\left(\left(\sum_{i=0}^{7} X_i\right)\left(\sum_{i=0}^{7} H_i\right)-a-b\right) \\
&\quad + z^{-8}\underbrace{\left(\sum_{i=4}^{7} X_i\right)\left(\sum_{i=4}^{7} H_i\right)}_{b}
\end{aligned}
\tag{A.11}
$$

In this way we have synthesized an 8-parallel FIR filter by cascading three 2by2 FFAs. Since each application of a 2by2 FFA gives us 3 filtering operations, we end up with 27 individual filtering operations of length $N/L = 5$.